
Summation of Path Integrals for Resonant Transport through an Interacting Quantum-Dot Spin Valve

DISSERTATION

zur Erlangung des Grades
„Doktor der Naturwissenschaften“

an der Fakultät für Physik
der Universität Duisburg-Essen

vorgelegt von

SIMON MUNDINAR, M. SC.
aus Neuendettelsau

DuEPublico

Duisburg-Essen Publications online

UNIVERSITÄT
DUISBURG
ESSEN

Offen im Denken

ub | universitäts
bibliothek

Diese Dissertation wird über DuEPublico, dem Dokumenten- und Publikationsserver der Universität Duisburg-Essen, zur Verfügung gestellt und liegt auch als Print-Version vor.

DOI: 10.17185/duepublico/73437

URN: urn:nbn:de:hbz:464-20201123-100556-4

Alle Rechte vorbehalten.

Referent: Prof. Dr. J. König
Korreferent: Prof. Dr. M. Thorwart

Tag der mündlichen Prüfung: 22.10.2020

The following articles originated in connection with the work on this thesis:

1. S. Mundinar, P. Stegmann, J. König, and S. Weiss,
Iterative path-integral summations for the tunneling magnetoresistance in interacting quantum-dot spin valves,
[Phys. Rev. B **99**, 195457 \(2019\)](#).
2. S. Mundinar, A. Hucht, J. König, and S. Weiss,
Interaction induced current asymmetries in resonant transport through interacting quantum-dot spin valves revealed by iterative summation of path integrals,
[Phys. Rev. B **102**, 045404 \(2020\)](#).

Zusammenfassung

Das Feld der Spintronik, bei dem der Elektronenspin neben der Elektronenladung als zusätzlicher Freiheitsgrad zur Informationsübertragung genutzt wird, ist äußerst vielversprechend in Bezug auf künftige Entwicklungen im Bereich der Informationsverarbeitung und -speicherung. Besonders wichtig ist dabei das Spinventil, im Grunde ein ‚Spintransistor‘, der die externe Kontrolle des Spintransports ermöglicht. Eine kontinuierliche Miniaturisierung von Spinventilen begründet das Konzept des *Quantenpunktspinventils*, das das Analogon zum Einzelelektronentransistor darstellt. Es fügt sich aus einem Quantenpunkt zusammen der an ferromagnetische Zuleitungen gekoppelt ist und erlaubt individuelle Kontrolle über einzelne Spins, indem man den magnetischen Tunnelwiderstand justiert, der das Spinventil definiert. Ziel dieser Arbeit ist es ein umfassendes theoretisches Bild von spinabhängigem elektronischem Transport durch ein wechselwirkendes Quantenpunktspinventil zu erstellen.

Transport durch Quantenpunktsysteme wird oft als klar voneinander getrennte Tunnelereignisse dargestellt, bei denen je ein Elektron von der Zuleitung auf den Quantenpunkt und dann weiter zur Ableitung tunnelt. Es hat sich jedoch gezeigt, dass diese sequentielle Beschreibung von elektronischem Transport unzureichend ist, insbesondere im Bereich niedriger Temperaturen und starker Ankopplung an die Zuleitungen. In Wirklichkeit tragen unendlich viele unterschiedliche Prozesse dazu bei, Elektronen von der Zuleitung über den Quantenpunkt zur Ableitung zu bewegen. Um ein vollständiges Bild von elektrischem Transport und der Spindynamik des Quantenpunktspinventils zu erhalten, ist es grundlegend wichtig, diese *resonanten Tunneleffekte* zu berücksichtigen. Dies ist das Hauptziel dieser Arbeit. Dabei legen wir besonderes Augenmerk auf das allgemeine Regime, in dem alle relevanten Energieskalen von der gleichen Größenordnung sind und dementsprechend störungstheoretische Ansätze fehlschlagen. Um dieses Regime inklusive resonantem Tunneln zu charakterisieren, machen wir von der numerisch exakten Technik namens *iterative Summation von Pfadintegralen* (ISPI) Gebrauch und erweitern sie, sodass spinabhängiger Transport mitberücksichtigt wird. Um den Einfluss der Spindynamik auf den elektrischen Transport zu untersuchen, führen wir zusätzliche, quantenpunkt-basierte Observablen, wie die Besetzungszahl und die Spinprojektion, für die Technik ein. Zusätzlich entwickeln wir die Methode weiter, indem wir sie auf einen *Transfermatrix-Ansatz* abbilden. Das Ergebnis ist eine neue Implementation der ISPI Methode, die sie vielseitiger und schneller macht.

Ausgestattet mit den beiden ISPI-Implementationen demonstrieren wir, dass es wesentlich ist, resonante Effekte zu berücksichtigen, um eine realistische theoretische Beschreibung des magnetischen Tunnelwiderstands eines Quantenpunktspinventils zu erhalten. Bei der Untersuchung des nicht-kollinearen Aufbaus des Quantenpunktspinventils zeigen wir, wie die Teilchen-Loch-Symmetrie des Systems von dem Zusammenspiel von Coulomb-Wechselwirkung und einem lokalen magnetischen Feld gebrochen wird. Das führt zu Asymmetrien im Leitwert und in den Spinkomponenten als Funktion der Gatterspannung.

Summary

The field of spintronics, where the electron spin is used next to the electron charge as an additional degree of freedom for information transfer, shows huge promise for future developments in the area of information processing and storage. Of particular importance to this field is the spin valve, a device that allows control of spin transport via external means, basically a ‘spin transistor’. Continued miniaturization of the spin valve motivates the proposition of a *quantum-dot spin valve*, the analog to a single-electron transistor. Such a device can be constructed from a quantum dot coupled to ferromagnetic leads and allows for individual control over single spins by tuning the tunnel magnetoresistance effect that defines the spin valve. In this work, we aim to give a thorough theoretical picture of spin-dependent electronic transport through an interacting quantum-dot spin valve.

Transport through quantum-dot systems is often pictured as well-separated tunneling events, where a single electron tunnels from the source electrode to the quantum dot and then on to the drain electrode. This sequential description of electronic transport, however, has proven to be lacking in the low-temperature regime and at strong coupling to the leads. In reality, infinitely many different processes contribute to the procedure of moving electrons from the source through the quantum dot and to the drain. To receive a complete picture of the electronic transport and the spin dynamics of the quantum-dot spin valve, it is crucial to include all of these *resonant tunneling effects*, which is the main goal of this work. We especially focus on the generic regime, where all relevant energy scales within the system are of equal order of magnitude, and thus perturbative approaches severely fail. To achieve a characterization of this regime including resonant tunneling, we employ the numerically exact technique of *iterative summation of path integrals* (ISPI) and generalize it to account for spin-dependent transport. To be able to study the impact of spin dynamics on the electronic transport we expand the pool of observables within this technique to include quantum-dot based quantities like the occupation number and spin projection. In addition, we advance the method itself by mapping it to a *transfer-matrix approach*. This leads to a novel implementation of the ISPI technique, which increases its performance and versatility.

With the two implementations of the technique at our disposal, we demonstrate that resonant effects are crucial to reach a reasonable theoretical description of the tunnel magnetoresistance of the interacting quantum-dot spin valve. When investigating noncollinear setups of the quantum-dot spin valve we show how particle-hole symmetry of the system is broken via the interplay between Coulomb interactions and a local magnetic field, leading to asymmetries in the conductance and in components of the spin projection as a function of the gate voltage.

Contents

1	Introduction	1
1.1	Quantum-Dot Systems	3
1.1.1	Coulomb Blockade and Kondo Effect	4
1.1.2	Tunnel Magnetoresistance and Exchange Field	6
1.1.3	Superconducting Leads and Double Quantum Dots	9
1.2	Experimental Realizations of Quantum-Dot Spin Valves	10
1.3	Structure of this Thesis	13
2	Theoretical Concepts for Fermionic Systems in Nonequilibrium	15
2.1	Keldysh Contour	16
2.2	Nonequilibrium Green Functions	18
2.2.1	Properties of Nonequilibrium Green Functions	19
2.2.2	Keldysh Rotation	20
2.2.3	Langreth Theorem	21
2.3	Grassmann Numbers	22
2.3.1	Grassmann Algebra	22
2.3.2	Grassmann Gaussian Integrals	23
2.4	Fermionic Coherent States	25
2.5	Summary	27
3	Quantum-Dot Spin Valve	29
3.1	Model	31
3.2	Noninteracting Limit	34
3.2.1	Current	35
3.2.2	Occupation Number and Spin Components	38
3.3	Theoretical Approaches	39
3.4	Summary	41
4	Coherent-State Path Integrals	43
4.1	Noninteracting Limit	45
4.1.1	Building the Path Integral	45
4.1.2	Solving the Path Integral	49
4.1.3	Time-Discrete Dressed Green Function	50
4.2	Interactions	51
4.3	Observables and Source Terms	52
4.3.1	Current	54
4.3.2	Occupation Number and Spin Projection	55

4.4	Summary	56
5	Iterative Summation of Path Integrals	57
5.1	Finite-Time Implementation	59
5.2	Transfer-Matrix Implementation	60
5.2.1	Symmetrization	63
5.2.2	Analytic Derivatives	64
5.3	Convergence	67
5.4	Parallelization and Performance	69
5.5	Summary	73
6	Results	75
6.1	Benchmark	75
6.1.1	Noninteracting Limit	75
6.1.2	High-Temperature Regime	81
6.1.3	Finite-Time and Transfer-Matrix Implementation	83
6.2	Collinear Setup	84
6.2.1	Temperature Dependence	85
6.2.2	Transport Spectroscopy	87
6.2.3	Summary	90
6.3	Noncollinearity and Zeeman field	91
6.3.1	Interaction-Induced Current Asymmetry	92
6.3.2	Angular Dependence	96
6.3.3	Summary	98
7	Conclusions	99
A	Infinite Order Expansion	101
B	Master Equation Approach	105
C	Inverse Keldysh Rotation	109
D	Fourier Transformation of the Tunneling Self-Energies	111
	Bibliography	115
	Acknowledgement	125

1 Introduction

Microprocessors are an integral part of today's everyday life. They are small processing units, where all required parts are joined in one integrated circuit. Depending on the field of application microprocessors are adapted, e.g. to have minimal power intake or maximal calculation power, to be heat- or radiation-resistant. Due to this versatility they can be found everywhere, from washing machines, radios and TVs to computers and mobile phones, in airplanes and cars as well as satellites and spacecrafts, and so on. With topics like artificial intelligence, big data, machine learning and the internet of things on the rise, microprocessors become even more widespread.

Transistors are the basic building blocks of any microprocessor. Therefore, the digital revolution which led to today's prevalence of microprocessors was kick-started by the invention of the transistor by Shockley, Bardeen and Brattain in 1947, for which they were awarded with the Nobel Prize in 1956. Transistors are semiconductor circuit elements whose conductance is tunable. They are often used as switches but also find application as amplifiers. Usually, transistors are constructed from semiconducting material that is positively (p) and negatively (n) doped in such a way that two p-n-junctions connected in series emerge. Three contacts (source, drain and gate) are applied, with source and drain connecting to parts with equal doping, while the gate connects either directly or via an insulating layer to the part in between, that is oppositely doped. Depending on the type of transistor, the resistivity between source and drain can be tuned either via a small current between gate and source or via a voltage that is applied to the gate. In the latter design, which is called *field effect transistor* (FET), the gate voltage influences the charge distribution within the semiconducting material allowing for a conducting channel to emerge between source and drain. As a result, the width of this channel, and with it the conductance of the transistor, is tuned via the gate voltage.

FETs were combined into increasingly complicated and powerful integrated circuits, and thus led to the development of microprocessors. To make these microprocessors more powerful significant effort is put into the optimization and miniaturization of transistors. The main benefits of smaller transistors are – apart from allowing more transistors in the same area – faster switching times and an increased power efficiency. The latter can be understood by the fact that power is necessary to charge and discharge the transistor's gate capacitances. Following electrostatics, the power to charge a capacitor is $\sim CV^2f$, where C is the gate capacitance, V is the charging voltage and f is the frequency with which the capacitor is charged. For a smaller transistor the capacitance C is smaller and the voltage needed to charge the transistor is smaller, too. As a result, it is often beneficial to have transis-

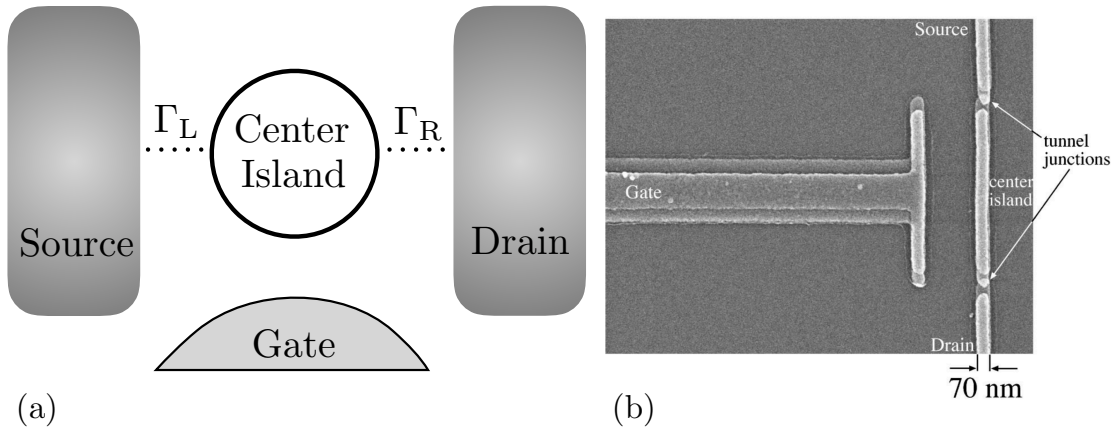


Figure 1.1: (a) Systematic sketch of a single-electron transistor with an island in the middle and tunneling strengths for the left and right lead $\Gamma_{L/R}$. The central island can be tuned via a gate voltage. (b) Scanning electron micrograph of an aluminum single-electron transistor. Taken from Ref. [2].

tors as small as possible. In recent years transistors with feature sizes of less than 10 nm have been commercially available. Thanks to this development, it is possible to have billions of transistors combined in a small microprocessor today, giving us enough calculation power even for demanding applications like machine learning and artificial intelligence.

When working with systems in the nanometer scale, we enter the regime of mesoscopic physics and even nanophysics, where quantum effects, like electron tunneling, cannot be neglected anymore. As a consequence, such structures are quantum many-body systems, for which the finite system size has to be taken into account. This interplay leads to interesting effects, like e.g. a conductance quantum of $2e^2/h$ per transport channel for quantum point contacts [1].

Once quantum effects play a significant role, it is necessary to adopt the design of electronic devices to these circumstances. This naturally lead to the concept of a *single-electron transistor*, which was pioneered by the work of Fulton and Dolan in 1987 [3]. These devices work similar to a FET, allowing control over the conductance via a gate voltage, but are based on the quantum mechanical tunneling effect. They are built from two tunnel junctions connected in series, with a small island between them that is contacted capacitively with the gate electrode. A systematic sketch of a single-electron transistor can be seen in Fig. 1.1 (a), while in panel (b) of that figure an experimental realization of an aluminum single-electron transistor can be seen. The island between the two tunnel junctions is usually chosen such that they only provide a finite number of different energy levels. Applying a voltage to the gate electrode allows us to control the island's energy levels and to tune electric

transport from source to drain. Possible realizations for the central island are e.g. small metallic islands or quantum dots, which are small structures that provide only one or at maximum very few energy levels. Single-electron transistors usually cannot be used in complex circuits due to fluctuations, but other applications have been found. Their high sensitivity means they are well-suited as charge sensors, microwave detectors or high precision electrometers [4].

Of course, electrons are fermionic particles with spin $\frac{1}{2}$. This degree of freedom is utilized in addition to the electron charge in the field of spintronics. The main benefit is an improved efficiency in information transfer and storage. As a consequence, spintronic devices are strong candidates for the use in the emerging in-memory processing technology, where the processor is directly integrated within its memory [5]. This technology is one of the basic building blocks in the field of neuromorphic computing. Just as in ordinary electronics one is able to construct transistor-like spintronic devices, so called *spin valves*, whose conductance differs depending on the spin of the particles. These devices are based on either the giant magnetoresistance (GMR), for whose discovery Fert and Grünberg were awarded with the Nobel Prize in 2007, or the *tunnel magnetoresistance* (TMR), which is endemic e.g. in systems that are the spintronic equivalent to the single-electron transistor, called *quantum-dot spin valves*. The quantum-dot spin valve is realized via a central quantum dot, that is tunnel-coupled to two ferromagnetic leads and contacted capacitively by a gate electrode. The TMR effect then causes the conductance through the system to vary depending on the leads' relative magnetization directions. If the magnetizations are aligned in parallel the conductance is large, while it is suppressed if they are aligned antiparallely.

The quantum-dot spin valve is the main focus of this thesis. The goal is to give a thorough theoretical description of this system. For this we make use of the technique of *iterative summation of path integrals* (ISPI) and generalize it to account for the spin-dependent transport that is necessary for an accurate physical picture of the quantum-dot spin valve. We develop the method further and demonstrate that it is closely related to the transfer-matrix approach, known from statistical physics.

1.1 Quantum-Dot Systems

Since the quantum-dot spin valve is a quantum-dot system, we stop short to give a basic introduction to such systems and to introduce some of the most prominent effects that are observed in them. Quantum dots are mesoscopic systems, small enough to have discrete energy levels for electrons to occupy, to which electrons are confined. The electrons occupying the quantum dot strongly interact via the Coulomb interaction, due to the smallness of the system. As a consequence, it is crucial to include these interactions to obtain an accurate description of transport through a quantum-dot system, even though the interplay between nonequilibrium electronic transport through the system and Coulomb interactions poses a great challenge from a theoretician's point of view.

The experimental discovery of quantum dots was in the early 1980s by Ekimov [6, 7] and Brus [8], who first described an increase of the distance between energy levels with decreasing size of quantum dots. This so-called quantum size effect has found commercial application recently in liquid crystal displays. There, a thin layer of quantum dots converts the blue backlight of the LEDs into other colors, leading to higher brilliance and lower power consumption than the usually used phosphor layer [9].

To allow for electric transport studies, the quantum dot is tunnel-coupled to external leads. The leads not only have their own transport properties but also specify the particles that partake in electric transport. Consequently, the physical properties of the leads have significantly impact on the transport characteristics of the setup. With a quantum dot coupled to two metallic leads or to two ferromagnetic leads we already mentioned two examples, the single-electron transistor and the quantum-dot spin valve, respectively. We discuss some prominent effects that occur in these two setups in the following and then give a short outlook to other quantum-dot systems.

1.1.1 Coulomb Blockade and Kondo Effect

We already mentioned the possibility to construct a single-electron transistor by coupling the quantum dot via tunnel barriers to two normal metal leads and contacting it capacitively to a gate electrode. Since the quantum dot provides only a few discrete energy levels, one finds very clear patterns in the transport spectroscopy for the different charge states. This can be seen in Fig. 1.2 (a), where the current is shown as function of the gate voltage. For highly negative gate voltages the quantum dot is unoccupied in this case. When increasing the gate voltage, one finds a sequence of peaks each followed by a valley. During these valleys the occupation number of the quantum dot is fixed to an integer number of electrons and transport through the device is suppressed. Whenever an additional electron is able to tunnel on the dot, one measures a peak in the current. The width of the valleys is proportional to the energy required to add an electron to the quantum dot. This addition energy comes about from two contributions: One is the Coulomb interaction, which is the reason why we talk about the *Coulomb blockade*, that causes the valleys to form. The other is the electron affinity of the current state of the quantum dot, which varies the size of the valleys, since some states are more stable than others [12]. This is the case e.g. when shells become fully occupied.

While Fig. 1.2 (a) was taken at one specific low bias voltage, we also have to take different bias voltages into account to get a complete transport spectroscopy of the system. In Fig. 1.2 (b) a measurement of such a transport spectroscopy is depicted for a silicon quantum dot. The differential conductance dI/dV is given as a function of both the bias voltage and the gate voltage. In this picture, the valleys caused by Coulomb blockade transform to prominent features, called *Coulomb diamonds* (the areas in dark blue), in which the total number of electrons on the quantum dot is again fixed and transport is suppressed. Once the bias voltage is large enough

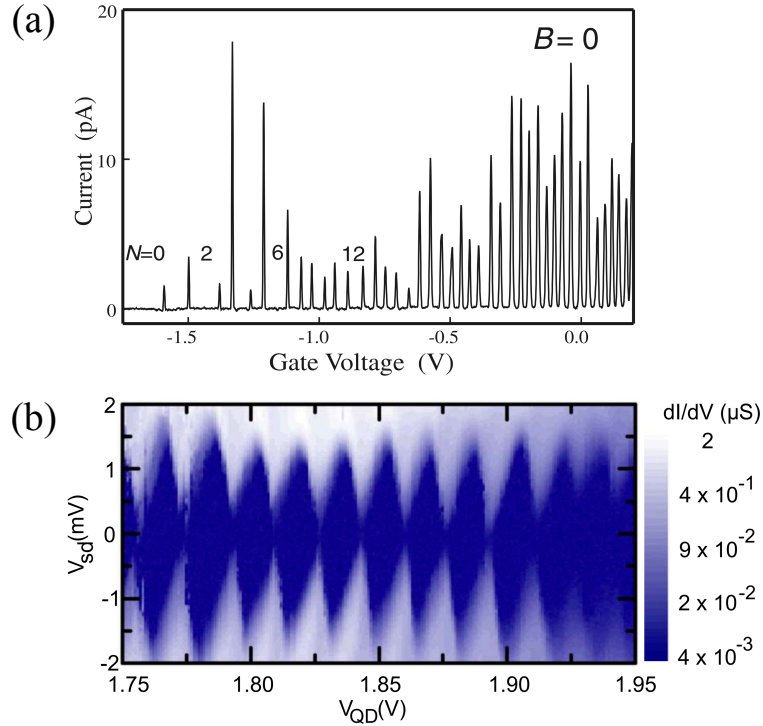


Figure 1.2: (a) Current through a quantum dot as a function of gate voltage, taken from Ref. [10]. Each peak shows the transition to a new charge state, where the occupation number is increased by one. In the areas between the peaks the occupation remains constant. (b) dI/dV as a function of gate and bias voltage for a silicon quantum dot, taken from Ref. [11]. The dark blue diamond shapes are the Coulomb diamonds throughout which the occupation number of the quantum dot is constant and transport is blocked.

to contain two or even more energy levels within the transport window, transport through the system is possible, which is the reason why Coulomb diamonds are only prevalent at low to intermediate bias voltages. As can be seen, the size of the Coulomb diamonds varies, meaning – just as before – that some charge states of the quantum dot are more stable than others. As a result it is possible to read off the Coulomb interaction from the average height of the Coulomb diamonds, and the level spacing from their difference in size [13].

There is an effect that requires these distinct Coulomb diamonds, caused by a strong Coulomb repulsion, to ensure a constant number of electrons on the dot. The so called *Kondo effect* describes a resonance where the conductance reaches its maximal value of the conductance quantum $G = 2e^2/h$. A transport spectroscopy including the Kondo effect is shown in Fig. 1.3 (a). The effect appears at sufficiently low temperatures $T < T_K$, with T_K being the so-called Kondo temperature, see Fig. 1.3 (b), and once the quantum dot is occupied by an odd number of electrons.

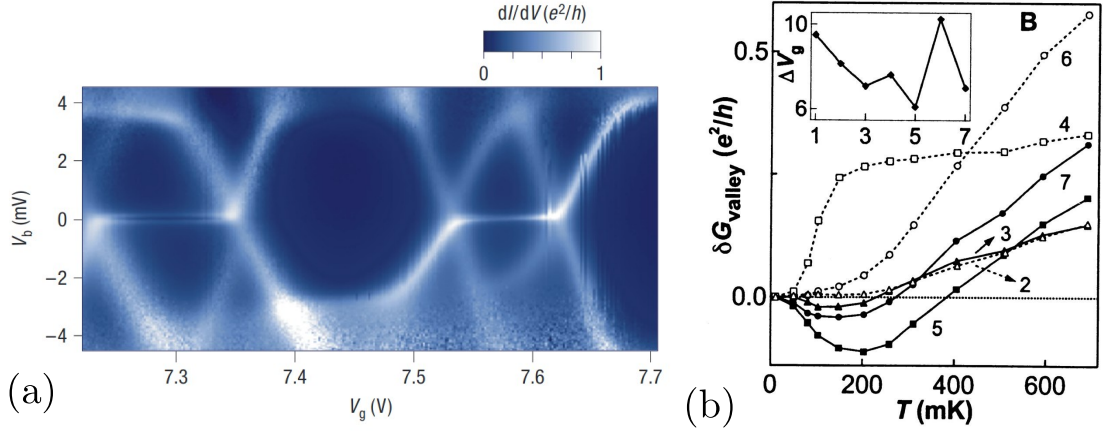


Figure 1.3: (a) Transport spectroscopy with Kondo peaks at zero bias in the Coulomb diamonds corresponding to a quantum dot with odd occupation number, taken from Ref. [14]. (b) The temperature dependence of the Kondo effect, taken from Ref. [15]. The effect itself is given in minima of the change in valley conductance $\delta G = G(T) - G(T_{\text{base}})$ with $T_{\text{base}} = 45\text{mK}$. Minima are only visible when the occupation number is odd.

This remarkable effect was first discovered in some metals by de Haas, de Boer and van de Berg [16] and theoretically explained by Kondo [17]. Later it was shown that quantum dots are Kondo systems, for which the Kondo effect can be tuned via the gate voltage [15, 18].

To explain the Kondo effect, we assume a quantum dot with only one energy level. If the bias voltage is much smaller than the Coulomb interaction $eV \ll U$, we are able to create a state where the dot is only singly occupied and first-order transport is blocked. The electron cannot leave the dot, since its energy is far below the transport window, and second electron cannot tunnel onto the dot, since the two-electron energy is far above the transport window. However, higher-order effects in the tunneling still allow transport through the quantum dot via virtual tunneling events. For the Kondo effect such effects are crucial since they allow for an effective spin flip of the electron occupying the dot. Many of these spin-flip processes in succession screen the spin of the electron by forming a spin-singlet state between the electrons in the leads and on the dot [15]. Consequently, to make the Kondo effect visible, low bias voltages are required in combination with strong Coulomb interactions and low temperatures, while the hybridization of the dot via the leads has to be high enough to allow for higher-order effects to occur.

1.1.2 Tunnel Magnetoresistance and Exchange Field

Coulomb blockade and the Kondo effect are general effects observable in quantum-dot systems, including the quantum-dot spin valve. We now turn to two well known

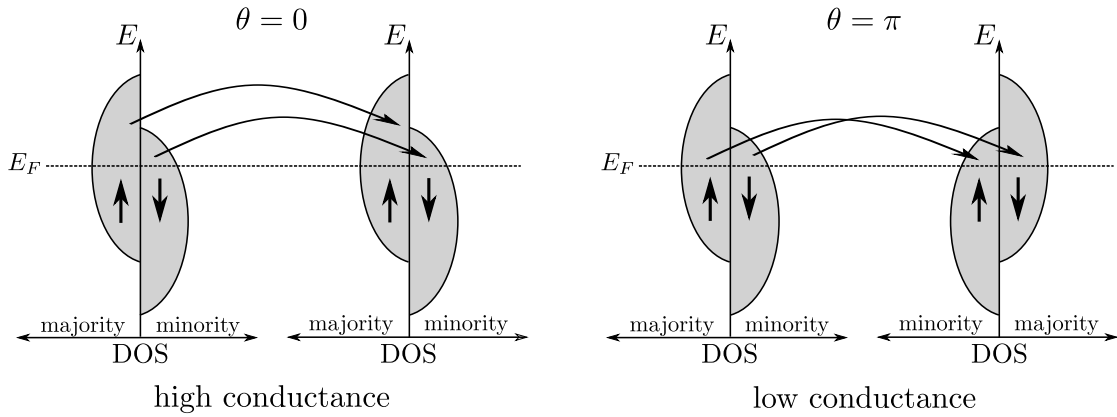


Figure 1.4: Sketches of the densities of states (DOS) as a function of the energy E of the two ferromagnetic leads. Majority and minority spins are defined with respect to the Fermi energy E_F . The left-hand side depicts the parallel setup in which the conductance through the system is high, while the right-hand side shows the antiparallel setup where the conductance is suppressed.

effects that require that the quantum dot is tunnel coupled to two ferromagnetic leads, and therefore can only be observed in quantum-dot spin valves.

We already mentioned the *tunnel magnetoresistance* (TMR) to be one of the two effects allowing the realization of spin valves. As a result, the TMR effect is not just some effect visible in the quantum-dot spin valve, but instead it is the effect that defines a quantum-dot system with ferromagnetic leads as a quantum-dot spin valve. We introduce the TMR and its discovery here, and then give an extensive discussion during our results in Sec. 6.2. The TMR effect was first discovered by Julliere in ferromagnetic films and is attributed to different transport properties depending on the magnetization directions of the two leads [19]. It can be understood from the densities of states at the Fermi energy of two ferromagnets. A sketch of the parallel and antiparallel setups of a single tunnel junction is shown in Fig. 1.4. In the parallel setup (where the angle between the ferromagnets' magnetizations is $\theta = 0$) the conductance through the system is high, since transport happens from the majority to the majority spin channel as well as from the minority to the minority spin channel. In the antiparallel setup (where $\theta = \pi$), however, spins are transported from the majority to minority channel and from the minority to the majority channel. As a result, in the parallel setup the majority channel is dominating, while in the antiparallel setup the minority channel dominates transport, leading to different conductances depending on the angle between the magnetizations. There are several definitions of the TMR being used. Throughout this work we choose to define it as follows:

$$\text{TMR} = \frac{I_p - I_{\text{ap}}}{I_p}, \quad (1.1)$$

where I_p is the current through the system with the magnetizations of the leads

being parallel, and I_{ap} is the current in the antiparallel setup. For a single tunnel junction Julliere found that the TMR is described solely by the polarization p of the magnetic leads. Julliere's value of the TMR is often used as a point of reference in this work. When using the definition from Eq. (1.1) Julliere's value is given by

$$\text{TMR}^{\text{Jull}} = \frac{2p^2}{1+p^2}. \quad (1.2)$$

This value is easily derived from the fact that the transmission through the junction for a given spin is proportional to the corresponding density of states in the source and the drain, respectively, and the latter are proportional to $1+p$ for the majority and $1-p$ for the minority spins. (We note that, in our definition of the TMR, we normalize with the current for the parallel configuration. Another common definition uses the current for the antiparallel configuration as normalization, which would give $\text{TMR}^{\text{Jull}} = 2p^2/(1-p^2)$.) Since the first discovery of the effect it was possible to construct spin valves with ever-increasing TMR values, especially in magnetic-layer structured spin valves. There TMR values of up to several hundred percent have been achieved at room temperature [20–22]. At low temperatures ($T < 5$ K), and using graphene heterostructures, TMR values of over 10⁴% were observed [23, 24]. Spin valves based on the TMR effect already found application in read heads of hard discs, magnetic sensors as well as in magnetoresistive random access memory devices (MRAM), providing fast writing and reading as well as long-lasting performance [25]. Quantum-dot spin valves usually exhibit TMR values of the order of Julliere's value, but allow us to realize highly tunable spin-valve devices, where the TMR depends strongly on the different system parameters. This is due to the fact, that the TMR is strongly influenced by the possibility to accumulate a finite spin polarization on the quantum dot. The spin accumulation has the tendency to weaken the spin-valve effect, i.e., to reduce the TMR. The value of the dot's spin polarization, on the other hand, results from an interplay of various processes that either lead to a spin accumulation or that provide a relaxation channel for the accumulated spin. This makes the TMR a highly nontrivial function of temperature, gate- and bias voltage, and Coulomb interaction, which we show during Sec. 6.2

The second effect attributed to the magnetized, ferromagnetic leads that we discuss here is the *exchange field effect*. It emerges when the quantum dot is interacting and coupled to spin-polarized leads [26]. It manifests as an interaction-induced spin precession on the quantum dot, that can be described – up to first order in the tunnel coupling Γ – via a magnetic field that is highly dependent on system parameters. The effects of this local exchange field become e.g. visible via a significant dependence of the conductance on the angle enclosed by the leads' magnetizations [26, 27] or as a splitting of the Kondo peak [28].

To understand the origin of the effect, we assume a singly-occupied quantum dot, that is coupled to ferromagnetic leads with parallel magnetizations. If the Coulomb interaction is very large, double occupation of the quantum dot is suppressed. However, due to tunneling between the leads and the quantum dot, transport is still possible and causes quantum charge fluctuations. These fluctuations depend strongly

on the spin of the electron on the quantum dot: If the electron is of majority spin it is able to tunnel easier between leads and quantum dot, than an electron of minority spin. As a result, spin degeneracy is lifted via an exchange interaction between the electrons spin and the ferromagnetic leads [29]. It was shown experimentally, as well as theoretically, that the effect can be measured by cancelling the exchange field with an external magnetic field in opposite direction [14, 27] or it can be probed via an additional superconducting lead [30].

1.1.3 Superconducting Leads and Double Quantum Dots

Up to now we introduced the single-electron transistor and the quantum-dot spin valve, but quantum-dot systems are a lot more versatile than the two examples we introduced: Firstly, different materials for the leads are possible, which have an important role on the system's transport properties, as we mentioned before. Secondly, one is not limited to a single quantum dot, but systems including multiple quantum dots are feasible and under research.

We showed that ferromagnetic leads cause new effects, like the TMR and the exchange field, to emerge. Ferromagnetism is a collective effect that occurs due to a spontaneous symmetry breaking once the material is cooled below the Curie temperature. The new effects are then caused by the leads' order parameters, i.e. their magnetizations. Of course, ferromagnetism is not the only such effect, another one would be superconductivity. This is, again, an effect that occurs due to a spontaneous symmetry breaking once the material cooled to temperatures lower than the critical temperature. The physical order parameter is now the superconductor's pair condensate, which one would expect to lead to new effects in quantum-dot systems when the leads are chosen to be superconducting. It is therefore not surprising that such a system is under heavy investigation [31, 32]. The particles partaking in electronic transport in superconductors are Cooper pairs, electron-electron pairs that interact via phonons, and quasiparticles, which are unbound electrons that broke away from the Cooper-pair condensate [33]. The density of states of a superconductor is characterized by a gap of size $2|\Delta|$ around the Fermi level, in which transport is suppressed. If superconducting leads are tunnel coupled to a quantum dot, they impose unique effects on the system as a whole. Two prominent examples for such effects are *Andreev Bound States* and *Multiple Andreev Reflections* [34–36]. To explain Andreev Bound States, we assume an electron on the quantum dot with energy below the gap of the superconductors. If the electron attempts to tunnel from the dot into one of the leads it is reflected as its time-reversed particle (a hole). This process is called *Andreev reflection*. The hole is again reflected on the other side back into an electron, resulting in two discrete subgap states of electron-hole pairs with opposite spins, which are referred to as Andreev Bound States [34, 37]. Via multiple Andreev reflections it is then possible to transfer Cooper pairs through the quantum dot, effectively allowing superconducting transport through the quantum dot system [38]. If this is combined with the Kondo effect, it is actually possible to reach a conductance larger than the conductance quantum $G = 2e^2/h$ [35]. We

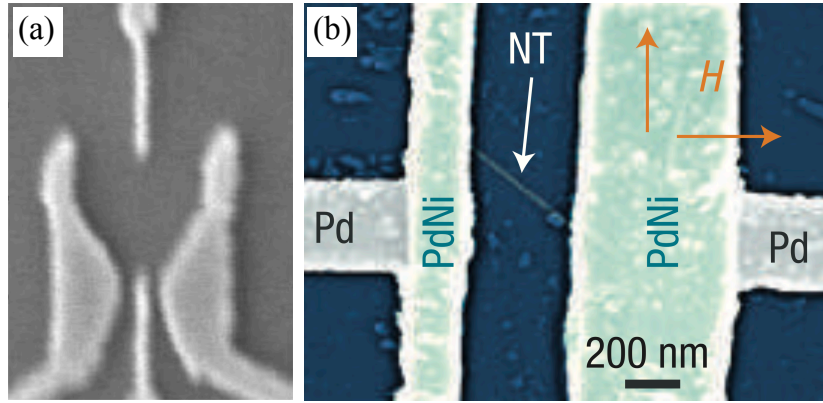


Figure 1.5: (a) Scanning electron micrograph of a lateral device consisting of a single quantum dot. The top of the surface is in dark gray, while the gates are depicted in light gray, taken from Ref. [45]. The quantum dot is located at the middle of the device. (b) Scanning electron micrograph picture of a nanotube setup for a quantum dot, coupled to PdNi leads. The arrow labeled NT points at the carbon nanotube, taken from Ref. [46].

stop short to note that *hybrid structures*, where the leads are of different materials, are under consideration. Systems with e.g. one normal and one superconducting lead or two ferromagnetic leads coupled to a quantum dot, together with a third superconducting lead are discussed [39, 40].

When working with systems including multiple quantum dots, the geometry of the setup becomes crucial. Even for the easiest case, a double quantum-dot system, two different geometries are possible, either the quantum dots are connected in series or in parallel [41]. Such systems have been discussed experimentally as well as theoretically, since they are strong contenders for spin-based qubits [42]. It was also shown, that a serial double quantum dot coupled to normal metallic leads, can be mapped to a system including one quantum dot with one ferromagnetic lead [43]. As a result, the quantum-dot spin valve, where one quantum dot is coupled to two ferromagnetic leads, is closely related to a double quantum-dot system, which also shows in a comparison between the two [44].

1.2 Experimental Realizations of Quantum-Dot Spin Valves

Experimental investigations of transport through quantum-dot systems are far from trivial. Due to the smallness of the systems under investigation, impurities and disorder have a huge impact on the setup's characteristics. The actual quantum dot can be realized in different ways, e.g. lateral and vertical quantum dot setups or systems where a carbon nanotube behaves as a quantum dot, which is the case

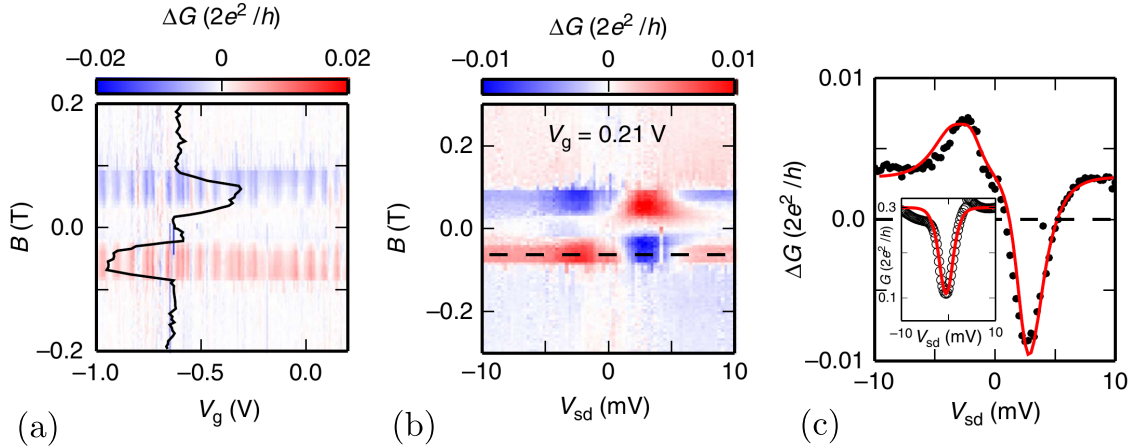


Figure 1.6: (a) The spin signal ΔG as a function of the external magnetic field B and the gate voltage V_g in the linear bias regime. The black line corresponds to a cut at $V_g = -0.85$ V. (b) The spin signal as a function of the external magnetic field and the bias voltage V_{sd} at a fixed gate voltage $V_g = 0.21$ V. The dashed line labels the cut at $B = -0.75$ mT that is shown in (c). The dots are experimental data, and the red line are theoretical predictions. All panels are taken from Ref. [13]

for high contact resistances [47]. Two exemplary quantum-dot setups are shown in Fig. 1.5, where panel (a) is a scanning electron micrograph of a lateral quantum-dot device, taken from Ref. [45]. The basis of this setup is a GaAs/AlGaAs heterostructure, where the AlGaAs is doped with Si to introduce free electrons, that form a 2D electron gas at the surface between the two materials. This 2D electron gas is then manipulated by applying gates (shown in light gray) on top of the heterostructure, creating a small, isolated island acting as the quantum dot [48]. Another realization is e.g. via growing self-assembled InAs quantum dots on a GaAs/AlGaAs heterostructure [49, 50] which are then contacted by leads. In panel (b) on the other hand we show a setup using a carbon nanotube that is coupled to PdNi leads, taken from Ref. [46]. The nanotubes are usually grown by chemical vapor deposition on Si substrates and are then applied to the leads via lithographic methods [46, 51].

For quantum-dot spin valves it has shown that the accumulation of electron spin on the quantum dot is the basis for many effects occurring in the system. This has become apparent in Ref. [52], where an effectively 0D aluminum island is tunnel-coupled to four cobalt terminals. Spin accumulation on the island is achieved by injecting electron spin via a tunneling current through two of the terminals. When a magnetic field is applied in-plane it was possible to measure a TMR, while a perpendicular magnetic field leads to precession of the accumulated spin. In Ref. [13] the spin accumulation and the spin's precession in a quantum-dot spin valve were studied in detail with a focus on a noncollinear setup. The quantum-dot was fabricated via a carbon nanotube, which was then tunnel-coupled to two PdNi electrodes. The

electrodes are positioned at an angle $\theta = \pi/2$ to ensure that their magnetizations are noncollinear. It is pointed out that the setup of the leads' magnetizations causes an a priori spin precession. An external magnetic field can be applied parallelly to the drain's magnetization axis (and therefore perpendicular to the source's). By measuring the conductance G while increasing and after that decreasing the magnetic field for several gate (V_g) and bias voltages (V_{sd}) leads to the pictures seen in Figs. 1.6 (a) and (b), where the spin signal $\Delta G = G_{\text{trace}} - G_{\text{retrace}}$ is given by the difference between the conductance measured while increasing the magnetic field and while decreasing it. In Fig. 1.6 (a) ΔG is studied as a function of the gate voltage and the magnetic field in the linear bias regime, $k_B T > eV_{sd}$. One finds clear stripes, where ΔG is positive or negative which show that hysteresis between trace and retrace of the magnetic field is modulated regularly for different gate voltages. In Fig. 1.6 (b) the linear bias regime is left and the spin signal is studied as a function of the bias voltage and the magnetic field. The gate voltage is fixed for this measurement. As can be seen, it is possible to change the sign of the spin signal, by tuning the bias voltage. This is emphasized in panel (c), which shows a cut through panel (b) along the dashed line at $B = -75\text{mT}$. One finds a nearly antisymmetric curve, where the in the high-voltage regime spin relaxation and spin accumulation are in balance. For intermediate bias voltages, out-of-equilibrium spin precession governs the spin signal. The spin precession is controlled by the exchange field, the external magnetic field and the total relaxation time of the dot's spin. In this experiment, the latter is dominated by the relaxation caused by the contacts. This contact-induced relaxation effect depends strongly on the bias voltage, which makes it possible to control spin precession simply by changing the bias voltage. All panels of Fig. 1.6 as well as the description and interpretation of the experiment are taken from Ref. [13].

Since we already referred to the indirect measurement of the exchange field, by compensating it via an external magnetic field, we also take the time and discuss this particular experiment in more detail. In Ref. [28] a splitting of the Kondo peak caused by the exchange field was observed for C_{60} atoms within a Ni gap. This result can be reproduced for a single-wall carbon nanotube acting as a quantum dot, coupled to pure Ni electrodes [14]. One of the main benefits of this setup is that it is possible to gate the carbon nanotube, allowing to tune the exchange field via a gate voltage. Since the exchange field visibly manifests in a splitting of the Kondo peak, the system is cooled down beneath the Kondo temperature T_K and measurements are taken at 30 mK in a $^3\text{He}/^4\text{He}$ dilution refrigerator. The differential conductance as a function of gate and bias voltage have already been shown in Fig. 1.3 with Kondo peaks visible in the odd Coulomb diamonds at zero bias. Applying an external magnetic field to the setup, it is possible to record the splitting of the Kondo peak as a function of the magnetic field, see Fig. 1.7(a). This is achieved by sweeping the external magnetic field from highly negative to highly positive values. It is obvious that the splitting of the Kondo peak is compensated at $B \approx \pm 1.12T$, giving the desired indirect measurement of the exchange field strength. It is noted that, for a second device, the Kondo peaks do not intersect, which hints at the exchange field

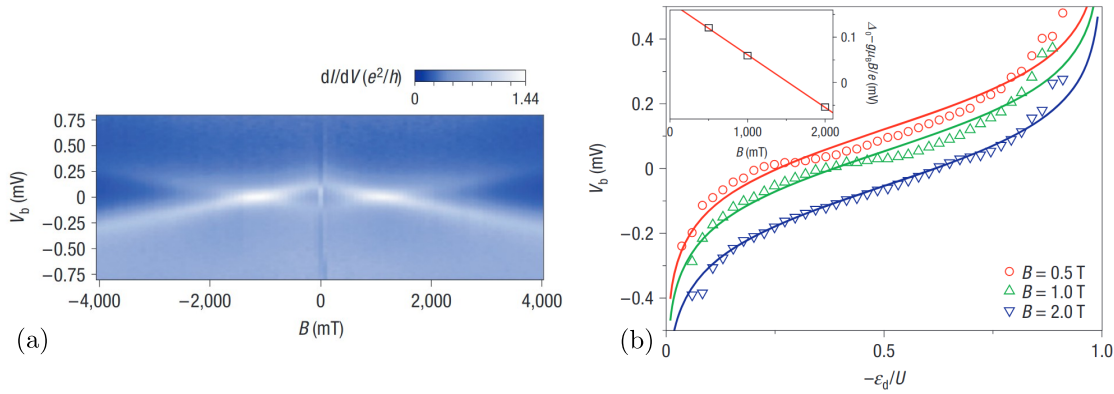


Figure 1.7: (a) Differential conductance as a function of both the bias voltage and the external magnetic field. The change of the splitting of the Kondo peak is clearly visible. The splitting is compensated at $B \approx 1.12$ T. (b) Renormalization of the quantum dot's level position caused by the exchange field. The peak position is plotted as a function of the level energy and the bias voltage for different magnetic fields. Both are taken from Ref. [14].

standing at an angle to the external magnetic field. Additionally, it is possible to measure the renormalization of energy levels caused by the exchange field via the majority spin peak positions in the differential conductance as functions of both bias and gate voltage within one Coulomb diamond. The result can be seen in Fig. 1.7(b), with symbols being data from measurements and the lines a fit predicted by a first order perturbation theory in Γ . The inset is used to determine a parameter for the fit. On the left side of the Coulomb diamond the dot is emptied with one electron, while on the right side it is filled with an additional electron. As can be seen, the level is shifted down on the left of the Coulomb diamond. This is because a majority spin can easily leave the quantum dot, but can only tunnel on the quantum dot if the dot is occupied with a minority spin due to Pauli's exclusion principle. As a result the minority spin is lowered beneath the majority spin level, on the right. Both panels of Fig. 1.7 as well as the description and interpretation of the experiment are taken from Ref. [14].

1.3 Structure of this Thesis

We started this thesis with a general overview of quantum-dot systems and the discussion of some prominent effects manifesting in these setups, including Coulomb blockade, Kondo effect, TMR and exchange field. The further structure of this thesis is as follows. In Chap. 2 we introduce the basic mathematical formalism to treat fermionic systems out of equilibrium. For this we introduce the Keldysh contour and nonequilibrium Green functions, general concepts that can be applied to any nonequilibrium many-body problem. To allow for a study of fermionic systems

within a path-integral formalism, we introduce the Grassmann algebra and fermionic coherent states and derive several useful identities. We introduce the Hamiltonian of the quantum-dot spin valve in detail throughout Chap. 3 and make use of the nonequilibrium Green function formalism to derive analytic formulas for the current through the noninteracting quantum-dot spin valve as well as its occupation number and spin projection. The chapter is rounded off by a discussion of several theoretical approaches to the problem of spin-dependent transport through an interacting quantum-dot system, allowing a classification of the ISPI formalism. Since the ISPI technique is based on the path-integral formalism, we demonstrate how to construct the path integral to calculate the partition function of the quantum-dot spin valve in Chap. 4. We explain how to incorporate interactions via a discrete Hubbard-Stratonovich transformation and discuss how source terms are able to break time-inversion symmetry of the Keldysh contour specifically to allow for the calculation of the expectation values of time-local observables. We explicitly show the source terms necessary to calculate the current, occupation number of the quantum dot and its spin projections. In Chap. 5 we then introduce the ISPI formalism and discuss the necessary approximations. We first demonstrate how the finite-time implementation of the ISPI technique is derived. After that we show how the ISPI technique can be mapped to a transfer-matrix approach, leading to the new transfer-matrix implementation. To receive numerically exact results from the ISPI technique, one has to apply a convergence procedure to eliminate systematic errors. We introduce this procedure and also add some remarks on the parallelization capabilities and performance of the method at the end of the chapter. The results for electronic transport through a quantum-dot spin valve obtained from the ISPI technique are showcased in Chap. 6. We first convince ourselves that the ISPI technique returns reliable data, by benchmarking it against two limiting cases: the noninteracting case and the high-temperature regime, where we compare our ISPI data with results from a perturbation theory in the tunneling. After that we turn to a setup where the leads' magnetization directions are aligned collinearly, and demonstrate that the TMR is heavily impacted by resonant tunneling contributions. In a next step, we study effects introduced by noncollinear lead magnetizations together with an external magnetic field, acting on the quantum dot. Here we find asymmetries in the conductance, caused by the violation of particle/hole symmetry. Finally, we conclude in Chap. 7.

Throughout this work we set $\hbar = 1$ to increase readability of the formulas.

2 Theoretical Concepts for Fermionic Systems in Nonequilibrium

In this chapter we discuss the theoretical concepts necessary for the remainder of this work. Throughout this thesis we study systems in nonequilibrium. Therefore, we present the mathematical framework necessary to treat systems in nonequilibrium in the first half of this chapter. These concepts are very general and not limited to a specific system nor to a particular process that drives the system out of equilibrium. We introduce the Keldysh formalism, on which we rely heavily throughout this thesis. It allows us to treat nonequilibrium systems by propagating along a closed-time contour, leading to a doubling of the system's degrees of freedom. First we show the reasoning behind the Keldysh contour, and then continue by introducing the notion of the nonequilibrium Green function as well as the Keldysh rotation. Finally, we present some useful identities involving nonequilibrium Green functions, including the well known Langreth theorem.

Since we are studying electronic transport through quantum-dot systems, the particles under consideration are electrons and hence fermions. To take the fermionic nature of the particles into account, it is necessary to require that the creation and annihilation operators obey anti-commutation relations, given by

$$\begin{aligned}\{c_\alpha, c_\beta\} &= 0, \\ \{c_\alpha^\dagger, c_\beta^\dagger\} &= 0, \\ \{c_\alpha, c_\beta^\dagger\} &= \delta_{\alpha\beta},\end{aligned}\tag{2.1}$$

where $\{\cdot, \cdot\}$ denotes the anti-commutator, and $c_\alpha, c_\alpha^\dagger$ are the annihilation and creation operators of the system, respectively. The indices α and β denote the quantum mechanical state in which an electron is annihilated or created. The method used in this thesis is based on path integrals in the basis of fermionic coherent states. Due to the anti-commutation relations the fermionic coherent states are closely connected to the Grassmann algebra, which gives rise to anti-commuting numbers, called Grassmann numbers. During the second half of this chapter we, thus, introduce the Grassmann algebra as well as some useful identities involving Grassmann numbers and then continue to introduce fermionic coherent states, again, with additional identities that are used throughout the thesis.

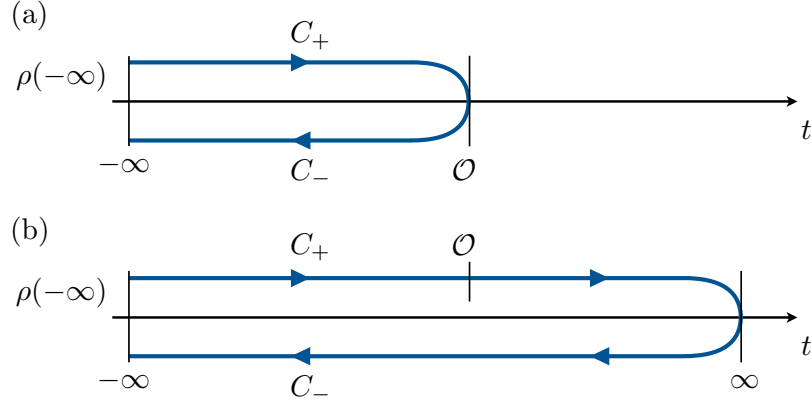


Figure 2.1: The Keldysh contour with the two branches C_{\pm} for the forward (+) and backward (-) propagation. The arrows indicate the propagation direction along the contour, the initial density matrix is $\rho(-\infty)$, and at some point in time the observable of interest \mathcal{O} is measured. In panel (a) the propagation stops at the operator \mathcal{O} , while for panel (b) the propagation is extended to $t \rightarrow \infty$. In this case the operator \mathcal{O} is placed on the upper contour C_+ here.

2.1 Keldysh Contour

Usually when investigating equilibrium setups, the system under consideration is evolved from a noninteracting state in the distant past, that is described by the density matrix $\rho(t \rightarrow -\infty) = \rho(-\infty)$, to a state where interactions reach their physical strength by switching them on adiabatically. Once the system is fully interacting, the observable \mathcal{O} is measured at time t . Some time after that, interactions are again adiabatically switched off until the time evolution reaches a point in the distant future where the system returns to its initial state. Since the system was in equilibrium throughout this procedure, the initial and final states are both known, which allows us to calculate the expectation value of the observable \mathcal{O} . In a nonequilibrium setup, however, even when we switch off interactions in the distant future, fluctuations occurred during the time evolution and it is impossible to know the final state at $t \rightarrow \infty$. The Keldysh formalism allows us to treat systems out of equilibrium nonetheless, at the cost of doubling the degrees of freedom. In this section we give a short introduction to the basic idea of the Keldysh contour, where we follow the derivation given in Refs. [53, 54].

We return to a quantum many-body system that in the distant past $t \rightarrow -\infty$ is noninteracting and in a state described by the density matrix $\rho(-\infty)$. The system is governed by a time-dependent Hamiltonian $\mathcal{H}(t)$, that on one hand includes the adiabatic switch-on process of the interactions, and on the other hand includes a true time dependence, e.g. due to an external field, that drives the system out of equilibrium. The switch-on process is similar to the one we described before,

meaning that starting from the system in state $\rho(-\infty)$, the interactions are switched on adiabatically. Some time after interactions reached their full strength, some operator \mathcal{O} is measured. The expectation value of this operator at time t is in general given by

$$\langle \mathcal{O}(t) \rangle = \frac{\text{tr} [\mathcal{O}\rho(t)]}{\text{tr} [\rho(t)]}. \quad (2.2)$$

The well-known Von Neumann equation defines the time evolution of the density matrix, where we emphasize that the density matrix is understood to be taken in the Schrödinger picture

$$\partial_t \rho(t) = -i [\mathcal{H}(t), \rho(t)], \quad (2.3)$$

with $[\cdot, \cdot]$ denoting the commutator. The Von Neumann equation is solved by introducing a unitary evolution operator $\mathcal{U}_{t,t'}$ such that [53, 54]

$$\rho(t) = \mathcal{U}_{t,-\infty} \rho(-\infty) \mathcal{U}_{t,-\infty}^\dagger = \mathcal{U}_{t,-\infty} \rho(-\infty) \mathcal{U}_{-\infty,t}. \quad (2.4)$$

where we employed unitarity and the fact that $[\mathcal{U}_{t,t'}]^{-1} = \mathcal{U}_{t',t}$. Since the Hamiltonian is time dependent, the evolution operator has to be constructed as an infinite product of short-time evolution operators. Each of these operators propagates the system over one time slice of length δ_t , during which the Hamiltonian is assumed to be constant. This is known as the Suzuki-Trotter formula, which is used multiple times throughout this work [55, 56]

$$\mathcal{U}_{t,t'} = \lim_{N \rightarrow \infty} e^{-i\mathcal{H}(t-\delta_t)\delta_t} \cdot \dots \cdot e^{-i\mathcal{H}(t-N\delta_t)\delta_t} \cdot e^{-i\mathcal{H}(t')\delta_t} = \mathcal{T} e^{-i \int_{t'}^t \mathcal{H}(\tau) d\tau}, \quad (2.5)$$

with \mathcal{T} being the time-ordering operator. From this definition of the evolution operator it is immediately clear that $\mathcal{U}_{t,t_1} \mathcal{U}_{t_1,t'} = \mathcal{U}_{t,t'}$. Plugging the solution of the Von Neumann equation, Eq. (2.4) back into Eq. (2.2) results in

$$\begin{aligned} \langle \mathcal{O}(t) \rangle &= \frac{1}{\text{tr} [\rho(-\infty)]} \text{tr} [\mathcal{O} \mathcal{U}_{t,-\infty} \rho(-\infty) \mathcal{U}_{-\infty,t}] \\ &= \frac{1}{\text{tr} [\rho(-\infty)]} \text{tr} [\mathcal{U}_{-\infty,t} \mathcal{O} \mathcal{U}_{t,-\infty} \rho(-\infty)], \end{aligned} \quad (2.6)$$

where we made use of the cyclicity of the trace. Reading from right to left, we start with the density matrix at time $-\infty$. This state is then propagated forward in time via $\mathcal{U}_{t,-\infty}$ until we reach the measurement time t , where the operator \mathcal{O} is located. After that we propagate in the opposite direction back to the time $-\infty$ via $\mathcal{U}_{-\infty,t}$. As a result, the system is propagated along a contour of the style seen in Fig. 2.1 (a). The contour has two branches C_ν , one for forward propagation in time ($\nu = +$) and one for backward propagation ($\nu = -$). In this formulation the operator \mathcal{O} is positioned directly on the turning point of the contour. To avoid finite size effects it is useful to extend the contour further to $t \rightarrow \infty$, when working with path integrals. This is achieved by inserting $\mathbb{1} = U_{t,\infty} U_{\infty,t}$ to the left of the operator

\mathcal{O} [54]

$$\begin{aligned} \langle \mathcal{O}(t) \rangle &= \frac{1}{\text{tr}[\rho(-\infty)]} \text{tr} [\mathcal{U}_{-\infty,t} \mathcal{U}_{t,\infty} \mathcal{U}_{\infty,t} \mathcal{O} \mathcal{U}_{t,-\infty} \rho(-\infty)] \\ &= \frac{1}{\text{tr}[\rho(-\infty)]} \text{tr} [\mathcal{U}_{-\infty,\infty} \mathcal{U}_{\infty,t} \mathcal{O} \mathcal{U}_{t,-\infty} \rho(-\infty)], \end{aligned} \quad (2.7)$$

where we made use of $\mathcal{U}_{-\infty,t} \mathcal{U}_{t,\infty} = \mathcal{U}_{-\infty,\infty}$. The contour is now expanded, such that after reaching the measurement time t on the forward propagation, we do not immediately propagate back in time. Instead, the forward propagation is continued to $t \rightarrow \infty$, and then one propagates all the way back to $t \rightarrow -\infty$. Note that the operator \mathcal{O} was placed on the forward branch C_+ , but could just as well be placed on the backward branch, if the unit operator is inserted to the right of the operator \mathcal{O} . In total the system evolves along a closed time contour, the so called *Keldysh contour* that is depicted in Fig. 2.1 (b).

2.2 Nonequilibrium Green Functions

As we just demonstrated, treating out-of-equilibrium systems on the Keldysh contour requires a doubling of the degrees of freedom. Consequently, a point in the physical time t is not defined uniquely anymore. Instead, at each physical time t , we can either be on the upper contour C_+ or on the lower C_- (cf. Fig. 2.1). To account for this Keldysh structure, we introduce Keldysh-time which provides a clear notation, given by

$$\tilde{t} = (t, \nu), \quad (2.8)$$

where t specifies the physical time and $\nu = \pm$ the Keldysh branch on which the time resides. It is understood that $\tilde{t} > \tilde{t}'$ means that \tilde{t} resides later on the Keldysh contour than \tilde{t}' . This especially means that elements on the lower contour are always larger than those on the upper contour.

When studying a system in equilibrium, Green functions have proven to be a very useful tool. In many-body theory Green functions are understood to be propagators, since they give the amplitude of a particle to propagate from a state β at time t' to a state α at time t [33]. Therefore, the Green function is given as the expectation value of a pair of creation and annihilation operators at times t and t' . The time-ordered Green function is then defined as

$$G_{\alpha\beta}^T(t, t') = -i \left\langle \mathcal{T} c_{\alpha}(t) c_{\beta}^{\dagger}(t') \right\rangle. \quad (2.9)$$

In a nonequilibrium scenario, this is not sufficient, especially the time-ordering operator \mathcal{T} is not clearly defined anymore. But one is able to show, that the perturbation expansion of the nonequilibrium Green function has the exact same structure as the $T = 0$ expansion of the equilibrium Green function [53, 57], instead of the time ordering operator the contour ordering operator has to be used, though. The contour ordering operator \mathcal{T}_C orders operators along the Keldysh contour, similarly to the

time ordering along the physical time, such that operators that reside later on the contour are moved to the left of those that are earlier on the contour. This enables us to define the contour-ordered Green function [53, 58]

$$G_{\alpha\beta}(\tilde{t}, \tilde{t}') = G_{\alpha\beta}^{\nu\nu'}(t, t') = -i \left\langle \mathcal{T}_C c_\alpha(\tilde{t}) c_\beta^\dagger(\tilde{t}') \right\rangle. \quad (2.10)$$

Depending on the combination of ν and ν' , there are four different possibilities for how the contour ordering acts on the operators:

$$G_{\alpha\beta}^{\nu\nu'}(t, t') = \begin{cases} -i \left\langle \mathcal{T} c_\alpha(t) c_\beta^\dagger(t') \right\rangle & \text{for } \nu = +, \nu' = + \\ i \left\langle c_\beta^\dagger(t') c_\alpha(t) \right\rangle & \text{for } \nu = +, \nu' = - \\ -i \left\langle c_\alpha(t) c_\beta^\dagger(t') \right\rangle & \text{for } \nu = -, \nu' = + \\ -i \left\langle \tilde{\mathcal{T}} c_\alpha(t) c_\beta^\dagger(t') \right\rangle & \text{for } \nu = -, \nu' = - \end{cases} \quad (2.11)$$

We are able to identify these four expressions as familiar Green functions: The first is the time-ordered Green function, the second the lesser, the third the larger and the fourth is the anti-time-ordered Green function. As a result, one is able to write the nonequilibrium Green function as a 2×2 matrix in Keldysh space, given by

$$\mathbf{G}_{\alpha\beta}(t, t') = \begin{pmatrix} G_{\alpha\beta}^T(t, t') & G_{\alpha\beta}^<(t, t') \\ G_{\alpha\beta}^>(t, t') & G_{\alpha\beta}^{\tilde{T}}(t, t') \end{pmatrix}. \quad (2.12)$$

We denote 2×2 matrices in Keldysh space with bold letters in what follows.

2.2.1 Properties of Nonequilibrium Green Functions

The nonequilibrium Green function has some intrinsic properties that directly follow from relations of its elements. We add properties, that are necessary for further derivations. First, we note that from their definition in Eq. (2.11) the lesser and larger Green functions are both anti-Hermitian, $[G_{\alpha\beta}^<(t, t')]^* = -G_{\beta\alpha}^<(t', t)$ and $[G_{\alpha\beta}^>(t, t')]^* = -G_{\beta\alpha}^>(t', t)$. Both the time ordered and the anti-time ordered Green function can be expressed in terms of lesser and larger Green functions

$$\begin{aligned} G_{\alpha\beta}^T(t, t') &= \theta(t - t') G_{\alpha\beta}^>(t, t') + \theta(t' - t) G_{\alpha\beta}^<(t, t'), \\ G_{\alpha\beta}^{\tilde{T}}(t, t') &= \theta(t' - t) G_{\alpha\beta}^>(t, t') + \theta(t - t') G_{\alpha\beta}^<(t, t'), \end{aligned} \quad (2.13)$$

where the Heaviside step function $\theta(x)$ is defined as $\theta(x) = 0$ if $x < 0$ and $\theta(x) = 1$ if $x > 0$. For $\theta(0)$ it is useful to deviate from the usual definition where $\theta(0) = 1$. Instead, we define $\theta(0) = \frac{1}{2}$, which can be justified by using the common integral representation for the Heaviside step function

$$\theta(x) = \lim_{\epsilon \rightarrow 0} \frac{1}{2\pi i} \int_{-\infty}^{\infty} \frac{e^{-ixt}}{t - i\epsilon} dt. \quad (2.14)$$

Setting $x = 0$ in the equation above and making use of the identity $\lim_{\epsilon \rightarrow 0} \frac{1}{t - i\epsilon} = \mathcal{P} \frac{1}{t} + i\pi\delta(s)$ (see Ref. [59], \mathcal{P} denotes the principal value), one readily comes to the result that $\theta(0) = \frac{1}{2}$. A direct consequence of Eqs. (2.13) is that the four entries of the nonequilibrium Green function are not independent. Indeed, they fulfill the following relation

$$G_{\alpha\beta}^T(t, t') + G_{\alpha\beta}^{\tilde{T}}(t, t') = G_{\alpha\beta}^>(t, t') + G_{\alpha\beta}^<(t, t'). \quad (2.15)$$

In addition, we are able to define retarded (R), advanced (A) and Keldysh (K) Green functions with respect to the lesser and larger Green functions

$$\begin{aligned} G_{\alpha\beta}^R(t, t') &= \theta(t - t') [G_{\alpha\beta}^>(t, t') - G_{\alpha\beta}^<(t, t')] \\ G_{\alpha\beta}^A(t, t') &= \theta(t' - t) [G_{\alpha\beta}^<(t, t') - G_{\alpha\beta}^>(t, t')] \\ G_{\alpha\beta}^K(t, t') &= G_{\alpha\beta}^<(t, t') + G_{\alpha\beta}^>(t, t'). \end{aligned} \quad (2.16)$$

With these definitions and the anti-Hermiticity of lesser and larger Green functions, it is easy to see that $[G_{\alpha\beta}^R(t, t')]^* = G_{\beta\alpha}^A(t', t)$ and $[G_{\alpha\beta}^K(t, t')]^* = -G_{\beta\alpha}^K(t', t)$.

2.2.2 Keldysh Rotation

Since the four entries of the nonequilibrium Green functions are not independent of one another we are able to perform a linear transformation, called *Keldysh rotation*, that eliminates one of the four entries. There are two versions of the Keldysh rotation that are commonly used. One is given in Ref. [60], while the other is used e.g. in Ref. [57, 61]. Both are based on an involutory transformation matrix, with the exact form of the matrix differing for the two cases. We make use of both of these transformations throughout this thesis. When discussing the path-integral formalism (see Chap. 4) the first rotation is the starting point for a description of the free Green functions of the leads and the quantum dot. The second convention is what Langreth theorem is based upon and therefore finds use when we derive the noninteracting, analytical solution for the current through the quantum-dot spin valve (see Sec. 3.2). Having two very different approaches which should lead to the same results, gives us the possibility to compare data from both to be sure that there are no inherent issues.

For fermionic systems, it is customary to apply different transformation matrices from the left and from the right. This convention was first introduced by Larkin and Ovchinnikov [60]. Following them, we apply a 2×2 transformation matrix in Keldysh space \mathbf{U} from the left and the matrix $\kappa_z \mathbf{U}^{-1}$ from the right, where κ_z is a Pauli matrix in Keldysh space. As a result, the Keldysh rotation takes the following form

$$\mathbf{G}'_{\alpha\beta}(t, t') = \mathbf{U} \mathbf{G}_{\alpha\beta}(t, t') \kappa_z \mathbf{U}^{-1}. \quad (2.17)$$

For the first case the transformation matrix \mathbf{U} is given by $\mathbf{U} = 1/\sqrt{2} \begin{pmatrix} 1 & 1 \\ 1 & -1 \end{pmatrix}$, and of course $\mathbf{U}^{-1} = \mathbf{U}$ due to the involution. With this the transformed nonequi-

ilibrium Green function takes the form

$$\mathbf{G}'_{\alpha\beta}(t, t') = \begin{pmatrix} G_{\alpha\beta}^R(t, t') & G_{\alpha\beta}^K(t, t') \\ 0 & G_{\alpha\beta}^A(t, t') \end{pmatrix}. \quad (2.18)$$

For the case used by Langreth the transformation matrix takes the form $\mathbf{U} = \begin{pmatrix} 1 & 0 \\ 1 & -1 \end{pmatrix}$ and again $\mathbf{U}^{-1} = \mathbf{U}$. After this transformation, the resulting Green function is given by

$$\mathbf{G}'_{\alpha\beta}(t, t') = \begin{pmatrix} G_{\alpha\beta}^R(t, t') & G_{\alpha\beta}^<(t, t') \\ 0 & G_{\alpha\beta}^A(t, t') \end{pmatrix}. \quad (2.19)$$

The fact that for both cases one element vanishes is a direct consequence of the identity in Eq. (2.15).

2.2.3 Langreth Theorem

As a final identity we introduce the well-known Langreth theorem [62, 63]. When working with perturbation expansions (see e.g. App. A) we often encounter expressions of the form

$$\mathbf{C}(t, t') = \int dt_1 \mathbf{A}(t, t_1) \mathbf{B}(t_1, t'), \quad (2.20)$$

where \mathbf{A} , \mathbf{B} and \mathbf{C} are all 2×2 matrices in Keldysh space in the basis given in Eq. (2.19). Usually, we are then interested in one of the matrix elements of the resulting matrix \mathbf{C} . Langreth theorem relates the elements of the resulting matrix to the elements of the initial matrices \mathbf{A} and \mathbf{B} . The identities take the following form

$$\begin{aligned} C^{R/A}(t, t') &= \int dt_1 A^{R/A}(t, t_1) B^{R/A}(t_1, t') \\ C^<(t, t') &= \int dt_1 (A^R(t, t_1) B^<(t_1, t') + A^<(t, t_1) B^A(t_1, t')). \end{aligned} \quad (2.21)$$

There are two ways to prove Langreth theorem. One is rather straight forward: we switch to Fourier space, where the convolution simplifies to a product. Keeping in mind that the Green functions are invariant under time translations as stated before, we find for Eq. (2.20) in Fourier space

$$\mathbf{C}(\omega) = \mathbf{A}(\omega) \mathbf{B}(\omega). \quad (2.22)$$

This is a simple matrix product, and the three elements of \mathbf{C} take the form

$$\begin{aligned} C^{R/A}(\omega) &= A^{R/A}(\omega) B^{R/A}(\omega) \\ C^<(\omega) &= A^R(\omega) B^<(\omega) + A^<(\omega) B^A(\omega). \end{aligned} \quad (2.23)$$

which is the same structure as in Eqs. (2.21). Indeed, when Eqs. (2.21) are Fourier transformed, one finds exactly Eqs. (2.23), which proves Langreth theorem.

An alternative route is the one taken by Langreth [62]. For it one transforms the Keldysh contour such that it is build from two loops C_1 and C_2 , both begin and end at t_0 . To calculate $C^<(t, t')$ one chooses $t \in C_1$ and $t' \in C_2$. As a result

$$C^<(t, t') = \int_{C_1} dt_1 \mathbf{A}(t, t_1) B^<(t_1, t') + \int_{C_2} dt_1 A^<(t, t_1) \mathbf{B}(t_1, t'). \quad (2.24)$$

If, now, we make use of the definition of the retarded and advanced Green functions, Eqs. (2.16), we are able to replace the integrals over contours with an integral over real time, which leads exactly to the second of Eqs. (2.21).

2.3 Grassmann Numbers

The theoretical approach we take to calculate the partition function is based on path integrals (see Chap. 4). To treat fermionic systems within this formalism, it is necessary to introduce the notion of anti-commuting numbers, so called *Grassmann numbers*, since the fermionic creation and annihilation operators obey the anti-commutation relations given in Eqs. (2.1). The anti-commuting nature of Grassmann numbers therefore proves useful to depict this behavior. In fact, the first application of Grassmann numbers in physics was to allow the construction of fermionic path integrals. Nowadays Grassmann numbers are commonly used as a basis for superspace, onto which supersymmetry is constructed [64]. In a first step we construct the Grassmann algebra and draw some immediate consequences from it. We then continue to derive some important formulas involving Grassmann numbers and Gaussian integrals, starting with 1-dimensional integrals and finishing with the multidimensional versions.

2.3.1 Grassmann Algebra

The Grassmann (or exterior) algebra \mathcal{A} is constructed using generators ξ_i with $i = 1, \dots, N$. These generators obey the following rules [65, 66]:

1. They can be added and multiplied by complex numbers, meaning that \mathcal{A} is indeed a vector space, i.e.

$$c_0 + c_i \xi_i + c_j \xi_j \in \mathcal{A}, \text{ for } c_0, c_i, c_j \in \mathbb{C}. \quad (2.25)$$

2. The product of the generators is associative and anti-commutative. This means that

$$\xi_i \xi_j + \xi_j \xi_i = \{\xi_i, \xi_j\} = 0, \quad (2.26)$$

where $\{\cdot, \cdot\}$ denotes the anti-commutator. And for higher order products associativity means that

$$\xi_i (\xi_j \xi_k) = (\xi_i \xi_j) \xi_k = \xi_i \xi_j \xi_k. \quad (2.27)$$

From these two rules we are able to derive some basic properties of Grassmann numbers directly. Due to the anti-commutative nature of Grassmann numbers the square of a Grassmann number is zero

$$\xi^2 = 0. \quad (2.28)$$

Any function of Grassmann numbers is defined via its Taylor expansion. But the square of a Grassmann number is zero the Taylor expansion terminates after a finite number of terms. Thus, some function f of a Grassmann number ξ is given by

$$f(\xi) = \sum_{n=0}^{\infty} \frac{1}{n!} f^{(n)}|_{\xi=0} \xi^n = f(0) + \left. \frac{df}{d\xi} \right|_{\xi=0} \xi, \quad (2.29)$$

or in the case of a multidimensional function

$$f(\xi_1, \dots, \xi_k) = \sum_{n=0}^{\infty} \frac{1}{n!} \sum_{i_1 \dots i_n} \left. \frac{\partial^n f}{\partial \xi_{i_1} \dots \partial \xi_{i_n}} \right|_{\xi=0} \xi_{i_1} \dots \xi_{i_n}. \quad (2.30)$$

To make this definition of a function work, one has to define the derivative of a function of Grassmann numbers with respect to a Grassmann number. Keeping in mind that every function of Grassmann numbers can at most be linear in one specific Grassmann number it is sufficient to give the following definition:

$$\frac{\partial}{\partial \xi_i} \xi_j = \delta_{ij}. \quad (2.31)$$

Integration over functions of Grassmann numbers with respect to a Grassmann number cannot be defined in the sense of a Lebesgue integral, as is the case for real or complex functions. Instead, the definition is chosen to preserve similarities with bosonic descriptions. The integral is defined as follows [67]

$$\int d\xi 1 = 0, \text{ and } \int d\xi \xi = 1. \quad (2.32)$$

Using these definitions one is able to show that for Grassmann numbers integration and derivation are effectively identical

$$\int f(\xi) d\xi = \int (f(0) + f'(0)\xi) d\xi = f'(0) = \partial_{\xi} f(\xi). \quad (2.33)$$

2.3.2 Grassmann Gaussian Integrals

With the knowledge of the Grassmann algebra, we are now equipped to derive some useful integral identities involving Grassmann numbers. These identities are necessary when calculating the partition function via coherent state path integrals.

We start by proving the following integral identity

$$\int \prod_{i=1}^N d\bar{\xi}_i d\xi_i \exp(-\bar{\xi}^T A \xi) = \det(A), \quad (2.34)$$

with A being a $N \times N$ matrix with matrix elements $(A)_{ij} = a_{ij}$ and $\xi, \bar{\xi}$ are N dimensional vectors with Grassmann-like elements ξ_i and $\bar{\xi}_i$. We emphasize that $\bar{\xi}_i$ and ξ_i are completely independent Grassmann variables. We demonstrate the proof for case that A is a 2×2 matrix. Higher dimensional cases can be shown the same way, but the process is more tedious. The exponential function is written as its Taylor series, and then the integrals are evaluated one by one:

$$\begin{aligned} & \int d\bar{\xi}_1 d\xi_1 d\bar{\xi}_2 d\xi_2 \exp(-\bar{\xi}_1 a_{11} \xi_1 - \bar{\xi}_1 a_{12} \xi_2 - \bar{\xi}_2 a_{21} \xi_1 - \bar{\xi}_2 a_{22} \xi_2) \\ &= \int d\bar{\xi}_1 d\xi_1 d\bar{\xi}_2 d\xi_2 (1 - \bar{\xi}_1 a_{11} \xi_1)(1 - \bar{\xi}_1 a_{12} \xi_2)(1 - \bar{\xi}_2 a_{21} \xi_1)(1 - \bar{\xi}_2 a_{22} \xi_2) \\ &= \int d\bar{\xi}_1 d\xi_1 d\bar{\xi}_2 (1 - \bar{\xi}_1 a_{11} \xi_1)(1 - \bar{\xi}_2 a_{21} \xi_1) \int d\xi_2 (1 - \bar{\xi}_1 a_{12} \xi_2 - \bar{\xi}_2 a_{22} \xi_2) \\ &= \int d\bar{\xi}_1 d\xi_1 (1 - \bar{\xi}_1 a_{11} \xi_1) \int d\bar{\xi}_2 (1 - \bar{\xi}_2 a_{21} \xi_1)(\bar{\xi}_1 a_{12} + \bar{\xi}_2 a_{22}) \\ &= \int d\bar{\xi}_1 d\eta_1 (1 - \bar{\xi}_1 a_{11} \xi_1) \int d\bar{\xi}_2 (\bar{\xi}_1 a_{12} + \bar{\xi}_2 a_{22} - \bar{\xi}_2 a_{21} \xi_1 \bar{\xi}_1 a_{12}) \\ &= \int d\bar{\xi}_1 d\xi_1 (1 - \bar{\xi}_1 a_{11} \xi_1)(a_{22} - a_{21} \xi_1 \bar{\xi}_1 a_{12}) \\ &= \int d\bar{\xi}_1 d\xi_1 (a_{22} - a_{21} \xi_1 \bar{\xi}_1 a_{12} - \bar{\xi}_1 a_{11} \xi_1 a_{22}) \\ &= \int d\bar{\xi}_1 (-a_{21} \bar{\xi}_1 a_{12} + \bar{\xi}_1 a_{11} a_{22}) = a_{11} a_{22} - a_{21} a_{12} = \det(A). \end{aligned} \quad (2.35)$$

During the calculation it is important to keep in mind that signs change when pulling one Grassmann number in front of the other. With this the full calculation is straight forward and one finds the expected result. A direct consequence of Eq. (2.34) is that

$$\int \prod_{i=1}^N d\bar{\xi}_i d\xi_i \exp\left(-\sum_{i=1}^N \bar{\xi}_i \xi_i\right) = 1. \quad (2.36)$$

Apart from multidimensional Gaussian integrals, we are in need of the following identity, which we are able to prove by making use of Eq. (2.34):

$$\int \prod_{i=1}^N d\bar{\xi}_i d\xi_i e^{-\bar{\xi}^T A \xi + \bar{\eta}^T \xi + \bar{\xi}^T \eta} = \det(A) e^{\bar{\eta}^T A^{-1} \eta}, \quad (2.37)$$

where $\bar{\eta}$, η , $\bar{\xi}$ and ξ are N -dimensional Grassmann vectors and A is a complex invertible $N \times N$ matrix. We start by shifting $\bar{\xi}$ and ξ

$$\bar{\xi} \rightarrow \bar{\xi} + \bar{\eta} A^{-1}, \text{ and } \xi \rightarrow \xi + A^{-1} \eta. \quad (2.38)$$

As a consequence the integral reduces to

$$\begin{aligned} & \int \prod_{i=1}^N d\bar{\xi}_i d\xi_i e^{-\bar{\xi}^T A \xi + \bar{\eta}^T \xi + \bar{\xi}^T \eta} \\ &= e^{\bar{\eta}^T A^{-1} \eta} \int \prod_{i=1}^N d\bar{\xi}_i d\xi_i e^{-\bar{\xi}^T A \xi} \\ &= e^{\bar{\eta}^T A^{-1} \eta} \det(A), \end{aligned}$$

where in the last step we employed Eq. (2.34), leading to the desired result.

2.4 Fermionic Coherent States

Having introduced the Grassmann algebra and some basic properties, we now turn to the basis of fermionic coherent states, in which the path-integral formalism for fermionic systems is usually developed. Coherent states were first introduced as quantum mechanical analogue to a classical system. For bosonic systems coherent states are defined as the eigenstates of the annihilation operator. This definition is adopted for fermions, meaning [65, 68]

$$c_\alpha |\xi\rangle = \xi_\alpha |\xi\rangle, \quad (2.39)$$

with $|\xi\rangle$ being a coherent state and c_α annihilates a particle in state α . In the fermionic case the eigenvalues of the annihilation operator have to be anti-commuting, due to the fermionic anti-commutation relations for the creation and annihilation operators, Eq. (2.1). As a result, ξ_α is a Grassmann number. To account for these we have to define a generalized Fock space, which is constructed by the following equation

$$|\xi\rangle = \sum_{\alpha} \xi_\alpha |\phi_\alpha\rangle, \quad (2.40)$$

where $|\xi\rangle$ is a vector in the generalized Fock space, that is built from a linear combination of vectors $|\phi_\alpha\rangle$ from ordinary Fock space \mathcal{F} with Grassmann numbers as coefficients [68]. Since in Eq. (2.39) we encounter both an annihilation operator and a Grassmann number it is necessary to specify their commutation behavior. It is natural to require that [68]

$$\begin{aligned} \{c_\alpha, \xi_\beta\} &= 0 \\ \{c_\alpha^\dagger, \xi_\beta\} &= 0. \end{aligned} \quad (2.41)$$

We are now able to define a fermionic coherent state $|\xi\rangle$ as

$$|\xi\rangle = e^{-\sum_{\alpha} \xi_{\alpha} c_{\alpha}^{\dagger}} |0\rangle = \prod_{\alpha} (1 - \xi_{\alpha} c_{\alpha}^{\dagger}) |0\rangle. \quad (2.42)$$

It is easy to prove that this is indeed an eigenstate of the annihilation operator, by acting on this state with the annihilation operator c_β . The proof works as follows

$$\begin{aligned}
c_\beta \prod_{\alpha} (1 - \xi_\alpha c_\alpha^\dagger) |0\rangle &= \prod_{\alpha \neq \beta} (1 - \xi_\alpha c_\alpha^\dagger) c_\beta (1 - \xi_\beta c_\beta^\dagger) |0\rangle \\
&= \prod_{\alpha \neq \beta} (1 - \xi_\alpha c_\alpha^\dagger) \xi_\beta c_\beta c_\beta^\dagger |0\rangle = \prod_{\alpha \neq \beta} (1 - \xi_\alpha c_\alpha^\dagger) \xi_\beta (1 - c_\beta^\dagger c_\beta) |0\rangle \\
&= \prod_{\alpha \neq \beta} (1 - \xi_\alpha c_\alpha^\dagger) \xi_\beta |0\rangle = \prod_{\alpha \neq \beta} (1 - \xi_\alpha c_\alpha^\dagger) \xi_\beta (1 - \xi_\beta c_\beta^\dagger) |0\rangle \\
&= \xi_\beta \prod_{\alpha} (1 - \xi_\alpha c_\alpha^\dagger) |0\rangle. \tag{2.43}
\end{aligned}$$

Throughout this derivation we used that c_β commutes with $\xi_\alpha c_\alpha^\dagger$ for $\alpha \neq \beta$ and in the second to last step we made use of the fact that $\xi_\beta^2 = 0$. Having found the definition of a coherent state, it is now possible to derive some relations, which are going to be necessary for constructing the path integral.

At first, we note that the fermionic coherent states build an over complete basis. As a result, they are not orthogonal and the overlap between two coherent states is given by

$$\langle \xi | \xi' \rangle = e^{\sum_{\alpha} \bar{\xi}_{\alpha} \xi'_{\alpha}}. \tag{2.44}$$

To prove this we write out the two coherent states and develop them as their Taylor series

$$\begin{aligned}
\langle \xi | \xi' \rangle &= \langle 0 | \prod_{\alpha} (1 - \bar{\xi}_{\alpha} c_{\alpha}) (1 - c_{\alpha}^{\dagger} \xi'_{\alpha}) | 0 \rangle \\
&= \langle 0 | \prod_{\alpha} (1 + \bar{\xi}_{\alpha} \xi'_{\alpha} c_{\alpha} c_{\alpha}^{\dagger}) | 0 \rangle \\
&= \prod_{\alpha} (1 + \bar{\xi}_{\alpha} \xi'_{\alpha}) = e^{\sum_{\alpha} \bar{\xi}_{\alpha} \xi'_{\alpha}}, \tag{2.45}
\end{aligned}$$

which is what we wanted to show. Due to this fact one is able to build a resolution of unity via the fermionic coherent states, taking the form

$$\mathbb{1} = \int \prod_{\alpha} d\bar{\xi}_{\alpha} d\xi_{\alpha} e^{-\sum_{\alpha} \bar{\xi}_{\alpha} \xi_{\alpha}} |\xi\rangle \langle \xi|. \tag{2.46}$$

The proof for this identity is more elaborate and we refer to Ref. [69]. Finally, we introduce the trace of some operator \mathcal{O} written in fermionic coherent states. This is given by

$$\text{tr}(\mathcal{O}) = \int \prod_{\alpha} d\bar{\xi}_{\alpha} d\xi_{\alpha} e^{-\sum_{\alpha} \bar{\xi}_{\alpha} \xi_{\alpha}} \langle -\xi | \mathcal{O} | \xi \rangle. \tag{2.47}$$

To prove this we start by writing the trace in the basis of occupation numbers and

introduce a resolution of unity (see Eq. (2.46)) in the next step

$$\begin{aligned}
\text{tr}(\mathcal{O}) &= \sum_n \langle n | \mathcal{O} | n \rangle \\
&= \sum_n \int \prod_\alpha d\bar{\xi}_\alpha d\xi_\alpha e^{-\sum_\alpha \bar{\xi}_\alpha \xi_\alpha} \langle n | \mathcal{O} | \xi \rangle \langle \xi | n \rangle \\
&= \sum_n \int \prod_\alpha d\bar{\xi}_\alpha d\xi_\alpha e^{-\sum_\alpha \bar{\xi}_\alpha \xi_\alpha} \langle -\xi | n \rangle \langle n | \mathcal{O} | \xi \rangle \\
&= \int \prod_\alpha d\bar{\xi}_\alpha d\xi_\alpha e^{-\sum_\alpha \bar{\xi}_\alpha \xi_\alpha} \langle -\xi | \mathcal{O} | \xi \rangle, \tag{2.48}
\end{aligned}$$

where in the third step we switched places of the two inner products, changing the sign of one of the two states, while in the last step we used that $\sum_n |n\rangle\langle n| = \mathbf{1}$. This then leads to the desired identity for the trace.

2.5 Summary

Throughout this chapter we laid out the mathematical framework to treat fermionic systems out of equilibrium. We introduced the Keldysh contour, a closed time contour that allows the treatment of nonequilibrium systems at the cost of doubling the degrees of freedom. We applied this Keldysh contour to the notion of Green functions, which transforms a Green function in the traditional sense into a 2×2 matrix in Keldysh space. Identifying the elements of this matrix, led us to several useful identities, which allow for an easier evaluation of these four Green functions. To develop a path-integral formalism for fermionic systems the notion of anti-commuting numbers, so called Grassmann numbers, was introduced. We explained their algebra and defined their derivative and integral. The latter allowed us to derive several integral identities for the path-integral formalism. Finally, a generalized Fock space was adopted to include fermionic coherent states, which are eigenvalues of the annihilation operator with the respective eigenvalues being Grassmann numbers. This is the basis in which the path-integral formalism is developed and therefore we, again, derived several useful identities, that find frequent use in Chap. 4.

3 Quantum-Dot Spin Valve

We now turn our focus to the system that is discussed throughout this work, the quantum-dot spin valve. It is a quantum dot, that is tunnel coupled to two ferromagnetic leads and capacitively contacted via a gate electrode. The interplay between the spin dynamics, caused by the ferromagnetic leads, the Coulomb interactions between the electrons confined to the small quantum dot and nonequilibrium make it a fascinating system to study. We already introduced the TMR, Kondo effect and exchange field effect in Chap. 1, which all can be studied within the quantum-dot spin valve. We start by giving an overview of current treatments of the quantum-dot spin valve.

On an experimental level, quantum-dot spin valves are discussed extensively with several effects having been under investigation. It is possible to control spin transport, and with it the TMR, via a gate voltage, which has been shown for an InAs quantum dot coupled to Ni electrodes [50], as well as for a carbon-nanotube quantum-dot setup [46, 47]. For both systems it has been shown that an external magnetic field can compensate the exchange field, thus effectively enabling a measurement of it [14]. The Kondo effect has been measured for both an InAs and a carbon-nanotube quantum-dot setup [14, 49]. Additionally, measurements of the Kondo effect have been carried out for a C₆₀ molecule coupled to Ni electrodes [28]. Again, for a setup including a carbon nanotube as quantum dot the precession of an on-site spin can be harnessed and tuned via a gate voltage [13] and the magnetoresistance shows a strong hysteretic behavior for temperatures lower than 30 K [70].

From a theoretician's point of view, the quantum-dot spin valve has gathered a lot of attention, too. Coulomb interactions prohibit a diagonalization of the underlying many-body Hamiltonian and controlled physical approximations are needed to investigate the emerging physical phenomena. Different approximation strategies are possible to tackle the interacting, spin-dependent problem. The most prominent of these methods are discussed in short in Sec. 3.3. Here, we give a short overview of the current state of research regarding the quantum-dot spin valve. Using the Hartree-Fock method, i.e. approximating electron-electron interactions, the TMR and the accumulated spin were examined for a noncollinear setup of the quantum-dot spin valve [71]. Using a hierarchical quantum master equation approach in the high temperature limit, it was discussed that exchange interactions quenching a strong current suppression causes several peaks in the conductance [44]. Within a weak-tunneling approximation in a wide range of bias and gate voltages, characteristics of the exchange field have been discussed [26, 27]. A multi-level metallic island coupled to ferromagnetic leads has been treated on the same footing [72, 73].

Additionally, it has been shown that the exchange field can be probed via a third, superconducting lead [74], or via a spin resonance, that appears when the exchange field is perpendicular to one of the leads polarizations [75]. The coherent dynamics of a quantum-dot spin valve have been shown to be distillable from full counting statistics [76]. It was also shown recently, that the magnetizations of the attached leads may be switched by tuning gate voltages [77].

We demonstrate in Chap. 6 that higher order effects have a strong influence on the TMR. Consequently, numerically exact methods that include all orders of the tunnel coupling and the Coulomb interaction are in high demand for a complete picture of the electronic transport through quantum-dot spin valves. There are several methods accounting for resonant tunneling that have been applied to the quantum-dot spin valve. For the regime of linear response numerical renormalization group (NRG) approaches work well revealing the temperature dependence of the TMR [78], as well as allowing a discussion of the Kondo problem, including the influence of the ferromagnet's band structure [79, 80]. In addition, the Kondo problem for a quantum-dot spin valve was tackled via an equations-of-motion method [81] as well as via a poor man's scaling approach combined with slave-boson mean field theory [82]. Using density matrix renormalization group (DMRG) theory, the local density of states as well as the TMR have been calculated [83]. For the sake of completeness, we note that quantum-dot systems coupled to normal metal leads are also studied by means of quantum Monte Carlo simulations [84], allowing e.g. the study of the time-dependent current through these systems, as well as the Green functions and occupation number [85]. The short-to-intermediate time limit for e.g. the tunneling current, could also be obtained by means of a generalized iterative influence functional [86].

Throughout this work we make use of the ISPI technique, that is introduced and expanded upon in Chap. 5. This method was already successfully used to describe electric transport through an Anderson dot, that is coupled to two normal leads [87, 88], and to the Anderson-Holstein model [89], where the quantum dot has an intrinsic bosonic mode. In addition, it was applied to a magnetic, interacting quantum dot [90]. For this, the Anderson model was expanded by adding a magnetic impurity that is localized on the quantum dot and interacts via an exchange interaction with the localized spins of the electrons on the quantum dot. We apply the ISPI technique to the quantum-dot spin valve and expand the formalism to allow for spin-dependent transport. Additionally, we introduce the dot's occupation number and its spin projection as possible observables within this approach.

In this chapter, we introduce the Hamiltonian for the quantum-dot spin valve, and describe each of its parts in detail. We give an analytical derivation of the tunneling current as well as the occupation number and spin projections for the case of a noninteracting setup. Finally, we give an overview of prominent theoretical approaches to the problem of treating the interacting quantum-dot spin valve, allowing a classification of the ISPI scheme, that is used for this thesis.

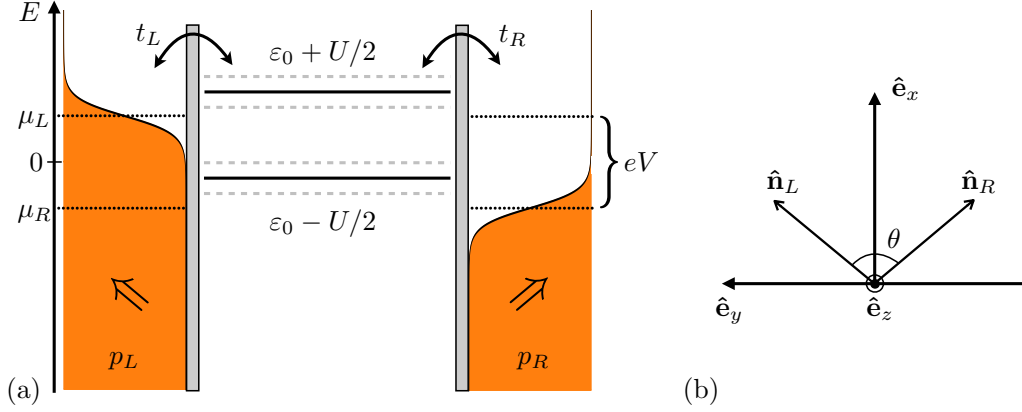


Figure 3.1: Panel (a) shows a sketch of the quantum-dot spin valve at some finite temperature $k_B T$, the orange parts on the left- and right-hand side represent the leads at different chemical potentials $\mu_{L/R}$, given by the bias voltage eV . The double arrows in the leads denote the magnetization axes $\hat{\mathbf{n}}_{L/R}$. The central part denotes the single-level quantum dot, with the two solid lines describing the energy levels for single (lower) and double (upper) occupation, while the dashed grey lines show the impact of a magnetic field. The grey bars between the dot and the leads represent tunneling barriers. (b) The common coordinate system for the setup used throughout this work. The choice is based on the the leads' magnetization axes.

3.1 Model

A theoretical description of electronic transport through quantum-dot systems is usually based on an adaptation of the Anderson impurity model, which was originally introduced by Anderson in 1961 to describe magnetic impurities embedded in metals [91]. We adapt the Anderson impurity model too by coupling a single-level quantum dot to two ferromagnetic leads. Each of the leads is magnetized in an arbitrary direction and is spin-polarized, leading to spin-dependent tunneling in and out of the quantum dot. A systematic sketch of the system is given in Fig. 3.1. The Hamiltonian for the quantum-dot spin valve is consequently given by

$$\mathcal{H} = \sum_{\alpha} \mathcal{H}_{\alpha} + \mathcal{H}_{\text{dot}} + \sum_{\alpha} \mathcal{H}_{\text{T},\alpha}, \quad (3.1)$$

where $\alpha = L, R$ labels the left- and right-hand lead. Going from left to right we inspect each term contributing to the Hamiltonian and describe it in detail.

Leads: The first part of Eq. (3.1) describes the two ferromagnetic leads, which are both modeled by a noninteracting, three-dimensional electron gas. Each lead is magnetized along some axis $\hat{\mathbf{n}}_{\alpha}$, with the two axes enclosing the angle θ . We choose

to quantize each lead along its magnetization axis. The ferromagnetic leads are approximated by the *Stoner model*, meaning one assumes a strong spin asymmetry in the density of states for majority (+) and minority (−) spins. Majority and minority spins are distinguished based on the spin type with larger density of states at the Fermi energy. The Hamiltonian for the leads then takes the form

$$\mathcal{H}_\alpha = \sum_{\mathbf{k}\tau} (\varepsilon_{\mathbf{k}\tau} - \mu_\alpha) c_{\alpha\mathbf{k}\tau}^\dagger c_{\alpha\mathbf{k}\tau}, \quad (3.2)$$

where $\tau = \pm$ differentiate majority and minority spin state of the electrons, and \mathbf{k} is the electron momentum. The operators $c_{\alpha\mathbf{k}\tau}^\dagger$ and $c_{\alpha\mathbf{k}\tau}$ create or annihilate a particle in lead α , with momentum \mathbf{k} and in spin state τ , respectively. $\varepsilon_{\mathbf{k}\tau}$ denotes the single particle energy and $\mu_{L/R} = \pm eV/2$ is the chemical potential, which is credited to the bias voltage V applied between left and right lead. e is the electron charge.

The density of states of lead α is given by $\rho(\varepsilon_{\alpha\mathbf{k}\tau}) = \sum_{\mathbf{k}} \delta(\omega - \varepsilon_{\alpha\mathbf{k}\tau})$. Throughout this work we work in the wide-band limit, meaning that we assume the density of states to be constant in energy $\rho(\varepsilon_{\alpha\mathbf{k}\tau}) \approx \rho(\varepsilon_{\alpha\mathbf{k}\tau}^F)$. This is justified since transport properties are usually dominated by states close to the Fermi energy. Of course, this approximation affects details of our results but the general physical picture is not affected. This is especially true, when the stationary limit is under investigation [92]. Additionally, including a real, energy-dependent density of states is possible within the path-integral formalism, but would make calculations more complicated and usually prohibit an analytical evaluation. The asymmetry between the majority and the minority density of state in lead α is characterized by the degree of spin polarization, given by

$$p_\alpha = \frac{\rho(\varepsilon_{\alpha\mathbf{k}+}^F) - \rho(\varepsilon_{\alpha\mathbf{k}-}^F)}{\rho(\varepsilon_{\alpha\mathbf{k}+}^F) + \rho(\varepsilon_{\alpha\mathbf{k}-}^F)}, \quad (3.3)$$

where $p_\alpha = 0$ describes a nonmagnetic lead, while $p_\alpha = 1$ represents a half metallic electrode with majority spins only.

The magnetization axes of the two leads $\hat{\mathbf{n}}_\alpha$ help us define a common coordinate system for our setup. We choose the x -axis such that it splits the angle θ in half. The y -axis resides in the same plane as the two magnetization axes and the x -axis, and the z -axis is then perpendicular on both x - and y -axis. The unit vectors are given by

$$\begin{aligned} \hat{\mathbf{e}}_x &= \frac{\hat{\mathbf{n}}_L + \hat{\mathbf{n}}_R}{|\hat{\mathbf{n}}_L + \hat{\mathbf{n}}_R|}, \\ \hat{\mathbf{e}}_y &= \frac{\hat{\mathbf{n}}_L - \hat{\mathbf{n}}_R}{|\hat{\mathbf{n}}_L - \hat{\mathbf{n}}_R|}, \\ \hat{\mathbf{e}}_z &= \hat{\mathbf{e}}_x \times \hat{\mathbf{e}}_y. \end{aligned} \quad (3.4)$$

In Fig. 3.1 (b) the coordinate system is depicted based on the magnetization axes from panel (a). The z -axis points out of the plane. Other conventions are of course possible and actively used, however, with our choice the angles $\theta_L = -\theta_R = \theta/2$ are always symmetric, which simplifies some formulas.

For future convenience it is useful to introduce a spinor notation with the spinors $\mathcal{C}_{\alpha\mathbf{k}} = (c_{\alpha\mathbf{k}+}, c_{\alpha\mathbf{k}-})^T$ and $\mathcal{C}_{\alpha\mathbf{k}}^\dagger = (c_{\alpha\mathbf{k}+}^\dagger, c_{\alpha\mathbf{k}-}^\dagger)$. Using this the Hamiltonian for lead α looks like

$$\mathcal{H}_\alpha = \sum_{\mathbf{k}} \mathcal{C}_{\alpha\mathbf{k}}^\dagger \mathcal{E}_{\alpha\mathbf{k}} \mathcal{C}_{\alpha\mathbf{k}}, \quad (3.5)$$

where we defined the matrix $\mathcal{E}_{\alpha\mathbf{k}} = \begin{pmatrix} \varepsilon_{\mathbf{k}+} - \mu_\alpha & 0 \\ 0 & \varepsilon_{\mathbf{k}-} - \mu_\alpha \end{pmatrix}$. We frequently use the short hand $\varepsilon_{\alpha\mathbf{k}\tau} = \varepsilon_{\mathbf{k}\tau} - \mu_\alpha$ to keep formulas compact.

Quantum Dot: The quantum dot is described by a single, interacting energy level E_0 , which can be tuned via a gate voltage. We choose to quantize the level along the z -axis of the coordinate system defined above, Eq. (3.4). The Hamiltonian is then given by

$$\mathcal{H}_{\text{dot}} = \sum_{\sigma} E_0 d_{\sigma}^\dagger d_{\sigma} + U d_{\uparrow}^\dagger d_{\downarrow}^\dagger d_{\downarrow} d_{\uparrow}, \quad (3.6)$$

where $\sigma = \uparrow, \downarrow$ denote the projection of the quantum-dot's spin along the quantization axis. d_{σ}^\dagger and d_{σ} create and annihilate an electron on the quantum dot with spin σ , respectively. For convenience in further calculations we make use of the operator identity

$$d_{\uparrow}^\dagger d_{\downarrow}^\dagger d_{\downarrow} d_{\uparrow} = \frac{1}{2} \left(d_{\uparrow}^\dagger d_{\uparrow} + d_{\downarrow}^\dagger d_{\downarrow} - \left(d_{\uparrow}^\dagger d_{\uparrow} - d_{\downarrow}^\dagger d_{\downarrow} \right)^2 \right), \quad (3.7)$$

which follows directly from the anti-commutation relations for the creation and annihilation operators, Eq. (2.1). The bilinear part of the interaction is then absorbed into the single-particle energy, leading us to define $\varepsilon_0 = E_0 + U/2$. In addition, we again introduce the spinor notation, such that \mathcal{D}^\dagger and \mathcal{D} are defined similarly to their lead counterparts. The resulting Hamiltonian is then

$$\mathcal{H}_{\text{dot}} = \mathcal{D}^\dagger \varepsilon_0 \sigma_0 \mathcal{D} - \frac{U}{2} (\mathcal{D}^\dagger \sigma_z \mathcal{D})^2, \quad (3.8)$$

where we made use of the Pauli matrix σ_z and $\sigma_0 = \mathbb{1}_2$ is a 2×2 identity matrix. Finally, we are also interested in the effects of a magnetic field acting on the quantum dot in an arbitrary direction. We include this in the Hamiltonian via an additional term

$$\mathcal{H}_{\text{dot}} = \mathcal{D}^\dagger (\varepsilon_0 \sigma_0 + \mathbf{B} \cdot \mathbf{S}) \mathcal{D} - \frac{U}{2} (\mathcal{D}^\dagger \sigma_z \mathcal{D})^2, \quad (3.9)$$

where $\mathbf{S} = \frac{1}{2}(\sigma_x, \sigma_y, \sigma_z)^T$ and \mathbf{B} is the local magnetic field, which is understood to be in units of $g\mu_B$. Here, g is the Landé factor for electrons and μ_B is the Bohr magneton.

Tunneling: Finally, the tunneling between the dot and the leads is described by the Hamiltonian

$$\mathcal{H}_{T,\alpha} = \sum_{\mathbf{k}} \mathcal{C}_{\alpha\mathbf{k}}^\dagger Y_{\alpha} \mathcal{D} + \text{H.c.} \quad (3.10)$$

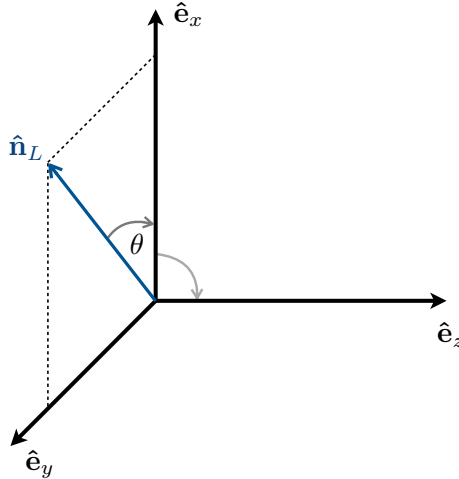


Figure 3.2: Rotation of the quantization axis.

Y_α includes the tunnel coupling t_α as well as a passive rotation from the dot's spin coordinate system to that of the respective lead. This is necessary since the two leads and the dot are in general all quantized in different directions. We therefore require a $SU(2)$ rotation between each lead and the dot. Due to our choice of the coordinate system the difference between left- and right-hand side is a mere change in sign of the angle. It is useful to split the rotation in two successive rotations, one rotating the magnetization axis in z -direction such that it is parallel to the x -axis afterwards and a second rotating it in y -direction such that it points along the z -axis in the end. In general $SU(2)$ rotations are given by

$$\mathfrak{R} = \exp\left(-\frac{i}{2}\boldsymbol{\theta} \cdot \boldsymbol{\sigma}\right), \quad (3.11)$$

where $\boldsymbol{\theta}$ is the vector including the angles, while $\boldsymbol{\sigma} = (\sigma_x, \sigma_y, \sigma_z)^T$. With this it is straight forward to give the form of Y_α

$$Y_\alpha = t_\alpha \exp\left(\frac{i\pi}{4}\sigma_y\right) \exp\left(\alpha\frac{i\theta}{4}\sigma_z\right) = \frac{t_\alpha}{\sqrt{2}} \begin{pmatrix} e^{i\alpha\theta/4} & e^{-i\alpha\theta/4} \\ -e^{i\alpha\theta/4} & e^{-i\alpha\theta/4} \end{pmatrix}. \quad (3.12)$$

We emphasize that we have chosen t_α and with it Y_α energy independent.

3.2 Noninteracting Limit

Throughout this work we study the current through the quantum-dot spin valve, as well as the occupation number and the three components of accumulated spin on the quantum dot using the ISPI technique. All these quantities are investigated in the stationary limit, where the dot was coupled to the leads and the bias voltage and the Coulomb interactions have reached their current value a long time ago. This

means, that we do not explore the effects of a time dependent bias or gate voltage nor of a time dependent tunnel coupling in this work.

As a benchmark for the ISPI method we often refer to the case of vanishing Coulomb interaction, which can be solved analytically. Hence, we derive the current as well as the four local observables, occupation number and components of the spin projection of the dot, using an equations-of-motion ansatz for $U = 0$. These derivations can be found in e.g. Ref. [33] for the Anderson model as well as in Ref. [57] for a multilevel quantum dot. The current for the Anderson model is given by the well-known Meir-Wingreen formula (see Ref. [61]), which means we derive a version of this formula that describes the current through the quantum-dot spin valve. Since these derivations are significantly easier without the spinor notation, that we introduced for the creation/annihilation operators in the Hamiltonian, we do not use this notation here.

3.2.1 Current

We can measure the current either on the left- or on the right-hand side of the quantum dot. Both have to be equal since our setup conserves charge. Throughout this work we discuss the symmetrized current $\mathcal{I} = \frac{\mathcal{I}_L + \mathcal{I}_R}{2}$. In general the operator of the current on side α is defined as

$$\mathcal{I}_\alpha = -e\dot{\mathcal{N}}_\alpha = -ie[\mathcal{H}, \mathcal{N}_\alpha], \quad (3.13)$$

where $\mathcal{N}_\alpha = \sum_{\mathbf{k}\tau} c_{\alpha\mathbf{k}\tau}^\dagger c_{\alpha\mathbf{k}\tau}$ is the occupation number operator of lead α . Since \mathcal{N}_α commutes with both, the dot and lead Hamiltonian, only the commutator with the tunneling Hamiltonian yields a nonzero contribution. Making use of the anti-commutation relations of the creation and annihilation operators it is straight forward to find

$$\mathcal{I}_\alpha = ie \sum_{\mathbf{k}\tau\sigma} Y_{\alpha,\tau\sigma} c_{\alpha\mathbf{k}\tau}^\dagger d_\sigma - Y_{\alpha,\sigma\tau}^* d_\sigma^\dagger c_{\alpha\mathbf{k}\tau}. \quad (3.14)$$

We are interested in the expectation value of this operator. Since $Y_{\alpha,\tau\sigma}$ and $Y_{\alpha,\sigma\tau}^*$ are only prefactors, they can be pulled from the expectation values, which then only contain creation and annihilation operators.

$$\langle \mathcal{I}_\alpha \rangle = I_\alpha = ie \sum_{\mathbf{k}\tau\sigma} Y_{\alpha,\tau\sigma} \langle c_{\alpha\mathbf{k}\tau}^\dagger d_\sigma \rangle - Y_{\alpha,\sigma\tau}^* \langle d_\sigma^\dagger c_{\alpha\mathbf{k}\tau} \rangle. \quad (3.15)$$

These expectation values have the form of lesser Green functions, which motivates us to define *mixed lesser Green functions*, given by

$$\begin{aligned} G_{\sigma,\alpha\mathbf{k}\tau}^<(t, t') &= i \langle c_{\alpha\mathbf{k}\tau}^\dagger(t') d_\sigma(t) \rangle \\ G_{\alpha\mathbf{k}\tau,\sigma}^<(t, t') &= i \langle d_\sigma^\dagger(t') c_{\alpha\mathbf{k}\tau}(t) \rangle, \end{aligned} \quad (3.16)$$

where we note that at equal times they fulfill $G_{\sigma,\alpha\mathbf{k}\tau}^<(t,t) = -[G_{\alpha\mathbf{k}\tau,\sigma}^<(t,t)]^*$. With this the current takes the form

$$\begin{aligned} I_\alpha &= 2e \operatorname{Re} \left(\sum_{\mathbf{k}\tau\sigma} Y_{\alpha\tau,\sigma} G_{\sigma,\alpha\mathbf{k}\tau}^<(t,t) \right) \\ &= 2e \operatorname{Re} \left(\sum_{\mathbf{k}\tau\sigma} Y_{\alpha\tau,\sigma} \int \frac{d\omega}{2\pi} G_{\sigma,\alpha\mathbf{k}\tau}^<(\omega) \right), \end{aligned} \quad (3.17)$$

where in the second step we took advantage of the fact that the mixed lesser Green function is invariant under time translations. Therefore, we are able to write it as $G_{\sigma,\alpha\mathbf{k}\tau}^<(t,t) = G_{\sigma,\alpha\mathbf{k}\tau}^<(0,0) = \int \frac{d\omega}{2\pi} G_{\sigma,\alpha\mathbf{k}\tau}^<(\omega)$.

We have to acknowledge that the system is in nonequilibrium and that the lesser Green function is only one of four elements of the full nonequilibrium Green function. For convenience we make use of the basis defined in Eq. (2.19). Using an infinite-order perturbation expansion, we are able to derive an expression for the nonequilibrium mixed Green function (cf. App. A) given by

$$\mathbf{G}_{\sigma,\alpha\mathbf{k}\tau}(\omega) = \sum_{\sigma'\tau'} \mathbf{G}_{\sigma\sigma'}(\omega) Y_{\alpha,\sigma'\tau'}^* \mathbf{g}_{\alpha\mathbf{k},\tau'\tau}(\omega). \quad (3.18)$$

Here $\mathbf{G}_{\sigma\sigma'}$ is the dressed dot Green function in presence of the leads, while $\mathbf{g}_{\alpha\mathbf{k},\tau\tau'}$ is the free Green function of lead α . We emphasize that bold letters again denote a 2×2 matrix in Keldysh space. With this formula we are now able to employ Langreth theorem, Eq. (2.21), to find an expression for the lesser Green function

$$G_{\sigma,\alpha\mathbf{k}\tau}^<(\omega) = \sum_{\sigma'\tau'} Y_{\alpha,\sigma'\tau'}^* [G_{\sigma\sigma'}^<(\omega) g_{\alpha\mathbf{k},\tau'\tau}^A(\omega) + G_{\sigma\sigma'}^R(\omega) g_{\alpha\mathbf{k},\tau'\tau}^<(\omega)]. \quad (3.19)$$

The elements of the free lead Green function are well-known and take the form

$$\begin{aligned} g_{\alpha\mathbf{k},\tau\tau'}^{R/A}(\omega) &= \lim_{\eta \rightarrow 0^+} \frac{\delta_{\tau\tau'}}{\omega - \varepsilon_{\alpha\mathbf{k}\tau} \pm i\eta} \\ g_{\alpha\mathbf{k},\tau\tau'}^<(\omega) &= i2\pi \delta_{\tau\tau'} \delta(\omega - \varepsilon_{\alpha\mathbf{k}\tau}) f_\alpha(\varepsilon_{\alpha\mathbf{k}\tau}), \end{aligned} \quad (3.20)$$

where $f_\alpha(x) = f(x - \mu_\alpha)$, and $f(x) = (1 + e^{\beta x})^{-1}$ is the Fermi-Dirac function and $\beta = \frac{1}{k_B T}$ is the inverse temperature. Plugging Eqs. (3.19) and (3.20) in the current formula, and cancelling the sum over τ' via the Kronecker-Delta $\delta_{\tau\tau'}$, one finds

$$\begin{aligned} I_\alpha &= 2e \operatorname{Re} \left[\int \frac{d\omega}{2\pi} \sum_{\mathbf{k}\sigma\tau\sigma'} Y_{\alpha,\tau\sigma} Y_{\alpha,\sigma'\tau}^* \left(\lim_{\eta \rightarrow 0^+} \frac{G_{\sigma\sigma'}^<(\omega)}{\omega - \varepsilon_{\alpha\mathbf{k}\tau} - i\eta} \right. \right. \\ &\quad \left. \left. + i2\pi G_{\sigma\sigma'}^R(\omega) \delta(\omega - \varepsilon_{\alpha\mathbf{k}\tau}) f_\alpha(\varepsilon_{\alpha\mathbf{k}\tau}) \right) \right]. \end{aligned} \quad (3.21)$$

To perform the sum over \mathbf{k} we transform it into an integral over energy $\sum_{\mathbf{k}} \rightarrow \int d\varepsilon_{\alpha\tau} \rho(\varepsilon_{\alpha\tau})$ and make use of the wide-band limit $\rho(\varepsilon_{\alpha\tau}) \approx \rho(\varepsilon_{\alpha\tau}^F)$, as discussed in

Sec. 3.1. Thanks to this approximation, we are able to continue to work analytically. For the second addend of the current formula the delta-function cancels the integral over $\varepsilon_{\alpha\tau}$, while in the first addend we make use of the identity [59]

$$\int d\varepsilon_{\alpha\tau} \lim_{\eta \rightarrow 0^+} \frac{1}{\omega - \varepsilon_{\alpha\tau} - i\eta} = \int d\varepsilon_{\alpha\tau} \left(\frac{\mathcal{P}}{\omega - \varepsilon_{\alpha\tau}} + i\pi\delta(\omega - \varepsilon_{\alpha\tau}) \right) = i\pi. \quad (3.22)$$

The principle value $\mathcal{P} \frac{1}{\omega - \varepsilon_{\alpha\tau}}$ vanishes since the integral runs symmetrically from $-\infty$ to ∞ . Therefore, the current takes the following form

$$I_\alpha = -2e \operatorname{Im} \left[\int \frac{d\omega}{2\pi} \sum_{\sigma\tau\sigma'} Y_{\alpha,\tau\sigma} Y_{\alpha,\sigma'\tau}^* \rho(\varepsilon_{\alpha\tau}^F) (\pi G_{\sigma\sigma'}^<(\omega) + 2\pi G_{\sigma\sigma'}^R(\omega) f_\alpha(\omega)) \right]. \quad (3.23)$$

In a final step we combine $2\pi \sum_\tau Y_{\alpha,\sigma'\tau}^* \rho(\varepsilon_{\alpha\tau}^F) Y_{\alpha,\tau\sigma}$ in one matrix

$$\begin{aligned} \hat{\Gamma}_\alpha &= \frac{1}{2} \begin{pmatrix} \Gamma_{\alpha+} + \Gamma_{\alpha-} & e^{-i\alpha\theta/2} p_\alpha (\Gamma_{\alpha+} + \Gamma_{\alpha-}) \\ e^{i\alpha\theta/2} p_\alpha (\Gamma_{\alpha+} + \Gamma_{\alpha-}) & \Gamma_{\alpha+} + \Gamma_{\alpha-} \end{pmatrix} \\ &= \begin{pmatrix} \Gamma_\alpha & e^{-i\alpha\theta/2} p_\alpha \Gamma_\alpha \\ e^{i\alpha\theta/2} p_\alpha \Gamma_\alpha & \Gamma_\alpha \end{pmatrix}. \end{aligned} \quad (3.24)$$

where, for the sake of clarity, we denote a 2×2 matrix in spin space with a hat throughout this section. Here we introduced the spin dependent hybridization of the dot by lead α , due to the tunneling amplitude t_α , given by $\Gamma_{\alpha\tau} = 2\pi |t_\alpha|^2 \rho(\varepsilon_{\alpha\tau}^F)$. At this point we also define that $\Gamma_\alpha = \sum_\tau \Gamma_{\alpha\tau}/2$. This should not be confused with the matrix $\hat{\Gamma}_\alpha$. Therefore, as a final result for the expectation value of the current operator we find

$$I_\alpha = -2e \int \frac{d\omega}{2\pi} \operatorname{Im} \left[\operatorname{tr} \left(\frac{1}{2} \hat{\Gamma}_\alpha \hat{G}^<(\omega) + \hat{\Gamma}_\alpha \hat{G}^R(\omega) f_\alpha(\omega) \right) \right]. \quad (3.25)$$

Having derived an analogue to the Meir-Wingreen formula for the quantum-dot spin valve, we are left with finding expressions for dressed retarded and lesser Green functions. The dressed nonequilibrium Green function obeys the Dyson equation, given by (see App. A)

$$\hat{\mathbf{G}}(\omega) = \hat{\mathbf{G}}_0(\omega) + \hat{\mathbf{G}}_0(\omega) \hat{\mathbf{\Sigma}}(\omega) \hat{\mathbf{G}}(\omega), \quad (3.26)$$

with $\hat{\mathbf{G}}_0$ being the free dot Green function and $\hat{\mathbf{\Sigma}}$ the self energy. Both are 4×4 matrices. The Dyson equation is solved via

$$\hat{\mathbf{G}}(\omega) = \left(\hat{\mathbf{G}}_0^{-1}(\omega) - \hat{\mathbf{\Sigma}}(\omega) \right)^{-1}. \quad (3.27)$$

The free dot Green function can be chosen diagonal in Keldysh space, and consequently takes the form

$$\hat{\mathbf{G}}_0(\omega) = \begin{pmatrix} [(\omega - \varepsilon_0)\sigma_0 - \mathbf{B} \cdot \mathbf{S} + i0^+]^{-1} & 0 \\ 0 & [(\omega - \varepsilon_0)\sigma_0 - \mathbf{B} \cdot \mathbf{S} - i0^+]^{-1} \end{pmatrix}. \quad (3.28)$$

From the Dyson equation, Eq. (3.26), and Langreth theorem, Eq. (2.23), it follows immediately that a similar Dyson equation is valid for the retarded and advanced Green functions

$$\hat{G}^{A/R}(\omega) = \hat{G}_0^{A/R} + \hat{G}_0^{A/R}(\omega)\hat{\Sigma}^{A/R}(\omega)\hat{G}^{A/R}(\omega), \quad (3.29)$$

while the lesser Green function obeys the *Keldysh theorem*

$$\hat{G}^<(\omega) = \hat{G}^R(\omega)\hat{\Sigma}^<(\omega)\hat{G}^A(\omega). \quad (3.30)$$

The self energies are defined as $\hat{\Sigma}^{A/R/<}(\omega) = \sum_{\alpha\mathbf{k}} Y_{\alpha}^{\dagger}\hat{g}_{\alpha\mathbf{k}}^{A/R/<}Y_{\alpha}$. Using the same simplifications as before one finds that

$$\begin{aligned} \hat{\Sigma}^{A/R} &= \pm \frac{i}{2} \sum_{\alpha} \begin{pmatrix} \Gamma_{\alpha} & e^{-i\alpha\theta/2}p_{\alpha}\Gamma_{\alpha} \\ e^{i\alpha\theta/2}p_{\alpha}\Gamma_{\alpha} & \Gamma_{\alpha} \end{pmatrix} = \pm \frac{i}{2} \sum_{\alpha} \hat{\Gamma}_{\alpha} \\ \hat{\Sigma}^< &= \sum_{\alpha} if_{\alpha}(\omega) \begin{pmatrix} \Gamma_{\alpha} & e^{-i\alpha\theta/2}p_{\alpha}\Gamma_{\alpha} \\ e^{i\alpha\theta/2}p_{\alpha}\Gamma_{\alpha} & \Gamma_{\alpha} \end{pmatrix} = \sum_{\alpha} if_{\alpha}(\omega)\hat{\Gamma}_{\alpha}. \end{aligned} \quad (3.31)$$

With this, all elements of Eq. (3.25) are known, allowing us to analytically calculate the current through a noninteracting quantum-dot spin valve. We rely heavily on this result, as an efficient way to calculate noninteracting results and as a benchmark to compare the noninteracting results from the more sophisticated methods, we introduce in Chapter 5.

3.2.2 Occupation Number and Spin Components

Having derived an expression of the current, finding analytical expressions for the occupation number and components of accumulated spin is straightforward. The operators for these observables are given by

$$\begin{aligned} \mathcal{N}_0 &= d_{\uparrow}^{\dagger}d_{\uparrow} + d_{\downarrow}^{\dagger}d_{\downarrow} \\ \mathcal{S}_x &= \frac{1}{2} \left(d_{\uparrow}^{\dagger}d_{\downarrow} + d_{\downarrow}^{\dagger}d_{\uparrow} \right) \\ \mathcal{S}_y &= \frac{i}{2} \left(d_{\uparrow}^{\dagger}d_{\downarrow} - d_{\downarrow}^{\dagger}d_{\uparrow} \right) \\ \mathcal{S}_z &= \frac{1}{2} \left(d_{\uparrow}^{\dagger}d_{\uparrow} - d_{\downarrow}^{\dagger}d_{\downarrow} \right). \end{aligned} \quad (3.32)$$

The expectation values of these operators can be easily identified as elements of the dressed lesser Green function of the quantum dot (see the definition of the nonequilibrium Green function, Eq. (2.10)). We, therefore are able to apply similar arguments as in the derivation of the noninteracting current. This leads us to

$$\begin{aligned} \langle \mathcal{N}_0 \rangle &= \int \frac{d\omega}{2\pi} \text{Im tr} \left(\hat{G}^<(\omega) \right) \\ \langle \mathcal{S}_j \rangle &= \int \frac{d\omega}{2\pi} \text{Im tr} \left(\hat{G}^<(\omega) \mathbf{S}_j \right), \quad j = x, y, z. \end{aligned} \quad (3.33)$$

The dressed lesser Green function is already known from the derivation of the current expectation value, while \mathbf{S} was introduced in Eq. (3.9) when discussing the form of the quantum-dot Hamiltonian. With this all parts of the expectation values are known and Eq. (3.33) is the analytical solution of the expectation values for occupation number and spin components.

3.3 Theoretical Approaches

The combination of nonequilibrium via the tunnel-coupled leads and the on-site Coulomb interactions prove to be difficult in a theoretical description of the quantum-dot spin valve. We have just derived an analytical solution for the noninteracting limit, $U = 0$. Alternatively, it would be possible to find an analytical solution for finite U , but without a hybridization from the leads. Both cases are, however, insufficient for a substantial description of the electronic transport through the quantum-dot spin valve.

To incorporate the Coulomb interaction and a finite hybridization strength Γ into a theoretical model, one has to introduce controlled approximations. This work is based on the ISPI technique, which allows us to study resonant effects of electronic transport through quantum-dot systems [87, 88, 93]. In Chap. 5 we discuss this method extensively and advance it to a transfer-matrix approach, and therefore refer to this chapter for in-depth information on the method. The ISPI approach is not limited to scenarios with a clear separation of energy scales and instead excels in the study of the stationary limit for the generic case where all energy scales are of the same order of magnitude. In this regime resonant tunneling leads to a finite peak broadening and accounting for Coulomb interactions is crucial for a quantitative discussion of electronic transport through the setup. This regime is experimentally relevant, especially for setups including larger quantum dots with small to intermediate Coulomb interaction strengths [13]. The peak broadening as well as interaction-induced effects are both well resolved within the ISPI scheme. This technique is therefore a useful tool, providing numerically exact data when discussing quantum-dot spin valves in the mixed-valence regime. We emphasize that, even though we focus on the stationary limit in this work, time-dependent problems are not out of the scope of the ISPI method. We note that there is a similar iterative approach to calculate density matrix elements, developed independently of the ISPI approach [94]. There are, of course, other ways to tackle the problem. To allow a classification of the ISPI technique, we introduce some prominent methods and explain which approximations are usually made, and in which parameter range they are applicable.

In Sec. 3.2 we introduced a solution for the noninteracting quantum-dot spin valve in nonequilibrium. If the electrons on the quantum-dot are only weakly interacting, it is possible to understand the noninteracting solution as the zeroth order of a *perturbation series in the Coulomb interaction U* [68, 95]. The self energies and Green functions of the noninteracting solution are then modified to include e.g. first

or first and second order processes in the Coulomb interaction, while higher order contributions are neglected. This approach is a more controlled approximation in the interaction strength as *mean-field theory* can provide. For mean-field theory the basic assumption is that the deviations of an operator from its expectation value are small. Applying this approximation and Wick's theorem to the interaction Hamiltonian, leads to the mean-field interaction Hamiltonian, with which the theory can be solved in a straight-forward manner [33, 96]. However, since the methods are limited to small Coulomb interactions, many important features cannot be studied using these methods, including e.g. Coulomb blockade.

When the quantum dot is only weakly coupled to the leads, it is possible to treat the tunneling Hamiltonian as a perturbation, leading to a series expansion in terms of the hybridization strength Γ . One is able to derive a *master equation* to allow calculation of the density-matrix elements. This master equation is then solved e.g. via the technique of real-time diagrammatics, where diagrams of up to some order in Γ are taken into account, while higher order diagrams are neglected [97]. A first-order approximation is referred to as *sequential tunneling*, while the second-order corrections are known as *cotunneling*. This method has proven hugely popular since it allows to study a wide variety of different setups and in many cases allows at least for a qualitative description of different effects. In Sec. 6.2 we compare ISPI data to results from a master equation approach. We thus discuss this method in more detail in App. B.

The perturbative methods provide powerful tools in the parameter ranges where they are applicable, respectively. There exist, however, several nonperturbative effects that are missed in studies with these methods by construction. Additionally, it can be difficult to link the results from perturbative methods to experimental measurements, since often they are only reproduced qualitatively but not quantitatively by perturbative approaches. As a result, numerically exact methods are in high demand, allowing not only a check of the reliability of perturbative methods, but also an expansion of the accessible parameter ranges of the systems. There are several numerically exact methods that have been established for quantum-dot models.

Several flavors of *quantum Monte Carlo simulations* (QMC) have been applied to different kinds of quantum-dot models. We are not aware of previous works where the method has been applied to the quantum-dot spin valve, but such a system should be in the scope of the method. The different approaches are usually based on diagrammatic QMC methods [98, 99], where the theory is expanded with respect to one part of the Hamiltonian, similar to perturbative approaches. Yet, QMC allows sampling over all orders n of the expansion and all times t_1, \dots, t_n of the different vertices. Different flavors of the method utilize different expansions of the Hamiltonian: CT-INT and CT-AUX both expand with respect to the interaction part of the Hamiltonian, with CT-AUX introducing an auxiliary field decomposition to the interaction part [100]. Both allow an easy treatment of large systems, but difficulty increases for complicated onsite interactions. CT-HYB is complimentary to the other two, expanding in terms of the tunneling Hamiltonian [101]. It excels when interactions are complicated, but is limited to smaller systems. Finally, CT-J

was developed to handle Kondo-like problems. All these methods are plagued by the *negative-sign problem*, which becomes increasingly complicated for longer propagation times. As a result, QMC methods are limited to the short-to-intermediate time range. Yet there have been significant developments to the formalism to tackle the negative-sign problem [102].

A different approach is taken by *renormalization group theories*. This family of methods revolves around intelligent truncation of the many-body Hilbert space. Two renormalization group methods are widely applied to quantum-dot systems, including the quantum-dot spin valve: numerical (NRG) [103] and density-matrix renormalization group theory (DMRG) [104]. Different approaches are of course possible and actively developed. For the NRG method the leads' continuous energy spectra are discretized logarithmically around the Fermi energy [105], while for the DMRG approach one isolates low-lying energy states of interest [106]. These methods prove especially useful to describe low-energy properties of the system but have difficulties to account for a large range of energies [78, 107].

3.4 Summary

In this chapter we introduced the Hamiltonian for the quantum-dot spin valve. It is built from a single-level, interacting quantum dot that is tunnel-coupled to two Stoner ferromagnets. Due to the magnetizations and polarizations of the ferromagnetic leads, the coupling between quantum dot and leads is spin-dependent. For the noninteracting Hamiltonian we were able to derive analytic solutions for the electric current through the system as well as for local observables, namely the occupation number and the spin projection of the quantum dot. These noninteracting solutions are used in Chap. 6 as one benchmark for the ISPI technique. However, neglecting Coulomb interactions on the quantum dot is not realistic. To allow the discussion of the electronic transport through an interacting quantum-dot spin valve, intelligent approximations are necessary. We discussed some prominent approaches to tackle this problem and set them in relation to the ISPI technique used in this work. We argued that ISPI is a powerful method that operates in parameter regimes, where other methods fail, and thus can help to reach a more complete picture of the whole parameter space, when combined with these different approaches.

4 Coherent-State Path Integrals

The theory of path integrals was first introduced by Feynman in 1948 as an alternative description of nonrelativistic quantum mechanics [108]. Since then the path integral formalism was applied to a wide variety of problems in physics, including many-body theory [65, 68]. The ISPI technique is based on this path-integral formulation of many-body theory. Therefore, in this chapter we introduce the formalism of coherent-state path integrals, and apply it to the problem of electronic transport through a quantum-dot spin valve. We make use of the mathematical concepts from Chapter 2 to calculate the partition function of the system using a path-integral ansatz. We do this first for the noninteracting case and then introduce interactions later on. To treat the quartic part in the dot degrees of freedom arising from the Coulomb term in the dot's Hamiltonian, Eq. (3.9), we decouple it via a discrete Hubbard-Stratonovich transformation. Finally, we transfer the resulting partition function into a generating functional, by including a source term, which allows us to calculate expectation values for different observables of our system. We introduce the source terms for the current as well as the occupation number of the quantum dot and the three components of accumulated spin on the quantum dot.

The first section mostly follows the path outlined in Refs. [54, 109], applying their ansatz for a simple toy model to our model of the quantum-dot spin valve with the Hamiltonian \mathcal{H} introduced in Sec. 3.1. We define the nonequilibrium partition function as

$$Z = \text{tr}(\mathcal{U}_C \rho_0), \quad (4.1)$$

where we choose the initial density matrix of our system to be the equilibrium density matrix

$$\rho_0 \equiv \frac{e^{-\beta[\mathcal{H}_{\text{dot}} + \sum_{\alpha}(\mathcal{H}_{\alpha} - \mu_{\alpha} \mathcal{N}_{\alpha})]}}{\text{tr} e^{-\beta[\mathcal{H}_{\text{dot}} + \sum_{\alpha}(\mathcal{H}_{\alpha} - \mu_{\alpha} \mathcal{N}_{\alpha})]}}, \quad (4.2)$$

with $\beta = \frac{1}{k_B T}$ and $\mathcal{N}_{\alpha} = \sum_{\mathbf{k}} c_{\alpha\mathbf{k}}^{\dagger} c_{\alpha\mathbf{k}}$. The unitary Keldysh contour evolution operator, \mathcal{U}_C , is given in terms of the evolution operators defined in Section 2.1 by

$$\mathcal{U}_C = \mathcal{U}_{-\infty, \infty} \mathcal{U}_{\infty, -\infty}. \quad (4.3)$$

From its definition it is clear, that the evolution operator is equal to the unit operator as long as no external fields break the symmetry between forward and backward propagation of the Keldysh contour. As a result the partition function is normalized

$$Z = \text{tr}(\mathbf{1} \rho_0) = 1. \quad (4.4)$$

In Sec. 4.3 we show that one is able to explicitly break the time-inversion symmetry via a source term to receive the expectation value of some observable of the system. For now, however, we work out the partition function using Eq. (4.1) and fermionic coherent states. The generalized Fock space of our system is built from the direct product of the Fock spaces of the free dot and the leads, $\mathcal{F} = \mathcal{F}_{\text{dot}} \otimes \mathcal{F}_L \otimes \mathcal{F}_R$. The coherent states $|\xi\rangle = |\phi, \psi_L, \psi_R\rangle$ are then elements of \mathcal{F} and obey the following eigenvalue equations

$$\begin{aligned} c_{\alpha\mathbf{k}\tau} |\xi\rangle &= \psi_{\alpha\mathbf{k}\tau} |\xi\rangle \\ d_{\sigma} |\xi\rangle &= \phi_{\sigma} |\xi\rangle, \end{aligned} \quad (4.5)$$

where $\psi_{\alpha\mathbf{k}\tau}$ and ϕ_{σ} are both Grassmann numbers. Similar equations are true for the dual vector $\langle\xi|$ and the respective creation operators

$$\begin{aligned} \langle\xi| c_{\alpha\mathbf{k}\tau}^{\dagger} &= \langle\xi| \bar{\psi}_{\alpha\mathbf{k}\tau} \\ \langle\xi| d_{\sigma}^{\dagger} &= \langle\xi| \bar{\phi}_{\sigma}. \end{aligned} \quad (4.6)$$

We emphasize that ϕ_{σ} and $\bar{\phi}_{\sigma}$ are independent Grassmann numbers, that are not somehow connected. The same is true for $\psi_{\alpha\mathbf{k}\tau}$ and $\bar{\psi}_{\alpha\mathbf{k}\tau}$. Since we introduced spinors for the creation and annihilation operators for the Hamiltonian (cf. Sec. 3.1), we also make use of a spinor notation for the Grassmann eigenvalues, given by

$$\begin{aligned} \mathcal{C}_{\alpha\mathbf{k}} |\xi\rangle &= \Psi_{\alpha\mathbf{k}} |\xi\rangle \\ \mathcal{D} |\xi\rangle &= \Phi |\xi\rangle, \end{aligned} \quad (4.7)$$

and $\bar{\Psi}_{\alpha\mathbf{k}}, \bar{\Phi}$ being defined accordingly.

The nonequilibrium partition function, Z , from Eq. (4.1) can be written in terms of a path integral ansatz the following way

$$Z = \int \mathcal{D} [\bar{\Phi}, \Phi, \bar{\Psi}_{\alpha\mathbf{k}}, \Psi_{\alpha\mathbf{k}}] e^{i(S_{\text{dot}} + \sum_{\alpha} (S_{\alpha} + S_{T,\alpha}))}, \quad (4.8)$$

where S_{dot} is the action caused by the dot Hamiltonian \mathcal{H}_{dot} , Eq. (3.9), S_{α} is the action for lead α , Eq. (3.5), and $S_{T,\alpha}$ is the action due to the hybridization of the dot by the leads, Eq. (3.10). The integration measure is given by

$$\mathcal{D} [\bar{\Phi}, \Phi, \bar{\Psi}_{\alpha\mathbf{k}}, \Psi_{\alpha\mathbf{k}}] = \lim_{N \rightarrow \infty} \prod_{l=1}^N \prod_{\nu=\pm} \frac{\mathcal{d} [\bar{\Phi}_l^{\nu}, \Phi_l^{\nu}, \bar{\Psi}_{\alpha\mathbf{k},l}^{\nu}, \Psi_{\alpha\mathbf{k},l}^{\nu}]}{\text{tr} e^{-\beta[\mathcal{H}_{\text{dot}} + \sum_{\alpha} (\mathcal{H}_{\alpha} - \mu_{\alpha} \mathcal{N}_{\alpha})]}}. \quad (4.9)$$

Here $l = 1, \dots, N$ denotes the physical time step and $\nu = \pm$ the branch of the Keldysh contour, see Eq. (4.10). This equation and the form of the action $S = S_{\text{dot}} + \sum_{\alpha} (S_{\alpha} + S_{T,\alpha})$ are derived in what follows.

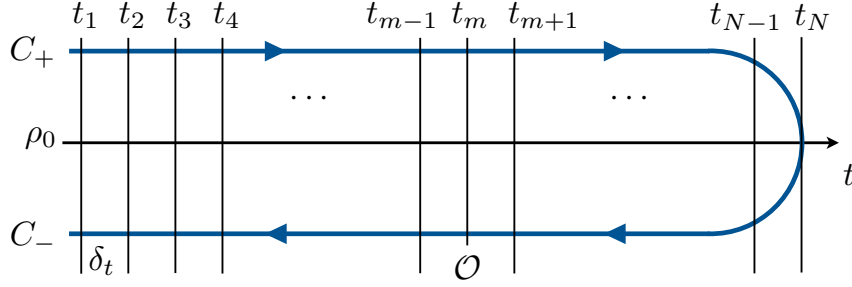


Figure 4.1: The Keldysh contour sliced into $2N$ parts with N slices on the C_+ branch, and N on the C_- branch. The discretization length is constant, given by δ_t . The source term of some observable \mathcal{O} is introduced at measurement time t_m .

4.1 Noninteracting Limit

In Sec. 3.2 we already derived a noninteracting solution for current, occupation number and spin projection using a nonequilibrium Green function approach. Including interactions within this derivation prohibits an analytical solution and approximations are necessary. This is similarly the case when applying the path-integral formalism. Therefore, we neglect interactions during this section, to allow ourselves a straightforward introduction of the path-integral formalism for the quantum-dot spin valve. Interactions are then reintroduced in Sec. 4.2.

4.1.1 Building the Path Integral

To construct the path integral representation of the partition function, Eq. (4.1), we first employ the Trotter break-up for the evolution operator $\mathcal{U}_{t,t'}$ from Eq. (2.5), leading to a time-discrete version of \mathcal{U}_C . Since the Hamiltonian is not explicitly time-dependent, we find

$$Z = \lim_{N \rightarrow \infty} \text{tr} \left((\mathcal{U}_{-\delta_t})^N (\mathcal{U}_{\delta_t})^N \rho_0 \right), \quad (4.10)$$

with short-time evolution operators $\mathcal{U}_{\pm\delta_t} = e^{\mp i\delta_t \mathcal{H}}$. This discretizes the Keldysh contour in $2N$ time steps total (N on the forward branch and N on the backward branch of the contour), which are all of size δ_t such that $N\delta_t = \text{const}$ (see. Fig. 4.1). We emphasize that $\mathcal{U}_C = (\mathcal{U}_{-\delta_t})^N (\mathcal{U}_{\delta_t})^N$ is only true up to first order in δ_t . Due to the limit $\lim_{N \rightarrow \infty}$ this is not an issue on an analytical basis. For a numerical treatment this introduces a systematic error, which we address during Sec. 5.3. The trace may then be rewritten in terms of fermionic coherent states, via Eq. (2.47), leading to

$$Z = \lim_{N \rightarrow \infty} \int d[\bar{\Phi}, \Phi, \bar{\Psi}_{\alpha\mathbf{k}}, \Psi_{\alpha\mathbf{k}}] e^{-\bar{\Phi}\Phi - \sum_{\alpha\mathbf{k}} \bar{\Psi}_{\alpha\mathbf{k}} \Psi_{\alpha\mathbf{k}}} \langle -\xi | (\mathcal{U}_{-\delta_t})^N (\mathcal{U}_{\delta_t})^N \rho_0 | \xi \rangle. \quad (4.11)$$

We are now able to insert additional unit operators between each pair of evolution operators, by using the resolution of unity in terms of coherent states, given in Eq. (2.46). This leads to a total of $2N$ sets of Grassmann fields, over which we have to integrate. For the sake of clarity, we employ the following naming convention: $l = 1, \dots, N$ counts the physical time-steps, while $\nu = \pm$ labels the Keldysh branch C_ν . We use this convention to enumerate the different states and Grassmann fields along the Keldysh contour, cf. Fig 4.1 for a graphical representation. We find the following sequence

$$\begin{aligned} Z &= \lim_{N \rightarrow \infty} \int \prod_{\nu=\pm} \prod_{l=1}^N d[\bar{\Phi}_l^\nu, \Phi_l^\nu, \bar{\Psi}_{\alpha\mathbf{k},l}^\nu, \Psi_{\alpha\mathbf{k},l}^\nu] e^{\sum_{\nu=\pm} \sum_{l=1}^N (-\bar{\Phi}_l^\nu \Phi_l^\nu - \sum_{\alpha\mathbf{k}} \bar{\Psi}_{\alpha\mathbf{k},l}^\nu \Psi_{\alpha\mathbf{k},l}^\nu)} \\ &\times \langle \xi_1^- | \mathcal{U}_{-\delta_t} | \xi_2^- \rangle \langle \xi_2^- | \mathcal{U}_{-\delta_t} | \xi_3^- \rangle \cdots \langle \xi_{N-1}^- | \mathcal{U}_{-\delta_t} | \xi_N^- \rangle \langle \xi_N^- | \mathbb{1} | \xi_N^+ \rangle \\ &\times \langle \xi_N^+ | \mathcal{U}_{+\delta_t} | \xi_{N-1}^+ \rangle \langle \xi_{N-1}^+ | \mathcal{U}_{+\delta_t} | \xi_{N-2}^+ \rangle \cdots \langle \xi_2^+ | \mathcal{U}_{+\delta_t} | \xi_1^+ \rangle \langle -\xi_1^+ | \rho_0 | \xi_1^- \rangle. \end{aligned} \quad (4.12)$$

Reading from right to left, we start with the initial density matrix ρ_0 which connects the lower to the upper branch at time t_1 and continue along C_+ until we reach time t_N , where C_+ is then connected to C_- . From Fig. 4.1 it is clear that at the time t_N no time-evolution happens. This results in a simple overlap of the two fermionic coherent states $\langle \xi_N^- | \xi_N^+ \rangle$, which is given in Eq. (2.44). From this point on, we then propagate backwards in time on the C_- branch until we once again reach the physical time t_1 . Consequently, we are left with calculating the matrix elements of the short-time evolution operators and of the initial density matrix.

Initial density matrix Calculating the matrix elements of the initial density matrix is straightforward. We first plug in the expression of the density matrix and note that we absorb the normalization factor into the integral measure, Eq. (4.9). Thus, we do not include the normalization factor explicitly here, which leads to

$$\langle -\xi_1^+ | \rho_0 | \xi_1^- \rangle = \langle -\xi_1^+ | e^{-\beta(\mathcal{H}_{\text{dot}} + \sum_{\alpha} (\mathcal{H}_{\alpha} - \mu_{\alpha} \mathcal{N}_{\alpha}))} | \xi_1^- \rangle. \quad (4.13)$$

Then, we recall that $|\xi\rangle = |\phi, \psi_L, \psi_R\rangle$, and thus are able to use the identity $\langle \phi | e^{d_{\sigma}^{\dagger} d_{\sigma} \lambda} | \phi' \rangle = e^{\bar{\phi}_{\sigma} \phi'_{\sigma} e^{\lambda}}$ and accordingly for the lead operators. This directly results in

$$\langle -\xi_1^+ | \rho_0 | \xi_1^- \rangle = \exp \left(-\bar{\Phi}_1^+ e^{-\beta \mathcal{E}_0} \Phi_1^- - \sum_{\alpha\mathbf{k}} \bar{\Psi}_{\alpha\mathbf{k},1}^+ e^{-\beta(\mathcal{E}_{\alpha\mathbf{k}} - \mu_{\alpha} \sigma_0)} \Psi_{\alpha\mathbf{k},1}^- \right). \quad (4.14)$$

Short-time evolution operator For the short-time evolution operator, we are able to split the tunneling Hamiltonian $\mathcal{H}_{T,\alpha}$ from the rest and insert an additional resolution of unity between the two parts

$$\begin{aligned} \langle \xi_{l+1}^{\nu} | \mathcal{U}_{\nu\delta_t} | \xi_l^{\nu} \rangle &= \int d[\bar{\Phi}, \Phi, \bar{\Psi}_{\alpha\mathbf{k}}, \Psi_{\alpha\mathbf{k}}] e^{-\bar{\Phi}\Phi - \sum_{\alpha\mathbf{k}} \bar{\Psi}_{\alpha\mathbf{k}} \Psi_{\alpha\mathbf{k}}} \\ &\times \langle \xi_{l+1}^{\nu} | e^{-\nu i \delta_t (\mathcal{H}_{\text{dot}} + \sum_{\alpha} \mathcal{H}_{\alpha})} | \xi \rangle \langle \xi | e^{-\nu i \delta_t \sum_{\alpha} \mathcal{H}_{T,\alpha}} | \xi_l^{\nu} \rangle. \end{aligned} \quad (4.15)$$

The two parts are then solved individually. Since Coulomb interactions are neglected during this section, solving the first part is straightforward and one readily finds

$$\langle \xi_{l+1}^\nu | e^{-\nu i \delta_t (\mathcal{H}_{\text{dot}} + \sum_\alpha \mathcal{H}_\alpha)} | \xi \rangle = \exp \left(\bar{\Phi}_{l+1}^\nu e^{-\nu i \delta_t \mathcal{E}_0} \Phi + \sum_{\alpha \mathbf{k}} \bar{\Psi}_{\alpha \mathbf{k}, l+1}^\nu e^{-\nu i \delta_t \mathcal{E}_{\alpha \mathbf{k}}} \Psi_{\alpha \mathbf{k}} \right), \quad (4.16)$$

while the tunneling part can be calculated in a similar fashion

$$\begin{aligned} \langle \xi | e^{-\nu i \delta_t \sum_\alpha \mathcal{H}_{T, \alpha}} | \xi_l^\nu \rangle = \exp \left(\bar{\Phi} \Phi_l^\nu + \sum_{\alpha \mathbf{k}} \bar{\Psi}_{\alpha \mathbf{k}} \Psi_{\alpha \mathbf{k}, l}^\nu \right. \\ \left. - \nu i \delta_t \sum_{\alpha \mathbf{k}} [\bar{\Psi}_{\alpha \mathbf{k}} Y_\alpha \Phi_l^\nu + \bar{\Phi} Y_\alpha^\dagger \Psi_{\alpha \mathbf{k}, l}^\nu] \right). \end{aligned} \quad (4.17)$$

To obtain the final expression for the short-time evolution operator, we are left with solving the integrals from Eq. (4.15). For this we expand the exponential functions and then perform the integrals over the Grassmann variables. The calculation is lengthy but again straightforward. We only present the final result here

$$\begin{aligned} \langle \xi_{l+1}^\nu | \mathcal{U}_{\nu \delta_t} | \xi_l^\nu \rangle = \exp \left(\bar{\Phi}_{l+1}^\nu e^{-\nu i \delta_t \mathcal{E}_0} \Phi_l^\nu + \sum_{\alpha \mathbf{k}} \bar{\Psi}_{\alpha \mathbf{k}, l+1}^\nu e^{-\nu i \delta_t \mathcal{E}_{\alpha \mathbf{k}}} \Psi_{\alpha \mathbf{k}, l}^\nu \right. \\ \left. - \nu i \delta_t \sum_{\alpha \mathbf{k}} (\bar{\Psi}_{\alpha \mathbf{k}, l+1}^\nu Y_\alpha \Phi_l^\nu + \bar{\Phi}_{l+1}^\nu Y_\alpha^\dagger \Psi_{\alpha \mathbf{k}, l}^\nu) \right), \end{aligned} \quad (4.18)$$

where we reiterate that this is only true up to first order in δ_t .

Having obtained the short-time evolution operator in terms of coherent states as well as the other building blocks, we are able to plug it all back into Eq. (4.12) and find

$$\begin{aligned} Z = \lim_{N \rightarrow \infty} \int \prod_{\nu=\pm} \prod_{l=1}^N \frac{d[\bar{\Phi}_l^\nu, \Phi_l^\nu, \bar{\Psi}_{\alpha \mathbf{k}, l}^\nu, \Psi_{\alpha \mathbf{k}, l}^\nu]}{\text{tr} e^{-\beta [\mathcal{H}_{\text{dot}} + \sum_\alpha (\mathcal{H}_\alpha - \mu_\alpha \mathcal{N}_\alpha)]}} \\ \exp \left[\sum_{\nu=\pm} \left(\sum_{l=1}^N \left(-\bar{\Phi}_l^\nu \Phi_l^\nu - \sum_{\alpha \mathbf{k}} \bar{\Psi}_{\alpha \mathbf{k}, l}^\nu \Psi_{\alpha \mathbf{k}, l}^\nu \right) + \sum_{l=1}^{N-1} \left(\bar{\Phi}_{l+1}^\nu e^{-\nu i \delta_t \mathcal{E}_0} \Phi_l^\nu \right. \right. \right. \\ \left. \left. + \sum_{\alpha \mathbf{k}} [\bar{\Psi}_{\alpha \mathbf{k}, l+1}^\nu e^{-\nu i \delta_t \mathcal{E}_{\alpha \mathbf{k}}} \Psi_{\alpha \mathbf{k}, l}^\nu - \nu i \delta_t (\bar{\Psi}_{\alpha \mathbf{k}, l+1}^\nu Y_\alpha \Phi_l^\nu + \bar{\Phi}_{l+1}^\nu Y_\alpha^\dagger \Psi_{\alpha \mathbf{k}, l}^\nu)] \right) \right) \\ \left. + \bar{\Phi}_N^- \Phi_N^+ - \bar{\Phi}_1^+ e^{-\beta \mathcal{E}_0} \Phi_1^- + \sum_{\alpha \mathbf{k}} (\bar{\Psi}_{\alpha \mathbf{k}, N}^- \Psi_{\alpha \mathbf{k}, N}^+ - \bar{\Psi}_{\alpha \mathbf{k}, 1}^+ e^{-\beta (\mathcal{E}_{\alpha \mathbf{k}} - \mu_\alpha \sigma_0)} \Psi_{\alpha \mathbf{k}, 1}^-) \right]. \end{aligned} \quad (4.19)$$

Note that several signs change between the two branches of the Keldysh contour, which is due to the change of propagation direction in time. Collecting addends in the exponential with the same combination of dot and lead Grassmann fields, we

are able to identify four different matrices. The expressions between the Grassmann fields are the elements of these matrices. If we recall that the expression above still has a 2×2 spin substructure, the total dimension of these matrices is $4N \times 4N$. As a result we find

$$Z = \lim_{N \rightarrow \infty} \int \prod_{\nu=\pm} \prod_{l=1}^N \frac{d[\bar{\Phi}_l^\nu, \Phi_l^\nu, \bar{\Psi}_{\alpha\mathbf{k},l}^\nu, \Psi_{\alpha\mathbf{k},l}^\nu]}{\text{tr} e^{-\beta[\mathcal{H}_{\text{dot}} + \sum_{\alpha} (\mathcal{H}_{\alpha} - \mu_{\alpha} \mathcal{N}_{\alpha})]}} \exp \left[\sum_{\nu, \nu'=\pm} \sum_{l, l'=1}^N \left(\bar{\Phi}_l^\nu i(G_0^{-1})_{ll'}^{\nu\nu'} \Phi_{l'}^{\nu'} \right. \right. \\ \left. \left. + \sum_{\alpha\mathbf{k}} \bar{\Psi}_{\alpha\mathbf{k},l}^\nu i(g_{\alpha\mathbf{k}}^{-1})_{ll'}^{\nu\nu'} \Psi_{\alpha\mathbf{k},l'}^{\nu'} - \bar{\Psi}_{\alpha\mathbf{k},l}^\nu i(T_{\alpha})_{ll'}^{\nu\nu'} \Phi_{l'}^{\nu'} - \bar{\Phi}_l^\nu i(T_{\alpha}^{\dagger})_{ll'}^{\nu\nu'} \Psi_{\alpha\mathbf{k},l'}^{\nu'} \right) \right] \quad (4.20)$$

The true nature of the matrices G_0 , $g_{\alpha\mathbf{k}}$, and T_{α} , T_{α}^{\dagger} becomes apparent, once we take the limit $N \rightarrow \infty$, leading to Eq. (4.8). Comparing Eq. (4.20) with Eq. (4.8) shows that the exponent is the action S and we are able to identify its different parts. For the part including only dot degrees of freedom we find

$$S_{\text{dot}} = \lim_{N \rightarrow \infty} \sum_{\nu=\pm} \sum_{l=1}^N \nu \delta_t \left(i \bar{\Phi}_{l+\nu}^\nu \frac{\Phi_{l+\nu}^\nu - \Phi_l^\nu}{\nu \delta_t} - \bar{\Phi}_{l+\nu}^\nu \mathcal{E}_0 \Phi_l^\nu \right) + i \bar{\Phi}_N^- \Phi_N^+ + \Phi_1^+ e^{-\beta \mathcal{E}_0} \Phi_1^- \\ = \int d\tilde{t} \bar{\Phi}(\tilde{t}) (i \partial_{\tilde{t}} \sigma_0 - \mathcal{E}_0) \Phi(\tilde{t}) = \int d\tilde{t} \bar{\Phi}(\tilde{t}) G_0^{-1}(\tilde{t}, \tilde{t}) \Phi(\tilde{t}). \quad (4.21)$$

To account for the limit in the second step we made the replacements $\bar{\Phi}_l^\nu \rightarrow \bar{\Phi}(\tilde{t})$, $\Phi_l^\nu \rightarrow \Phi(\tilde{t})$ and $\delta_t \sum_{\nu=\pm} \sum_{l=1}^N \rightarrow \int d\tilde{t}$, while in the last step we identified the inverse of the free quantum dot's nonequilibrium Green function $G_0^{-1}(\tilde{t}, \tilde{t}) = i \partial_{\tilde{t}} \sigma_0 - \mathcal{E}_0$. The other parts of the action are evaluated in an analogue manner

$$S_{\alpha} = \sum_{\mathbf{k}} \int d\tilde{t} \bar{\Psi}_{\alpha\mathbf{k}}(\tilde{t}) (i \partial_{\tilde{t}} \sigma_0 - \mathcal{E}_{\alpha\mathbf{k}}) \Psi_{\alpha\mathbf{k}}(\tilde{t}) = \sum_{\mathbf{k}} \int d\tilde{t} \bar{\Psi}_{\alpha\mathbf{k}}(\tilde{t}) g_{\alpha\mathbf{k}}^{-1}(\tilde{t}, \tilde{t}) \Psi_{\alpha\mathbf{k}}(\tilde{t}) \\ S_{T,\alpha} = - \sum_{\mathbf{k}} \int d\tilde{t} (\bar{\Psi}_{\alpha\mathbf{k}}(\tilde{t}) T_{\alpha}(\tilde{t}) \Phi(\tilde{t}) + \text{H.c.}) \quad (4.22)$$

Again, we identified the inverse of the leads' nonequilibrium Green function, given by $g_{\alpha\mathbf{k}}^{-1}(\tilde{t}, \tilde{t}) = i \partial_{\tilde{t}} \sigma_0 - \mathcal{E}_{\alpha\mathbf{k}}$. It is immediately apparent that the time-continuous actions have to be handled with care, since the boundary terms, which are off-diagonal in Keldysh space, are neglected in this representation. This is especially problematic for the terms $\Phi_1^+ e^{-\beta \mathcal{E}_0} \Phi_1^-$ and $\bar{\Psi}_{\alpha\mathbf{k},1}^+ e^{-\beta(\mathcal{E}_{\alpha\mathbf{k}} - \mu_{\alpha} \sigma_0)} \Psi_{\alpha\mathbf{k},1}^-$ in the free dot and leads Green functions, respectively. These terms are necessary to keep the normalization in tact, which we established in Eq. (4.4). Consequently, the continuous notation can only act as an abbreviation of the discrete notation. Thus, in what follows we work with the previously introduced $4N \times 4N$ matrices G_0 and $g_{\alpha\mathbf{k}}$. Importantly, these matrices are fully occupied in Keldysh space (see Ref. [54]). To remain consistent, we do not use the time-continuous tunnel action $S_{T,\alpha}$ from Eq. (4.22) but return to

the discrete matrices in Eq. (4.20) and compare it with Eq. (4.19), we find that the matrices T_α and T_α^\dagger should take the form

$$(T_\alpha)_{ll'}^{\nu\nu'} = \delta_{ll'} \delta_{\nu\nu'} \nu Y_\alpha \quad (4.23)$$

$$(T_\alpha^\dagger)_{ll'}^{\nu\nu'} = \delta_{ll'} \delta_{\nu\nu'} \nu Y_\alpha^\dagger. \quad (4.24)$$

4.1.2 Solving the Path Integral

Having derived the path integral formulation of the partition function, Eq. (4.8), we are left with the task of solving the path integral. To perform these high-dimensional integrals we make use of the discrete notation including the Green functions, see Eq. (4.20). The exact form of these matrices is derived later on. The partition function is given by

$$Z = \int D[\bar{\Phi}, \Phi, \bar{\Psi}_{\alpha\mathbf{k}}, \Psi_{\alpha\mathbf{k}}] \exp \left[\sum_{\nu, \nu' = \pm} \sum_{l, l' = 1}^N \left(\bar{\Phi}_l^\nu i (G_0^{-1})_{ll'}^{\nu\nu'} \Phi_{l'}^{\nu'} \right. \right. \\ \left. \left. + \sum_{\alpha\mathbf{k}} \bar{\Psi}_{\alpha\mathbf{k}, l}^\nu i (g_{\alpha\mathbf{k}}^{-1})_{ll'}^{\nu\nu'} \Psi_{\alpha\mathbf{k}, l'}^{\nu'} - \bar{\Psi}_{\alpha\mathbf{k}, l}^\nu i (T_\alpha)_{ll'}^{\nu\nu'} \Phi_{l'}^{\nu'} - \bar{\Phi}_l^\nu i (T_\alpha^\dagger)_{ll'}^{\nu\nu'} \Psi_{\alpha\mathbf{k}, l'}^{\nu'} \right) \right]. \quad (4.25)$$

For the noninteracting case both, the dot degrees of freedom and the lead degrees of freedom, appear bilinearly and thus the integrals can be solved exactly. Starting with the lead degrees of freedom, we make use of the identity given in Eq. (2.37), leading to

$$Z = \det \left(-i \sum_{\alpha\mathbf{k}} g_{\alpha\mathbf{k}}^{-1} \right) \int D[\bar{\Phi}, \Phi] \exp \left[\sum_{\nu, \nu' = \pm} \sum_{l, l' = 1}^N \left(\bar{\Phi}_l^\nu i (G_0^{-1})_{ll'}^{\nu\nu'} \Phi_{l'}^{\nu'} \right. \right. \\ \left. \left. - i \sum_{\alpha\mathbf{k}} \sum_{\tilde{\nu}, \tilde{\nu}' = \pm} \sum_{\tilde{l}, \tilde{l}' = 1}^N \bar{\Phi}_{\tilde{l}}^{\tilde{\nu}} (T_\alpha^\dagger)_{\tilde{l}\tilde{l}'}^{\tilde{\nu}\tilde{\nu}'} (g_{\alpha\mathbf{k}})_{\tilde{l}\tilde{l}'}^{\tilde{\nu}\tilde{\nu}'} (T_\alpha)_{\tilde{l}'\tilde{l}}^{\tilde{\nu}'\tilde{\nu}} \Phi_{\tilde{l}'}^{\tilde{\nu}'} \right) \right]. \quad (4.26)$$

Solving the integrals over dot degrees of freedom by applying Eq. (2.34), we find

$$Z = \det \left(-i \sum_{\alpha\mathbf{k}} g_{\alpha\mathbf{k}}^{-1} \right) \det \left(i \left(G_0^{-1} - i \sum_{\alpha\mathbf{k}} T_\alpha^\dagger g_{\alpha\mathbf{k}} T_\alpha \right) \right). \quad (4.27)$$

We note, that the first determinant will cancel in future calculations, allowing us to neglect it here. Also, the prefactor of i in the second determinant can be neglected, since it only amounts to a multiplication by 1, since $i^{4N} = 1$. We are able to define the tunneling self energies

$$\Sigma_{T, \alpha} = \sum_{\mathbf{k}} T_\alpha^\dagger g_{\alpha\mathbf{k}} T_\alpha, \quad (4.28)$$

allowing us to write the noninteracting partition function in its final form

$$Z = \det \left(G_0^{-1} - \sum_{\alpha} \Sigma_{T, \alpha} \right) = \det (\Delta^{-1}), \quad (4.29)$$

where we introduced the noninteracting, discrete, dressed Green function in presence of the leads $\Delta = (G_0^{-1} - \sum_{\alpha} \Sigma_{\alpha})^{-1}$. This then constitutes the final result for the partition function of the noninteracting quantum-dot spin valve.

4.1.3 Time-Discrete Dressed Green Function

To find an expression for the matrix Δ in Eqs. (4.29) it is useful to start in Fourier space and return to the time representation via a Fourier transform at the end. The energy representations of the free retarded and advanced Green functions are well known and have been introduced before for the leads, Eq. (3.20). A useful representation of the leads' nonequilibrium Green functions is obtained via the basis derived in Eq. (2.18) and letting the inverse Keldysh rotation act on this expression. The result is the following expression for the lead Green functions (see Appendix C for a derivation)

$$g_{\alpha\mathbf{k}} = \begin{pmatrix} g_{\alpha\mathbf{k}}^R & 0 \\ 0 & -g_{\alpha\mathbf{k}}^A \end{pmatrix} + (g_{\alpha\mathbf{k}}^A - g_{\alpha\mathbf{k}}^R) \begin{pmatrix} f_{\alpha}(\omega) & f_{\alpha}(\omega) \\ f_{\alpha}(\omega) - 1 & f_{\alpha}(\omega) \end{pmatrix}, \quad (4.30)$$

where the Fermi function for lead α is $f_{\alpha}(\omega) = (1 + \exp(\beta(\omega - \mu_{\alpha})))^{-1}$. We always have to sum over the lead Green functions with respect to \mathbf{k} . To evaluate this sum, we transform it into an integral via $\sum_{\mathbf{k}} \rightarrow \int d\varepsilon_{\alpha\tau} \rho(\varepsilon_{\alpha\tau})$ and we assume to be in the wide-band limit $\rho(\varepsilon_{\alpha\tau}) \approx \rho(\varepsilon_{\alpha\tau}^F)$. This is similar to the steps used in Sec. 3.2. With this we find

$$\sum_{\mathbf{k}} g_{\alpha\mathbf{k}}(\omega) = i\pi \begin{pmatrix} 2f_{\alpha}(\omega) - 1 & 2f_{\alpha}(\omega) \\ 2f_{\alpha}(\omega) - 2 & 2f_{\alpha}(\omega) - 1 \end{pmatrix} \otimes \begin{pmatrix} \rho(\varepsilon_{\alpha+}^F) & 0 \\ 0 & \rho(\varepsilon_{\alpha-}^F) \end{pmatrix}, \quad (4.31)$$

where we used the relation $\lim_{\eta \rightarrow 0^+} \frac{1}{\omega \pm i\eta} = \mathcal{P} \frac{1}{\omega} \mp i\pi\delta(\omega)$ as well as the representation of the δ -distribution $\pi\delta(\omega) = \lim_{\eta \rightarrow 0} \frac{\eta}{\omega^2 + \eta^2}$.

To reach an expression for the tunneling self energies, we multiply the lead Green function with $\kappa_z \otimes Y_{\alpha}^{\dagger}$ from the left and $\kappa_z \otimes Y_{\alpha}$ from the right, respectively, where κ_z is a Pauli matrix in Keldysh space (see Eqs. (4.23)). The resulting tunneling self energy then takes the form

$$\Sigma_{\text{T},\alpha}(\omega) = \frac{i}{2} \begin{pmatrix} 2f_{\alpha}(\omega) - 1 & -2f_{\alpha}(\omega) \\ -(2f_{\alpha}(\omega) - 2) & 2f_{\alpha}(\omega) - 1 \end{pmatrix} \otimes \begin{pmatrix} \Gamma_{\alpha} & \Gamma_{\alpha} p_{\alpha} e^{-i\theta/2} \\ \Gamma_{\alpha} p_{\alpha} e^{i\theta/2} & \Gamma_{\alpha} \end{pmatrix}, \quad (4.32)$$

where we introduced the spin-dependent hybridization given by $\Gamma_{\alpha\tau} = 2\pi t_{\alpha}^2 \rho(\varepsilon_{\alpha\tau}^F)$, which can be written with help of the polarization as $\Gamma_{\alpha\tau} = \Gamma_{\alpha}(1 + \tau p_{\alpha})$, using $\Gamma_{\alpha} = \sum_{\tau} \Gamma_{\alpha\tau}/2$.

The inverse Green function of the free quantum dot including a Zeeman field is well known to be

$$G_0^{-1}(\omega) = \kappa_z \otimes \begin{pmatrix} \omega - \varepsilon_0 - B_z & -B_x + iB_y \\ -B_x - iB_y & \omega - \varepsilon_0 + B_z \end{pmatrix}. \quad (4.33)$$

We note, that this equation is diagonal in Keldysh space, meaning we did neglect the initial density matrix of the quantum dot. This is not an issue thanks to the presence of the leads and since we only study the long-time limit. However, it changes the normalization of the generating functional, Eq. (4.4). Again, this is not problematic since we will always take the derivative of the generating functional to obtain the expectation values of observables.

With Eq. (4.33) and Eq. (4.32) we are able to write down $\Delta(\omega)$ according to its definition in Eq. (4.29). To obtain its time representation, we have to Fourier transform the expression, which can be either done analytically using the residue theorem or numerically by discretizing the expression in energy space and then applying a discrete Fourier transformation. The analytical Fourier transform via the residue theorem is shown in Appendix D. The result is then given by

$$\Delta_{ll'} = \int \frac{d\omega}{2\pi} e^{-i\omega(t-l')\delta_t} \left[G_0^{-1}(\omega) - \sum_{\alpha} \Sigma_{T,\alpha}(\omega) \right]^{-1}, \quad (4.34)$$

where Δ is then a $4N \times 4N$ Toeplitz style matrix with a 2×2 substructure for spin and a 2×2 substructure to account for the Keldysh branches. With it we are able to calculate the partition function, Eq. (4.29).

4.2 Interactions

While the noninteracting quantum-dot spin valve can be solved analytically via nonequilibrium Green functions (see Sec. 3.2), more elaborate, approximate approaches are necessary once Coulomb interactions cannot be neglected anymore. The path-integral formulation is well suited as a starting point for such approaches. The interaction part in the Hamiltonian, Eq. (3.9), is not bilinear in the dot's creation/annihilation operators but quartic. Such a term prohibits us from solving the integral over the dot degrees of freedom in a straight forward manner, as we did to reach the final expression for the noninteracting case Eq. (4.29). Instead we introduce a discrete Hubbard-Stratonovich transformation to decouple the quartic interaction term for each time t on the Keldysh contour C . The main idea of the Hubbard-Stratonovich transformation is to replace a term that is quartic in the Grassmann fields with terms that are only bilinear in these fields, at the cost of coupling it to newly introduced Ising-like degrees of freedom, $s_t = \pm 1$ [110, 111].

To enable a numerical implementation of the Hubbard-Stratonovich transformation, we have to work with the discretized Keldysh contour, where C_+ and C_- are split into N time slices of length δ_t each. This is what we already have in Eq. (4.29) allowing us to simply modify its derivation. The interaction term will be present on each time slice, and we implement the following identity to decouple it on each time slice

$$\exp\left(-\nu \frac{i\delta_t U}{2} (\bar{\Phi}_{\nu} \sigma_z \Phi_{\nu})^2\right) = \frac{1}{2} \sum_{s=\pm 1} \exp(-s\lambda_{\nu} \bar{\Phi}_{\nu} \sigma_z \Phi_{\nu}), \quad (4.35)$$

with s being an Ising-like degree of freedom called the Hubbard-Stratonovich spin. Such an independent degree of freedom emerges on each time slice. One possible solution for the Hubbard-Stratonovich parameter λ_ν is given by [87, 93, 111]

$$\lambda_\nu = \cosh^{-1} \left[\cos \left(\delta_t \frac{U}{2} \right) - i\nu \sin \left(\delta_t \frac{U}{2} \right) \right], \quad (4.36)$$

where $0 < U < \pi/\delta_t$. After having implemented the Hubbard-Stratonovich transformation, the dot degrees of freedom, again, only appear bilinearly in the path integral and therefore can be integrated out similarly as demonstrated in Sec. 4.1.2. The result is analogue to Eq. (4.29) but includes an additional *charging self energy* Σ_C that depends on the Hubbard-Stratonovich spins

$$Z = \sum_{\{\mathbf{s}\}} \det (\Delta^{-1} - \Sigma_C[\mathbf{s}]). \quad (4.37)$$

We introduced the Ising spin vector $\mathbf{s} = (s_1^+, s_1^-, s_2^+, s_2^-, \dots, s_N^+, s_N^-)$. The charging self energy is a diagonal $4N \times 4N$ matrix with elements

$$(\Sigma_C[\mathbf{s}])_{ll'} = \delta_{ll'} \begin{pmatrix} \lambda_+ s_l^+ & 0 \\ 0 & \lambda_- s_l^- \end{pmatrix} \otimes \sigma_z. \quad (4.38)$$

The sum over all possible spin configurations in Eq. (4.37) is not feasible, since it would require summation of 2^{2N} terms, where N is usually of the order several hundreds. Consequently, the summation has to be performed approximately, with a more efficient approach. This will be discussed in Chapter 5. In the last section of this chapter, we focus on including various source terms in the path-integral formalism that allow us to extract expectation values of several observables from the theory.

4.3 Observables and Source Terms

Source terms are implemented as external fields in the path-integral formalism that break the time inversion symmetry. The source term has to be specifically designed to enable the calculation of the expectation values of one specific observable and has to be changed to calculate different observables. In this thesis we focus on observables that are one of the following: the current, or observables that can be calculated directly from the current (linear conductance, differential conductance, TMR), as well as the occupation number of the quantum dot or the spin projections of quantum dot.

To find the form of the fitting source term for an observable \mathcal{O} , we first note how expectation values are calculated within the path integral formalism

$$\langle \mathcal{O} \rangle = \frac{\int \mathcal{D} [\bar{\Phi}, \Phi, \bar{\Psi}_{\alpha\mathbf{k}}, \Psi_{\alpha\mathbf{k}}] e^{iS} \mathcal{O} (\bar{\Phi}, \Phi, \bar{\Psi}_{\alpha\mathbf{k}}, \Psi_{\alpha\mathbf{k}})}{\int \mathcal{D} [\bar{\Phi}, \Phi, \bar{\Psi}_{\alpha\mathbf{k}}, \Psi_{\alpha\mathbf{k}}] e^{iS}}, \quad (4.39)$$

where $O(\bar{\Phi}, \Phi, \bar{\Psi}_{\alpha\mathbf{k}}, \Psi_{\alpha\mathbf{k}})$ is the operator \mathcal{O} in terms of the lead and dot Grassmann fields. We are able to write this as a derivation by including a multiplier η , which we choose to be real. We also note that the observables we work with are all local in time, meaning that they are all inserted at one physical time t_m , which we call the measurement time. As a result

$$\begin{aligned} \langle \mathcal{O} \rangle &= -i \frac{\delta}{\delta \eta} \frac{\int \mathcal{D} [\bar{\Phi}, \Phi, \bar{\Psi}_{\alpha\mathbf{k}}, \Psi_{\alpha\mathbf{k}}] e^{i(S + \eta O(\bar{\Phi}, \Phi, \bar{\Psi}_{\alpha\mathbf{k}}, \Psi_{\alpha\mathbf{k}}))}}{\int \mathcal{D} [\bar{\Phi}, \Phi, \bar{\Psi}_{\alpha\mathbf{k}}, \Psi_{\alpha\mathbf{k}}] e^{iS}} \Bigg|_{\eta=0} \\ &= -i \frac{\delta}{\delta \eta} \log Z[\eta] \Bigg|_{\eta=0}. \end{aligned} \quad (4.40)$$

where $Z[\eta] = \int \mathcal{D} [\bar{\Phi}, \Phi, \bar{\Psi}_{\alpha\mathbf{k}}, \Psi_{\alpha\mathbf{k}}] e^{i(S + \eta O(\bar{\Phi}, \Phi, \bar{\Psi}_{\alpha\mathbf{k}}, \Psi_{\alpha\mathbf{k}}))}$ is called the generating functional with $Z[0] = Z$ being the partition function. Similar to the case of interactions, to include the source term we only need to modify the derivation of Eq. (4.37) and expand it with another term. As a result we find

$$Z[\eta] = \sum_{\{\mathbf{s}\}} \det(\Delta^{-1} - \Sigma_C[\mathbf{s}] + \eta \Sigma_S). \quad (4.41)$$

Here, $\eta \Sigma_S$ is what we call the *source self energy* which handles the source term and has to be changed for each observable. The exact form is derived in the following sections. Plugging Eq. (4.41) back into Eq. (4.40) to calculate an expectation value, we are able to perform the derivative numerically

$$\langle \mathcal{O} \rangle = -i \frac{\sum_{\{\mathbf{s}\}} \det(\Delta^{-1} - \Sigma_C[\mathbf{s}] + \eta \Sigma_S) - \sum_{\{\mathbf{s}\}} \det(\Delta^{-1} - \Sigma_C[\mathbf{s}])}{\eta \sum_{\{\mathbf{s}\}} \det(\Delta^{-1} - \Sigma_C[\mathbf{s}])} \quad (4.42)$$

For the sake of numerical stability of the ISPI method (see Chap. 5) we require the use of the Toeplitz matrix Δ instead of its inverse. This can be achieved by expanding above equation with $\det(\Delta)$, leading to

$$\begin{aligned} \langle \mathcal{O} \rangle &= -i \frac{\sum_{\{\mathbf{s}\}} \det(\mathbb{1} - \Sigma_C[\mathbf{s}]\Delta + \eta \Sigma_S\Delta) - \sum_{\{\mathbf{s}\}} \det(\mathbb{1} - \Sigma_C[\mathbf{s}]\Delta)}{\eta \sum_{\{\mathbf{s}\}} \det(\mathbb{1} - \Sigma_C[\mathbf{s}]\Delta)} \\ &= -i \frac{\sum_{\{\mathbf{s}\}} \det(D[\eta, \mathbf{s}]) - \sum_{\{\mathbf{s}\}} \det(D[0, \mathbf{s}])}{\eta \sum_{\{\mathbf{s}\}} \det(D[0, \mathbf{s}])}, \end{aligned} \quad (4.43)$$

with $D[\eta, \mathbf{s}] = \mathbb{1} - (\Sigma_C[\mathbf{s}] - \eta \Sigma_S)\Delta$ resulting in the following expression for the generating functional

$$Z[\eta] = \sum_{\{\mathbf{s}\}} \det(D[\eta, \mathbf{s}]). \quad (4.44)$$

The ISPI scheme is used to numerically perform the sum in this expression via an approximation of the matrix Δ .

4.3.1 Current

To find the source term of an observable we start with its operator. The current operator is given by

$$\mathcal{I}_\alpha = ie \sum_{\mathbf{k}} \left(\mathcal{C}_{\alpha\mathbf{k}}^\dagger Y_\alpha \mathcal{D} - \mathcal{D}^\dagger Y_\alpha^\dagger \mathcal{C}_{\alpha\mathbf{k}} \right), \quad (4.45)$$

as was found in Eq. (3.14). Since this operator is normal ordered, it can simply be written in terms of Grassmann fields by replacing the creation and annihilation operators with the corresponding Grassmann fields

$$I_\alpha(t_m) = ie \sum_{\mathbf{k}} \left(\bar{\Psi}_{\alpha\mathbf{k}}^\nu(t_m) Y_\alpha \Phi^{\nu'}(t_m) - \bar{\Phi}^\nu(t_m) Y_\alpha^\dagger \Psi_{\alpha\mathbf{k}}^{\nu'}(t_m) \right). \quad (4.46)$$

The question remains on which branch C_ν of the Keldysh contour the different Grassmann fields act. If we work within a fully time-discrete formulation of the path integral, it is sufficient to place above equation on the upper or lower contour (or half on it on the upper and the other half on the lower). This is, however, not the route we take in our derivation. In Sec. 4.1.3 we started out with a continuous notation, which was then discretized. Such an ansatz requires more thought for the implementation of the source term, but is not plagued by unrealistic, δ_t -dependent shifts of the observables as function of the gate voltage ε_0 .

For the current the implementation on the upper contour is still possible, but this is just a coincidence. At the latest when we want to implement the occupation number and spin projections this direct approach fails. To remain consistent we introduce the derivation for the current, and can then just follow the same steps for the other observables. We recall that, when deriving the current through the noninteracting quantum dot in Sec. 3.2, we found that the expectation value of the current is given by two lesser Green functions that are anti-Hermitian (see Eq. (3.17)). In Eq. (2.11) we have shown that lesser Green functions are in general given by

$$G_{\alpha\beta}^<(t, t') = i \left\langle c_\beta^\dagger(t', -) c_\alpha(t, +) \right\rangle. \quad (4.47)$$

When we apply this to the lesser Green functions that build the expectation value of the current we find that

$$I_\alpha(t_m) = ie \sum_{\mathbf{k}} \left(\bar{\Psi}_{\alpha\mathbf{k}}^-(t_m) Y_\alpha \Phi^+(t_m) - \bar{\Phi}^-(t_m) Y_\alpha^\dagger \Psi_{\alpha\mathbf{k}}^+(t_m) \right). \quad (4.48)$$

When making use of the anti-Hermiticity of the lesser Green function, we are able to reduce the source term to

$$I_\alpha(t_m) = 2e \operatorname{Re} \sum_{\mathbf{k}} \bar{\Psi}_{\alpha\mathbf{k}}^-(t_m) Y_\alpha \Phi^+(t_m), \quad (4.49)$$

which leads to an even more sparse source self energy.

We then include $\eta I_\alpha(t_m)$ in Eq. (4.25), where we combine the interaction part with the Green function of the free dot to form $G^{-1}[\mathbf{s}]$ as well as the terms/term from Eq. (4.48) or Eq. (4.49) with the tunneling terms. As a result we find for the generating functional

$$\begin{aligned} Z[\eta] = & \sum_{\{\mathbf{s}\}} \int \mathcal{D}[\bar{\Phi}, \Phi, \bar{\Psi}_{\alpha\mathbf{k}}, \Psi_{\alpha\mathbf{k}}] \exp \left[\sum_{\nu, \nu'=\pm} \sum_{l, l'=1}^N \left(\bar{\Phi}_l^\nu i(G^{-1}[\mathbf{s}])_{ll'}^{\nu\nu'} \Phi_{l'}^{\nu'} \right. \right. \\ & + \sum_{\alpha\mathbf{k}} \bar{\Psi}_{\alpha\mathbf{k}, l}^\nu i(g_{\alpha\mathbf{k}}^{-1})_{ll'}^{\nu\nu'} \Psi_{\alpha\mathbf{k}, l'}^{\nu'} - \bar{\Psi}_{\alpha\mathbf{k}, l}^\nu \left(i(T_\alpha)_{ll'}^{\nu\nu'} + \delta_{lm} \delta_{l'm} \delta_{\nu-} \delta_{\nu'+} e\eta Y_\alpha \right) \Phi_{l'}^{\nu'} \\ & \left. \left. - \bar{\Phi}_l^\nu \left(i(T_\alpha^\dagger)_{ll'}^{\nu\nu'} - \delta_{lm} \delta_{l'm} \delta_{\nu-} \delta_{\nu'+} e\eta Y_\alpha^\dagger \right) \Psi_{\alpha\mathbf{k}, l'}^{\nu'} \right) \right], \end{aligned} \quad (4.50)$$

where m is the time step that includes t_m . We solve the path integral as we did in Sec. 4.1.2, which reproduces the result from Eq. (4.41), where the source self energy is given by

$$\eta \Sigma_{S, ll'}^{\nu\nu'} = e\eta \left(\nu Y_\alpha^\dagger g_{lm}^{\nu-} \delta_{l'm} \delta_{\nu'+} Y_\alpha - \delta_{lm} \delta_{\nu-} Y_\alpha^\dagger g_{ml'}^{+\nu'} \nu' Y_\alpha \right) \quad (4.51)$$

Terms of order $\mathcal{O}(\eta^2)$ and higher are neglected, since η is set to zero after performing the derivative, where we used the source term from Eq. (4.48). The resulting source self energy is a matrix with only two columns and two lines being nonzero. From this equation it is clear, that this is closely related to the tunneling self energy, Eq. (4.28). In fact, we can express the current's source self energy as

$$\eta \Sigma_{S, ll'}^{\nu\nu'} = e\eta \Sigma_{T, \alpha}^{\nu\nu'} (\delta_{l'm} \delta_{\nu'+} - \delta_{lm} \delta_{\nu-}) \quad (4.52)$$

Implementing the Source term from Eq. (4.49) produces the following source self energy

$$\eta \Sigma_{S, ll'}^{\nu\nu'} = 2e\eta \nu Y_\alpha^\dagger g_{lm}^{\nu-} \delta_{l'm} \delta_{\nu'+} Y_\alpha \quad (4.53)$$

and we have to take the real part of the resulting current. This source self energy only has two lines that are nonzero, which should prove necessary when implementing the transfer-matrix method.

4.3.2 Occupation Number and Spin Projection

The source self energies for the occupation number and the different spin projections are implemented in an analogous manner as the current. However, while we mentioned that it is still possible to implement the current source term simply on the C_+ branch of the Keldysh contour, this is not the case anymore for the occupation number and spin projections. The expectation values of these observables are given by

$$\begin{aligned} \langle \mathcal{N}(t_m) \rangle &= \text{tr} (G_{\text{dot}}^<(t_m, t_m)), \\ \langle \mathcal{S}_i(t_m) \rangle &= \frac{1}{2} \text{tr} (G_{\text{dot}}^<(t_m, t_m) \sigma_i), \quad \text{with } i = x, y, z, \end{aligned} \quad (4.54)$$

with $G_{\text{dot}}^<(t_m, t_m) = [\bar{\Phi}^-(t_m)]^T \cdot [\Phi^+(t_m)]^T$. Just as for the current we include the respective source term in Eq. (4.25). This time, however, it only depends on the dot degrees of freedom and we combine it with the dot term. Since this term is not affected when the lead degrees of freedom are integrated out, the source self energy only has 2 nonvanishing elements. For the occupation number it is given by

$$(\eta\Sigma_S)_{ll'}^{\nu\nu'} = \eta\delta_{lm}\delta_{l'm}\delta_{\nu-\delta_{\nu'}+\sigma_0}. \quad (4.55)$$

The source self energies for the spin projections are given accordingly. With this the source self energies are known for the four observables, we discuss throughout this thesis. They are plugged back into Eq. (4.44), which is then the main result of this chapter. The next chapter is dedicated to performing sum over the determinant.

4.4 Summary

During this chapter, we derived the path integral formulation of the partition function to the model of the quantum-dot spin valve, that was introduced in Chap. 3. We started off with a noninteracting setup, which can be derived and solved analytically in the wide-band limit. We found that the partition function is given by the determinant of the inverse of the model's time-discrete, dressed Green function Δ^{-1} . When including onsite Coulomb interactions, one finds that the interaction Hamiltonian is quartic in the dot's degrees of freedom. As a consequence, analytically tracing out the dot's degrees of freedom is rendered impossible. A discrete Hubbard-Stratonovich transformation allows us to break through this obstacle at the cost of introducing one additional Ising-like degree of freedom per time slice. The partition function for the interacting quantum-dot spin valve, has a similar form as the noninteracting but one has to sum over all possible configurations of these Ising-like degrees of freedom. Doing this analytically proves an impossible task, and approximations are required, one of which is the ISPI technique introduced in the following chapter.

In a final step, we explained how to calculate expectation values of several observables via the path-integral method. For this the partition function is transformed into a generating functional, by introducing so-called source terms for the different observables. These source terms break time-inversion symmetry in a specific way, allowing the calculation of expectation values via derivation of the generating functional with respect to a multiplier η , added to the source term.

5 Iterative Summation of Path Integrals

Describing resonant transport through an interacting quantum-dot spin valve is a problem of exponential difficulty. This can be seen impressively in Eq. (4.44), where one has to sum over all 2^{2N} configurations of the Ising-like Hubbard-Stratonovich transformation. Since N usually has to be of the order of a few hundreds, it is clear that a brute-force approach is a hopeless task. A more sophisticated and efficient way, including controlled approximations, is necessary to perform the sum. Such a method is provided by the ISPI scheme [87, 93]. It is a complete deterministic approach, based on the iterative evaluation of sums over determinants as they appear in Eq. (4.44). The ISPI technique relies on the fact that lead-induced correlations decrease exponentially with increasing time. This allows us to reduce the number of summations from 2^{2N} to $(N/K)2^{2K}$, where K is the number of Trotter slices (of size δ_t) over which correlations are taken into account. This is usually a huge reduction of complexity since – as we mentioned before – N is of the order of a few hundreds while K can be chosen to be 6 or 7. We remark that a similar formulation in terms of the reduced density matrix of the system has been presented in Ref. [94].

In Fig. 5.1 we demonstrate how the dot's Green function decays with time by showing the absolute value of Δ as a function of $t - t' = (l - l')\delta_t$ in the continuum limit, $\delta_t \rightarrow 0$ in a semilogarithmic plot. In panels (a) and (b) we demonstrate how different values of the bias voltage affect the time-dependence of the Green function at high ($k_B T = \Gamma$) and low ($k_B T = 0.1\Gamma$) temperature, respectively. We show the impact of a magnetic field in x -direction in panel (c) and of the gate voltage in panel (d). We find that low temperatures make the Green function decay slower, and both the bias voltage and the magnetic field may lead to oscillations in the time-dependence but neither alter the exponential decrease. Increasing the gate voltage suppresses the Green function and introduces small, fast oscillations that are only visible at large times. All this is consistent with the findings in Refs. [87, 88, 93]. In total, we have an exponential decrease of the lead-induced correlations with increasing times, which becomes apparent e.g. from Eq. (D.4). The system parameters only introduce oscillations or change the slope of the decrease. This motivates us to neglect all contributions from time differences $t - t'$ larger than a chosen timescale t_K . In the discretized version this amounts to setting all matrix elements $\Delta_{ll'}$ of the dressed Green function with $|l - l'|\delta_t > t_K$ to 0. Therefore, lead-induced correlations are only included over a span of K Trotter slices, where $K = t_K/\delta_t$. We call t_K the memory or correlation time.

The truncation after K Trotter slices makes the matrix $D[\eta, \mathbf{s}]$ block tridiagonal.

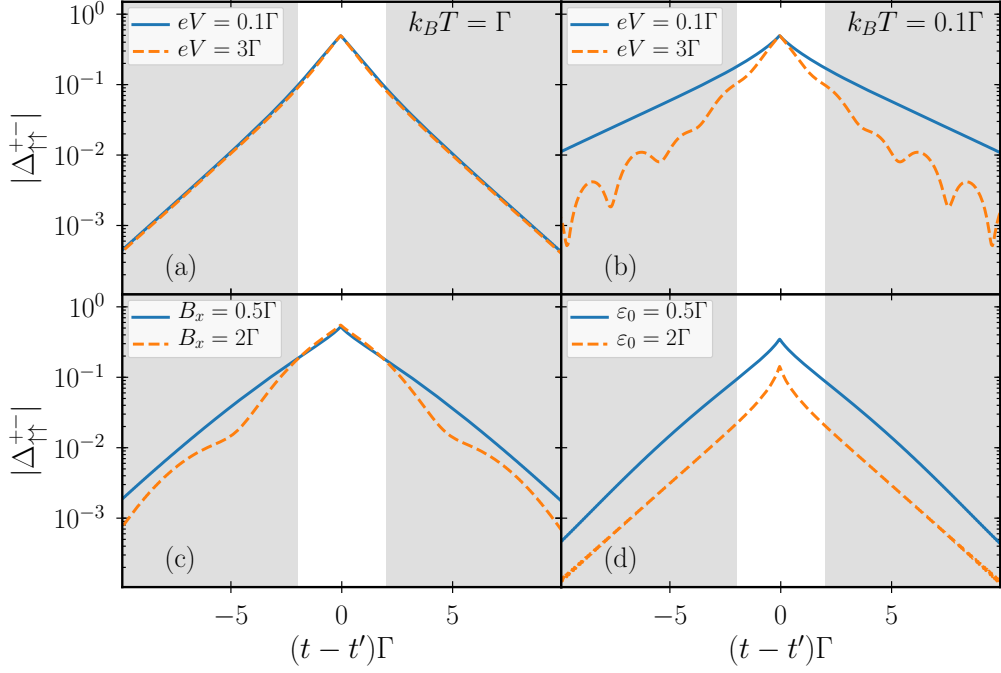


Figure 5.1: Semilogarithmic plots of the absolute value of the Green function Δ as a function of time for different setups of the system parameters. (a) Different values of the bias voltage at large temperatures $k_B T = \Gamma$. (b) Different values of the bias voltage at low temperatures $k_B T = 0.1\Gamma$. For panels (a,b) the other parameters are given by $\varepsilon_0 = 0$, $\mathbf{B} = 0$, $p = 0.5$, $\theta = \pi/2$. (c) Impact of a magnetic field in x -direction. Other parameters are $k_B T = 0.2\Gamma$, $\varepsilon_0 = 0$, $eV = 0.1\Gamma$, $p = 0.5$, $\theta = \pi/2$. (d) Impact of the gate voltage with the other parameters at $k_B T = 0.2\Gamma$, $eV = 0.1\Gamma$, $\mathbf{B} = 0$, $p = 0.5$, $\theta = \pi/2$. Shaded areas demonstrate the truncation necessary for ISPI at correlation time $\Gamma t_K = 2$.

It can, then, be written in the form

$$D[\eta, \mathbf{s}] \approx \begin{pmatrix} D_{11} & D_{12} & 0 & 0 & \cdots & 0 \\ D_{21} & D_{22} & D_{23} & 0 & \cdots & 0 \\ 0 & D_{32} & D_{33} & D_{34} & \cdots & 0 \\ 0 & 0 & D_{43} & D_{44} & \cdots & 0 \\ \vdots & \vdots & \vdots & \vdots & \ddots & \vdots \\ 0 & 0 & 0 & 0 & \cdots & D_{N_K N_K} \end{pmatrix}. \quad (5.1)$$

The total $4N \times 4N$ matrix is decomposed into blocks $D_{nn'}$ of size $4K \times 4K$. The index n runs from 1 to $N_K = N/K$, and only blocks $D_{nn'}$ with $|n - n'| \leq 1$ have finite entries. Since $\Sigma_C(\mathbf{s})$ is a diagonal matrix, the definition of $D[\eta, \mathbf{s}]$ in Eq. (4.44) yields that the blocks $D_{nn'}$ in the n -th row depend only on the set of $2K$ Hubbard-Stratonovich spins from the Trotter slices $(n - 1)K + 1$ to nK but not on spins

from Trotter slices outside of this range. We define these sets of $2K$ spins by $\mathbf{s}_n \equiv (s_{(n-1)K+1}^+, s_{(n-1)K+1}^-, \dots, s_{nK}^+, s_{nK}^-)$.

5.1 Finite-Time Implementation

If we use the approximation from Eq. (5.1) and apply it to Eq. (4.44), we have to evaluate $\det D[\eta, \mathbf{s}]$ for all configurations of Hubbard-Stratonovich spins. The determinant of a block tridiagonal matrix can be analyzed in an iterative fashion [87, 93, 112]. For this we iteratively make use of Schur's formula

$$\det \begin{pmatrix} a & b \\ c & d \end{pmatrix} = \det a \cdot \det(d - ca^{-1}b), \quad (5.2)$$

where a, b, c, d could be, again, matrices. In the first step, we apply Schur's formula to the matrix $D[\eta, \mathbf{s}]$, such that $a = D_{11}$, while $b = (D_{12}, 0, 0, \dots, 0)$ and $c = (D_{21}, 0, 0, \dots, 0)^T$ and d is the remaining, quadratic part of the matrix $D[\eta, \mathbf{s}]$, with D_{22} in its upper left corner and $D_{N_K N_K}$ in its lower right corner. To calculate the determinant of $4(N-K) \times 4(N-K)$ matrix $d - ca^{-1}b$, we again use Schur's formula with the new a taken as the upper left $4K \times 4K$ block and, b, c, d defined in an analogue manner to the first step. This procedure is repeated until we arrive at the lower right corner. The result is [112]

$$Z[\eta] = \sum_{\{\mathbf{s}\}} \det D_{11} \cdot \det \check{D}_{22} \cdot \dots \cdot \det \check{D}_{N_K N_K} \quad (5.3)$$

where \check{D}_{nn} is defined iteratively by

$$\check{D}_{nn}[\mathbf{s}_n, \dots, \mathbf{s}_1] = D_{nn}[\mathbf{s}_n] - D_{n,n-1}[\mathbf{s}_n] (\check{D}_{n-1,n-1}[\mathbf{s}_{n-1}, \dots, \mathbf{s}_1])^{-1} D_{n-1,n}[\mathbf{s}_{n-1}], \quad (5.4)$$

together with $\check{D}_{11} = D_{11}$. Due to this iterative definition, \check{D}_{nn} depends on all the blocks $D_{\bar{n}\bar{n}'}$ of Eq. (5.1) that are placed above of D_{nn} , i.e. $\bar{n}, \bar{n}' \leq n$. This is, however, inconsistent with our decision to neglect all correlations beyond t_K . Since D was approximated as being block tridiagonal, we should consistently eliminate the influence of $D_{\bar{n}\bar{n}'}$ on \check{D}_{nn} when \bar{n}, \bar{n}' deviates from n by more than 1.

To do this in a controlled manner, we neglect terms of the style

$$D_{n,n-1} [D_{n-1,n-1}]^{-1} D_{n-1,n-2} [D_{n-2,n-2}]^{-1} D_{n-2,n-1} [D_{n-1,n-1}]^{-1} D_{n-1,n} \quad (5.5)$$

whenever they appear during the iteration. This is necessary, since these terms couple the Hubbard-Stratonovich spin sets \mathbf{s}_n and \mathbf{s}_{n-2} , which is inconsistent with our approximation. For example, in the third iteration step we approximate as follows

$$\begin{aligned} \det(\check{D}_{33}) &= \det(D_{33} - D_{32} [D_{22}]^{-1} D_{23} + D_{32} [D_{22}]^{-1} D_{21} [D_{11}]^{-1} D_{12} [D_{22}]^{-1} D_{23}) \\ &\approx \det(D_{33} - D_{32} [D_{22}]^{-1} D_{23}). \end{aligned} \quad (5.6)$$

The fourth step then builds upon this approximation and is itself approximated in the same way and so on. For the sake of clarity, we write out the iteration procedure. Necessary steps for a consistent approximation have already been implemented, leaving us to find the following expression

$$Z[\eta] = \sum_{\{\mathbf{s}\}} \det(D_{11}) \det(D_{22} - D_{21} [D_{11}]^{-1} D_{12}) \det(D_{33} - D_{32} [D_{22}]^{-1} D_{23}) \cdots \\ \times \det(D_{N_K, N_K} - D_{N_K, N_K-1} [D_{N_K-1, N_K-1}]^{-1} D_{N_K-1, N_K}). \quad (5.7)$$

The result is a rather compact approximation procedure, which we can write as follows: In Eq. (5.3) we replace each \check{D}_{nn} with

$$\check{D}_{nn}[\mathbf{s}_n, \mathbf{s}_{n-1}] = D_{nn}[\mathbf{s}_n] - D_{n, n-1}[\mathbf{s}_n] (D_{n-1, n-1}[\mathbf{s}_{n-1}])^{-1} D_{n-1, n}[\mathbf{s}_{n-1}], \quad (5.8)$$

with $\check{D}_{11} = D_{11}$, i.e., in comparison to Eq. (5.4) we have replaced

$$(\check{D}_{n-1, n-1}[\mathbf{s}_{n-1}, \dots, \mathbf{s}_1])^{-1} \rightarrow (D_{n-1, n-1}[\mathbf{s}_{n-1}])^{-1} \quad (5.9)$$

on the right hand side. This automatically leads to a consistent approximation, for which \check{D}_{nn} and, therefore, also its determinant $\det \check{D}_{nn}$ depends only on two sets of Hubbard Stratonovich spins, namely \mathbf{s}_n and \mathbf{s}_{n-1} from the Trotter slices $(n-2)K+1, \dots, nK$ but not from earlier or later ones. This allows us to reorder the different determinants, and we are thus able to evaluate the sum over all Hubbard-Stratonovich spins in a piecewise manner

$$Z[\eta] = \sum_{\{\mathbf{s}_{N_K}, \mathbf{s}_{N_K-1}\}} \det(\check{D}_{N_K N_K}[\mathbf{s}_{N_K}, \mathbf{s}_{N_K-1}]) \cdots \sum_{\{\mathbf{s}_2\}} \det(\check{D}_{33}[\mathbf{s}_3, \mathbf{s}_2]) \\ \times \sum_{\{\mathbf{s}_1\}} \det(\check{D}_{22}[\mathbf{s}_2, \mathbf{s}_1]) \det(D_{11}[\mathbf{s}_1]). \quad (5.10)$$

Each of the sums in Eq. (5.10) runs over 2^{2K} different spin configurations. This is what we refer to as the *finite-time implementation* of the ISPI technique, which has been used in previous works. It has proven to be a powerful tool when working with systems in the regime where all energy scales are of the same order of magnitude [88, 93]. In total, there are $N_K 2^{2K}$ summations instead of the summation over the 2^{2N} configurations of the Hubbard-Stratonovich spins in Eq. (4.44), without the truncation scheme. A more precise estimate of the scaling behavior of the numerical effort should take into account the effort for building \check{D}_{nn} from Eq. (5.8). An in-depth investigation of the performance of the ISPI code is given in Sec. 5.4.

5.2 Transfer-Matrix Implementation

In the last section we introduced the finite-time implementation of the ISPI technique. We are, however, able to take Eq. (5.10) as a basis and further develop the

method. The shape of Eq. (5.10) suggests to rewrite it into the product of matrices and a vector in the space of Hubbard-Stratonovich spin configurations. For this we arrange the 2^{4K} different values of $\det \tilde{D}_{nn}[\mathbf{s}_n, \mathbf{s}_{n-1}]$ for the different Hubbard-Stratonovich spin configurations in a $2^{2K} \times 2^{2K}$ matrix, which we call the *transfer matrix*.

$$\Lambda_{n,n-1} = \left(\det \tilde{D}_{nn}[\mathbf{s}_n, \mathbf{s}_{n-1}] \right) \quad (5.11)$$

where each row corresponds to one of the 2^{2K} configurations for \mathbf{s}_n and each column to one of the 2^{2K} configurations for \mathbf{s}_{n-1} . These transfer matrices are, one after another, multiplied with a vector of dimensionality 2^{2K} , where the starting vector is given by

$$|\Lambda_1\rangle = (\det D_{11}[\mathbf{s}_1]). \quad (5.12)$$

The Keldysh generating functional can, then, be written as a product

$$Z[\eta] = \langle 1 | \Lambda_{N_K, N_K-1} \cdots \Lambda_{3,2} \Lambda_{2,1} | \Lambda_1 \rangle \quad (5.13)$$

of the transfer matrices, where $\Lambda_{n,n-1}$ is a $2^{2K} \times 2^{2K}$ matrix for $n \geq 2$, $|\Lambda_1\rangle$ is a 2^{2K} dimensional column vector, and $\langle 1 | = (1, \dots, 1)$ a 2^{2K} dimensional row vector. The latter is necessary to account for the final spin sum $\sum_{\{\mathbf{s}_{N_K}\}}$ in Eq. (5.10). Each of the N_K matrix multiplications requires a summation over 2^{2K} Hubbard-Stratonovich spin configurations.

The term *transfer matrix* is known from statistical physics, where the transfer-matrix method has proven to be a powerful tool. The method was first introduced by Kramers and Wannier to solve the 1-dimensional Ising model [113, 114]. A few years later it was then used by Onsager as the basis for his well-known exact solution of the 2-dimensional Ising model [115]. The transfer-matrix method in statistical physics allows to calculate the partition function of e.g. the 1 or 2 dimensional Ising model by calculating the largest eigenvalue and its eigenvector of some matrix, that is called the transfer matrix. It is, however, not limited to these models but is a far more general approach. We choose this name consciously since Eq. (5.13) is the starting point for a mapping of the ISPI scheme to the transfer-matrix method. The final result is then the *transfer-matrix implementation* of the ISPI technique.

To transform the ISPI technique into a transfer-matrix method we return to Eq. (5.13) where we set $\eta \rightarrow 0$ for a moment, thus neglecting the source term. As a consequence, we restore time-translation symmetry, Eq. (4.4), and the diagonal blocks of the matrix $D[\eta, \mathbf{s}]$, Eq. (5.1), are all the same $4K \times 4K$ matrices, meaning $D_{nn} = D_{n+1n+1}$. This is equally true all blocks above the diagonal as well as all blocks below the diagonal, respectively. Hence, it is clear that the different transfer matrices $\Lambda_{n,n'}$ are all equal, too, as long as the source term is not implemented. This allows us to set $\Lambda_{n,n'} = \Lambda$ and write

$$Z[0] = \langle 1 | \Lambda \Lambda \cdots \Lambda \Lambda | \Lambda_1 \rangle = \langle 1 | \Lambda^{N_K} | \Lambda_1 \rangle. \quad (5.14)$$

From Eqs. (4.44) and (4.55) it is clear that the source self energy of either the occupation number or the components of the spin projection affects one line in the

block matrix of $4K \times 4K$ matrices D_{nn} , Eq. (5.1). The current's source self energy, Eq. (4.52), is more complicated. However, employing the reduced version of the source self energy, Eq. (4.53), it is still possible to calculate currents within the transfer-matrix approach. Still, in this section we focus on the occupation number and spin projections as observables. In what follows, we refer to elements in the line that is affected by the source term as $D_{mm}[\eta]$, with $n = 1, \dots, N_K$. Thus, the matrix $D[\eta, \mathbf{s}]$ in the proximity of D_{mm} takes the form

$$D[\eta, \mathbf{s}] = \begin{pmatrix} D_{11} & \cdots & 0 & 0 & 0 & 0 & \cdots & 0 \\ \vdots & \ddots & \vdots & \vdots & \vdots & \vdots & \ddots & \vdots \\ 0 & \cdots & D_{m-2m-2} & D_{m-2m-1} & 0 & 0 & \cdots & 0 \\ 0 & \cdots & D_{m-1m-2} & D_{m-1m-1} & D_{m-1m} & 0 & \cdots & 0 \\ 0 & \cdots & 0 & D_{mm-1}[\eta] & D_{mm}[\eta] & D_{mm+1}[\eta] & \cdots & 0 \\ 0 & \cdots & 0 & 0 & D_{m+1m} & D_{m+1m+1} & \cdots & 0 \\ \vdots & \ddots & \vdots & \vdots & \vdots & \vdots & \ddots & \vdots \\ 0 & \cdots & 0 & 0 & 0 & 0 & \cdots & D_{N_K N_K} \end{pmatrix}, \quad (5.15)$$

The boxes denote the elements included in the transfer matrices $\Lambda_{m-1, m-2}$ (red), $\Lambda_{m, m-1}[\eta]$ (black) and $\Lambda_{m+1, m}[\eta]$ (blue). It is obvious that two of the transfer matrices are affected by the source self energy, while all other transfer matrices still fulfill $\Lambda_{n, n'} = \Lambda$, for $n, n' \neq m$.

To account for the inclusion of the source term, we have to modify Eq. (5.14), which leads to the following formula for the generating functional including the source term

$$\begin{aligned} Z[\eta] &= \langle 1 | \Lambda \Lambda \cdots \Lambda \Lambda_{m+1, m}[\eta] \Lambda_{m, m-1}[\eta] \Lambda \cdots \Lambda \Lambda | \Lambda_1 \rangle \\ &= \langle 1 | \Lambda^{N_K/2-1} \Lambda_{m+1, m}[\eta] \Lambda_{m, m-1}[\eta] \Lambda^{N_K/2-1} | \Lambda_1 \rangle. \end{aligned} \quad (5.16)$$

To evaluate $\Lambda^{N_K/2-1}$ we recall that we are interested in the long-term limit, which is reached once $N_K \rightarrow \infty$. When decomposing the transfer matrix in terms of its eigenvectors we find

$$\lim_{L \rightarrow \infty} \Lambda^L = \lim_{L \rightarrow \infty} \sum_{\mu} \lambda_{\mu}^L |\lambda_{\mu}\rangle \langle \lambda_{\mu}| \approx \lambda_0^L |\lambda_0\rangle \langle \lambda_0|, \quad (5.17)$$

where λ_{μ} are the eigenvalues of the transfer matrix Λ with $|\lambda_0| > |\lambda_1| > \dots$, and $|\lambda_0| > 1$. With $|\lambda_{\mu}\rangle$ we denote the eigenvectors corresponding to the eigenvalue λ_{μ} . Plugging this back into Eq. (5.16), we find

$$Z[\eta] = \lambda_0^{N_K-2} \langle 1 | \lambda_0 \rangle \langle \lambda_0 | \Lambda_{m+1, m}[\eta] \Lambda_{m, m-1}[\eta] | \lambda_0 \rangle \langle \lambda_0 | \Lambda_1 \rangle. \quad (5.18)$$

When calculating expectation values by using this generating functional in Eq. (4.43), constant factors cancel and we find

$$\langle \mathcal{O} \rangle = -\frac{i}{\eta} \left(\frac{\langle \lambda_0 | \Lambda_{m+1, m}[\eta] \Lambda_{m, m-1}[\eta] | \lambda_0 \rangle}{\lambda_0^2} - 1 \right). \quad (5.19)$$

Thus we reduced the number of transfer matrices we need to evaluate from N_K in the ISPI case to 3: Λ , $\Lambda_{m+1,m}[\eta]$ and $\Lambda_{m,m-1}[\eta]$, which decreases computation times, as we show in Sec. 5.4. There, we also discuss in detail how the transfer-matrix approach compares in detail with the usual ISPI technique. We are able to advance the transfer matrix approach further since it allows to analytically calculate the derivative with respect to η , which is necessary to calculate expectation values, Eq. (4.40). For this we first symmetrize Eq. (5.16), and then demonstrate step by step how to perform the derivative $\frac{\delta}{\delta\eta}Z[\eta]|_{\eta=0}$.

5.2.1 Symmetrization

To symmetrize Eq. (5.16), we recall the derivation of this formula by iteratively applying Schur's formula, Eq. (5.2), to the truncated matrix D , Eq. (5.1). During this derivation we introduced the matrix \tilde{D}_{nn} , whose determinant provides the elements of the transfer matrix $\Lambda_{n,n'}$. Using Schur's formula, we are able to rewrite the determinant of \tilde{D}_{nn} , leading to

$$\begin{aligned} \det(\tilde{D}_{nn}) &= \begin{vmatrix} D_{n-1,n-1} & D_{n-1,n} \\ D_{n,n-1} & D_{n,n} \end{vmatrix} |D_{n-1,n-1}|^{-1} \\ &= \det(\bar{D}_{n,n-1}) \det(D_{n-1,n-1})^{-1}, \end{aligned} \quad (5.20)$$

where we defined $\bar{D}_{n,n-1}$ as the 2×2 block matrix with $D_{n-1,n-1}$ in its upper left corner and $D_{n,n}$ in its lower right corner. This matrix depends, similarly to \tilde{D}_{nn} on two sets of Hubbard-Stratonovich spins, \mathbf{s}_{n-1} and \mathbf{s}_n . On the other hand, the matrix in the second determinant on the right-hand side of Eq. (5.20) only depends on \mathbf{s}_{n-1} . This representation of $\det(\tilde{D}_{nn})$ allows us to give a different formulation of the generating functional, by plugging it back into Eq. (5.10)

$$\begin{aligned} Z[\eta] &= \sum_{\{\mathbf{s}_{N_K}\}} \sum_{\{\mathbf{s}_{N_K-1}\}} \det(\bar{D}_{N_K,N_K-1}[\mathbf{s}_{N_K}, \mathbf{s}_{N_K-1}]) \det(D_{N_K-1,N_K-1}[\mathbf{s}_{N_K-1}])^{-1} \cdots \\ &\quad \times \sum_{\{\mathbf{s}_2\}} \det(\bar{D}_{3,2}[\mathbf{s}_3, \mathbf{s}_2]) \det(D_{2,2}[\mathbf{s}_2])^{-1} \sum_{\{\mathbf{s}_1\}} \det(\bar{D}_{2,1}[\mathbf{s}_2, \mathbf{s}_1]). \end{aligned}$$

From this equation, we are able to define two transfer matrices, $U_{n,n-1}$ and V_n , similarly to how we defined the transfer matrix $\Lambda_{n,n'}$ in Eq. (5.11).

$$U_{n,n-1} = (\det \bar{D}_{n,n-1}[\mathbf{s}_n, \mathbf{s}_{n-1}]) \quad (5.21)$$

$$V_n = (\det D_{n,n}[\mathbf{s}_n]), \quad (5.22)$$

where, again, each row corresponds to one of the 2^{2K} configurations of \mathbf{s}_n , and each column to one of the 2^{2K} configurations for \mathbf{s}_{n-1} . As a result, the transfer matrix $U_{n,n-1}$ is a fully occupied $2^{2K} \times 2^{2K}$ matrix in the space of Hubbard-Stratonovich spin configurations, while V_n is a diagonal matrix in that same space. We note that

from Eq. (5.20) it follows directly that $\Lambda_{n,n-1} = U_{n,n-1}V_{n-1}^{-1}$. With this we are able to give a symmetrized version for the generating functional

$$Z[\eta] = \langle 1 | U_{N_K, N_K-1} V_{N_K-1}^{-1} \cdots U_{m+1, m}[\eta] V_m^{-1}[\eta] U_{m, m-1}[\eta] V_{m-1}^{-1} \cdots U_{2, 1} | 1 \rangle. \quad (5.23)$$

Applying Eq. (5.17) and the long-term limit $N_K \rightarrow \infty$, we are able to write this as

$$Z[\eta] = \lambda_0^{N_K-2} \langle 1 | \lambda_0 \rangle \langle \lambda_0 | U_{m+1, m}[\eta] V_m^{-1}[\eta] U_{m, m-1}[\eta] V_{m-1}^{-1} | \lambda_0 \rangle \langle \lambda_0 | 1 \rangle. \quad (5.24)$$

We emphasize that in this symmetrized version two fully occupied and one diagonal transfer matrix are affected by the source self energy. However, it allows us to analytically calculate the derivative $\frac{\delta}{\delta\eta} Z[\eta]|_{\eta=0}$, which we demonstrate in the following section.

5.2.2 Analytic Derivatives

To calculate expectation values of observables we use Eq. (4.40), which requires us to calculate $\frac{\delta}{\delta\eta} \log Z[\eta]|_{\eta=0} = Z[0]^{-1} \frac{\delta}{\delta\eta} Z[\eta]|_{\eta=0}$. For this we use Eq. (5.24) and the product rule, which leads us to the following expression

$$\begin{aligned} Z[0]^{-1} \frac{\delta}{\delta\eta} Z[\eta]|_{\eta=0} &= \lambda_0^{-2} \langle \lambda_0 | \left[\left(\frac{\delta}{\delta\eta} U_{m+1, m}[\eta] \right) V_m^{-1}[0] U_{m, m-1}[0] \right. \\ &\quad \left. + U_{m+1, m}[0] \left(\frac{\delta}{\delta\eta} V_m^{-1}[\eta] \right) U_{m, m-1}[0] \right. \\ &\quad \left. + U_{m+1, m}[0] V_m^{-1}[0] \left(\frac{\delta}{\delta\eta} U_{m, m-1}[\eta] \right) \right] V_{m-1}^{-1} | \lambda_0 \rangle. \end{aligned} \quad (5.25)$$

These three parts can be solved one by one, which we do in what follows. For these calculations we use the notation $\bar{A}_{n,n-1}$, which denotes a part of a $N_K \times N_K$ block matrix A with $4K \times 4K$ blocks, that is defined similarly to $\bar{D}_{n,n-1}$ in Eq. (5.20).

We start with the derivation of $\frac{\delta}{\delta\eta} U_{m+1, m}[\eta]$. The derivative acts on the elements of the transfer matrix, which themselves are given by the determinant of $\bar{D}_{m+1, m}$ with different configuration of the spins \mathbf{s}_{m+1} and \mathbf{s}_m . Therefore, we make use of the identity $\partial \det(A) = \det(A) \text{tr}(A^{-1} \partial A)$ [116], and use the definition $\bar{D}_{m+1, m}[\eta = 0] = \bar{D}_{2, 1}[\eta = 0] = \bar{D}_0$. We find

$$\begin{aligned} \frac{\delta}{\delta\eta} \det(\bar{D}_{m+1, m}[\eta]) &= \det(\bar{D}_0) \text{tr} \left(\bar{D}_0^{-1} \frac{\delta}{\delta\eta} \bar{D}_{m+1, m}[\eta] \right) \\ &= \det(\bar{D}_0) \text{tr} \left(\bar{D}_0^{-1} \frac{\delta}{\delta\eta} (\bar{D}_0 + \eta \bar{\Sigma}_{S, m+1, m} \bar{\Delta}_{m+1, m}) \right) \\ &= \det(\bar{D}_0) \text{tr} (\bar{D}_0^{-1} \bar{\Sigma}_{S, m+1, m} \bar{\Delta}_{m+1, m}), \end{aligned} \quad (5.26)$$

where in the second step we made use of the definition of $D[\eta, \mathbf{s}]$, Eq (4.44), and introduced the matrices $\bar{\Sigma}_S$ and $\bar{\Delta}$, which are also submatrices of Σ_S and Δ . $\bar{\Sigma}_S$ for the

occupation number as well as spin projection is given by $\bar{\Sigma}_{S,m+1,m} = \begin{pmatrix} \Sigma_{S,mm} & 0 \\ 0 & 0 \end{pmatrix}$, where $\Sigma_{S,mm}$ is a $4K \times 4K$ matrix with only two nonzero elements, see Eq. (4.55). It is useful to express Δ in terms of D_0 . Since $D_0 = \mathbb{1} - \Sigma_C \Delta$, we find $\Delta = \Sigma_C^{-1}(\mathbb{1} - D_0)$, where it is assumed that the Coulomb interaction $U \neq 0$. Plugging this back into Eq. (5.26) we find

$$\begin{aligned} \frac{\delta}{\delta\eta} \det(\bar{D}_{m+1,m}[\eta]) &= \det(\bar{D}_0) \operatorname{tr}(\bar{D}_0^{-1} \bar{\Sigma}_{S,m+1,m} \bar{\Sigma}_{C,m+1,m}^{-1} (\mathbb{1} - \bar{D}_0)) \\ &= \det(\bar{D}_0) \operatorname{tr}(\bar{D}_0^{-1} \bar{\Sigma}_{S,m+1,m} \bar{\Sigma}_{C,m+1,m}^{-1} - \bar{\Sigma}_{S,m+1,m} \bar{\Sigma}_{C,m+1,m}^{-1}) \\ &= \det(\bar{D}_0) \operatorname{tr}(\bar{D}_0^{-1} \bar{\Sigma}_{S,m+1,m} \bar{\Sigma}_{C,m+1,m}^{-1}), \end{aligned} \quad (5.27)$$

where we used that $\operatorname{tr}(\bar{\Sigma}_S \bar{\Sigma}_C^{-1}) = 0$. Due to the sparseness of $\bar{\Sigma}_S$ and $\bar{\Sigma}_C^{-1}$, we are able to reduce above expression, leaving us with the final result

$$\frac{\delta}{\delta\eta} U_{m+1,m}[\eta] = \det(\bar{D}_0) \operatorname{tr}((\bar{D}_0^{-1})_{11} \Sigma_{S,mm} (\Sigma_C^{-1})_{11}) \quad (5.28)$$

The calculation for $\frac{\delta}{\delta\eta} U_{m,m-1}[\eta]$ is completely analogue, and we find

$$\frac{\delta}{\delta\eta} U_{m,m-1}[\eta] = \det(\bar{D}_0) \operatorname{tr}((\bar{D}_0^{-1})_{22} \Sigma_{S,mm} (\Sigma_C^{-1})_{22}) \quad (5.29)$$

To derive $\frac{\delta}{\delta\eta} V_m^{-1}[\eta]$, we proceed similarly to the case of the other transfer matrix $U_{m+1,m}$. The derivative acts on the elements of the transfer matrix, and since it is diagonal we find

$$\frac{\delta}{\delta\eta} \det(D_{mm})^{-1} = \frac{\delta}{\delta\eta} \det(D_{mm}^{-1}) = \det(D_{0,11}^{-1}) \operatorname{tr}\left(D_{0,11} \frac{\delta}{\delta\eta} D_{mm}^{-1}\right), \quad (5.30)$$

where we note that the matrices are only one $4K \times 4K$ block and we again made use of time-translation invariance $D_{mm}[\eta = 0] = D_{0,11}$. Applying the chain rule, we find

$$\begin{aligned} \frac{\delta}{\delta\eta} \det(D_{mm})^{-1} &= \det(D_{0,11}^{-1}) \operatorname{tr}\left(D_{0,11} (-1) D_{0,11}^{-2} \frac{\delta}{\delta\eta} D_{mm}\right) \\ &= -\det(D_{0,11}^{-1}) \operatorname{tr}\left(D_{0,11}^{-1} \frac{\delta}{\delta\eta} D_{mm}\right). \end{aligned} \quad (5.31)$$

The trace is similar to the one from the derivative of $U_{m+1,m}$, and is evaluated accordingly, leading to the following result

$$\frac{\delta}{\delta\eta} V_m[\eta] = -\det(D_{0,11}^{-1}) \operatorname{tr}((D_{0,11})^{-1} \Sigma_{S,mm} (\Sigma_{C,11})^{-1}) \quad (5.32)$$

We note that for the derivative of $U_{m+1,m}$ one calculates the of inverse of \bar{D}_0 and then takes the upper left element, while for the derivative of V_m one first takes the upper left element and then calculates the inverse of this $4K \times 4K$ matrix.

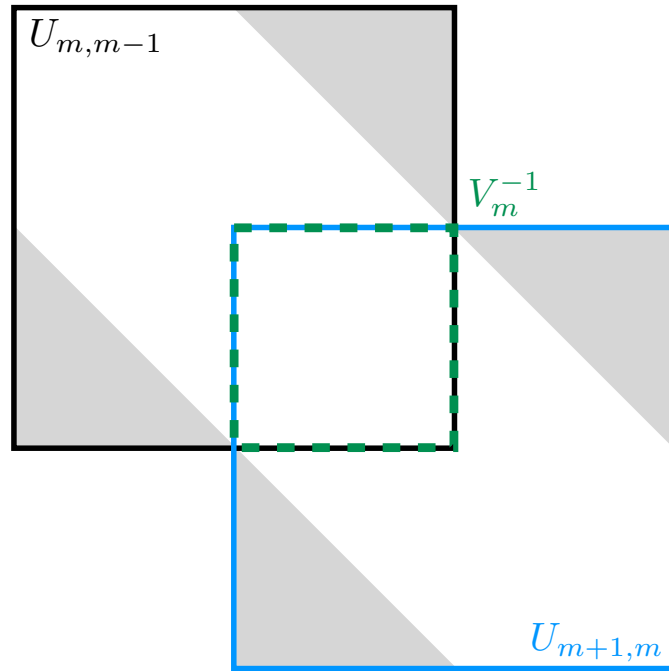


Figure 5.2: Zoomed in version of the black and blue box of Eq. (5.15). The elements of the truncated Green function $D[\eta, \mathbf{s}]$ that are required to build the three transfer matrices are shown by three squares, black contains the elements for $U_{m,m-1}$, blue the elements for $U_{m+1,m}$ and in the dashed green square contains the elements necessary to build V_m^{-1} . In areas that are shaded grey the elements are zero due to the truncation.

Plugging Eqs. (5.28), (5.29) and (5.32) back into Eq. (5.25) allows for an analytic expression of the derivative of the generating functional. When inspecting these three expressions of the derivations of the three transfer matrices closely, it is striking that they all have the same structure. If we recall that the Green function is symmetric under time translation, one might assume that they are all equal, except that $\frac{\delta}{\delta\eta} V[\eta]$ has opposite sign. This would, of course, be very beneficial, since then it would be sufficient to evaluate the diagonal transfer matrix V_m to calculate an expectation value. In Fig. 5.2 we show a sketch of the elements that contribute to the three different transfer matrices affected by the source self energy. The black and blue box represent the elements included by $U_{m,m-1}$ and $U_{m+1,m}$ respectively. The remaining central box denotes the elements included in V_m . As a consequence, Eq. (5.23), can be interpreted such that each U transfer matrix propagates the system two steps forward, while each V^{-1} transfer matrix propagates the system one step back, leading to a pilgrim step-like procedure. If we assume that the source term is located at the center of the green box in the middle, the three transfer matri-

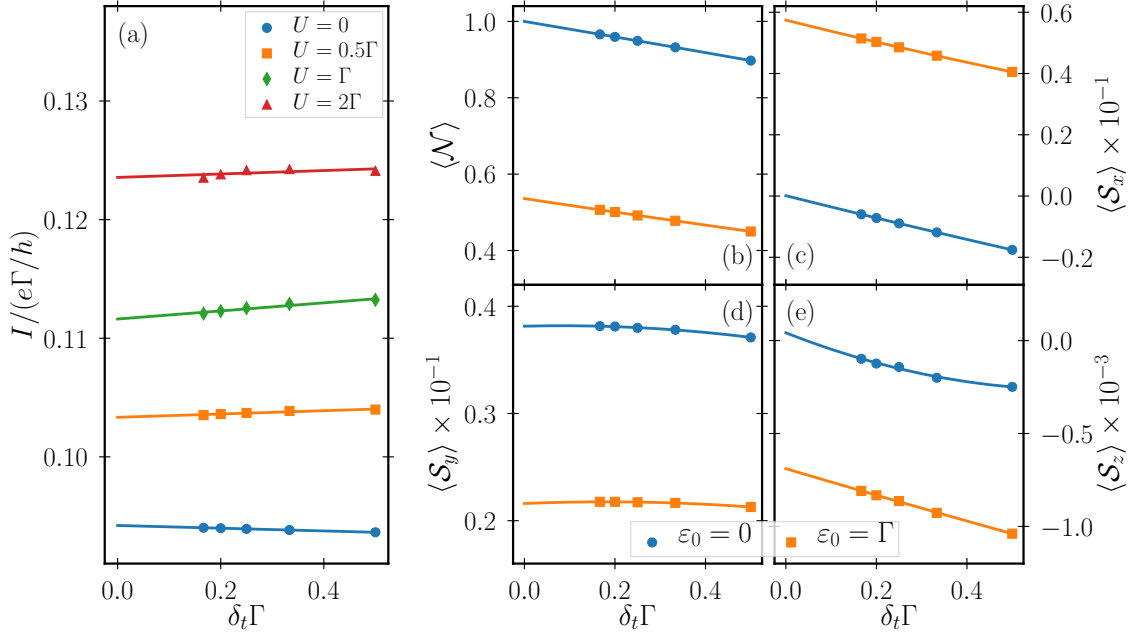


Figure 5.3: The regression in the Trotter step size δ_t for the current (a), as well as the occupation number and spin expectation values (b-e). For the current we show different Coulomb interaction strengths, while for the other observables two different values of the gate voltage ε_0 are depicted. For the current the parameters are chosen as $k_B T = 0.2\Gamma$, $\varepsilon_0 = \Gamma$, $eV = 0.1\Gamma$, $\mathbf{B} = 0$, $p = 0.5$, $\theta = 0$ and $\Gamma t_K = 1$, while for the other observables we show the case $k_B T = 0.2\Gamma$, $U = 0.5\Gamma$, $eV = 0.1\Gamma$, $B_y = 0.2\Gamma$, $p = 0.5$, $\theta = \pi/2$ and $\Gamma t_K = 1$.

ces still include different elements. As a result, the three contributions in Eq. (5.25) are not all equal apart from a minus sign, but instead have different values, that should converge for large K . For the values of K we are working with here, however, this is only an approximation, which we do not implement. Instead, we work with the results obtained from Eq. (5.25).

5.3 Convergence

When applying the ISPI scheme, two systematic errors are accumulated. For the discrete Hubbard-Stratonovich transformation, Eq. (4.35), finite discretization time steps δ_t are necessary. This time-discretization introduces a finite Trotter error for the calculation of the path integral along the Keldysh contour [111, 117], which scales with polynomially with δ_t for $\delta_t \rightarrow 0$, with the order of the polynomial depending on the observable of interest. A second source of systematic error comes from truncating correlations beyond t_K to enable us to solve the spin sum from Eq. (4.37). To reduce both errors and estimate the remaining error bars, we perform a convergence

procedure. We describe the general process here and discuss the peculiarities the different observables impose.

(i) Trotter error To eliminate the Trotter error, we first choose a finite correlation time t_K . For this t_K , the observable is calculated for different values of the discretization length δ_t . The result is a set of different realizations for every observable $\mathcal{O}(t_K, \delta_t(K))$ for discretization lengths $\delta_t(K) = t_K/K$ with $K = 2, \dots, 7$. We then perform the well-established extrapolation [117, 118] to the continuum limit, $\delta_t \rightarrow 0$. Since the actual δ_t -dependence varies strongly depending on the observable \mathcal{O} under discussion, we fit against the polynomial expression

$$\mathcal{O}(t_K, \delta_t \rightarrow 0) = \lim_{\delta_t \rightarrow 0} \sum_{i=0}^n c_i \delta_t^i. \quad (5.33)$$

This means that $\mathcal{O}(t_K)|_{\delta_t=0}$ is given by the constant c_0 , which inherits a natural deviation due to the (non)linear fitting procedure. In practice, we have chosen $\Gamma\delta_t \leq 0.5$, which allows to resolve all physical properties for finite bias voltage and temperature. Note that for the current expectation values the fitting function is linear in δ_t , whereas the occupation number \mathcal{N} and the components of the spin projection $\mathcal{S}_{x,y,z}$ are fitted with quadratic order to sufficient accuracy for gate voltages $-2\Gamma < \varepsilon_0 < 2\Gamma$. Typical outcomes of this procedure are shown in Fig. 5.3 for the different observables. For the current we demonstrate different values of Coulomb interaction strength at the correlation time $\Gamma t_K = 1$. The other parameters are given by $k_B T = 0.2\Gamma$, $\varepsilon_0 = \Gamma$, $eV = 0.1\Gamma$, $\mathbf{B} = 0$, $p = 0.5$, $\theta = 0$. For the occupation number and the spin expectation values we show different gate voltages ε_0 at the same correlation time $\Gamma t_K = 1$. Other parameters are given by $k_B T = 0.2\Gamma$, $U = 0.5\Gamma$, $eV = 0.1\Gamma$, $B_y = 0.2\Gamma$, $p = 0.5$, $\theta = \pi/2$. ISPI data are given as symbols, and the solid lines display the fitted polynomial expression, which is used for the extrapolation towards $\delta_t \rightarrow 0$. This step eliminates the Trotter error.

(ii) Truncation error We repeat the extrapolation $\delta_t \rightarrow 0$ for different finite values of the correlation time t_K . Using the resulting values bereft of the Trotter error $\mathcal{O}(t_K)$, we eliminate the respectively associated truncation error by extrapolating to infinite correlation time with the help of a linear regression for $1/(\Gamma t_K) \rightarrow 0$. This step is similar for the current, occupation number and spin projections. The y -intercept of the linear regression is the final value with eliminated Trotter and truncation error. The procedure is shown in Fig. 5.4, again for the different observables, with the parameters chosen as before. For the current correlation times $\Gamma t_K = 0.5, \dots, 2$ are taken into account, while for the occupation number and spin projections we use $\Gamma t_K = 0.5, \dots, 1.5$. These are the ones that are compatible with $\Gamma\delta_t \leq 0.5$, while still allowing for a large enough number of values to perform the $\delta_t \rightarrow 0$ extrapolation from step (i).

Having eliminated the two sources of systematic errors, we are able to estimate error bars for the results of the convergence procedure from the standard deviations

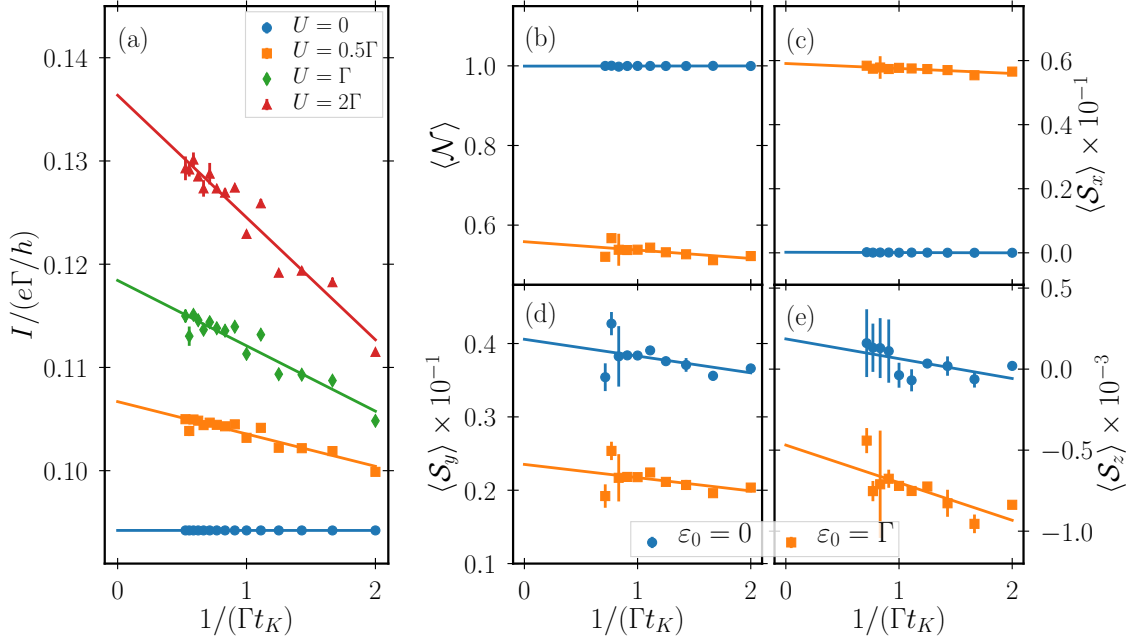


Figure 5.4: The regression in the inverse correlation time t_K for the current (a), as well as the occupation number and spin expectation values (b-e). For the current we show different Coulomb interaction strengths, while for the other observables two different values of the gate voltage ε_0 are depicted. The parameters are chosen similar to Fig. 5.3.

of both subsequent linear regressions.

Since we are interested in the stationary values of the different observables, we need to set the measurement time t_m large enough to overcome transient behavior. We find that for the quantum-dot spin valve $\Gamma t_m \geq 10$ is sufficient. We note in passing, that other systems, like e.g. a quantum dot coupled to a normal lead and a superconductor, may require significantly larger measurement times to reach the stationary state.

For the noninteracting case, $U = 0$, the errors are eliminated very efficiently with the described extrapolations, such that error bars are smaller than the symbol size in all curves presented for this case. With increasing U , the error bars become larger. We are able to obtain reliable results within reasonable computation time for intermediate values of the interaction up to $U = 2\Gamma$. Whenever the orbital of the dot is tuned far outside the transport window opened by the bias voltage (large $|\varepsilon_0|$ or small eV), the ISPI data for the current become noisy.

5.4 Parallelization and Performance

Even though we reduced the number of summations from 2^{2N} in Eq. (4.44) with $N \sim \mathcal{O}(10^2)$ to $N_K 2^{2K}$ in Eq. (5.13) via the ISPI scheme, where we took $K \leq 7$ into

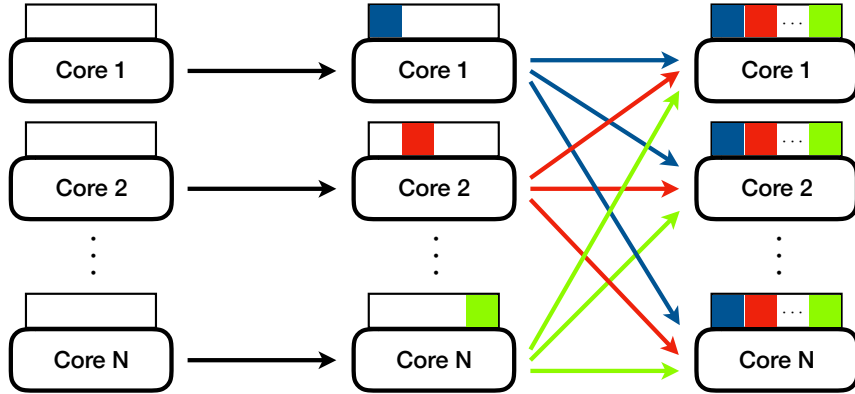


Figure 5.5: Systematic sketch of the parallel implementation of ISPI. After the initialization, each core calculates several lines of the transfer matrix independently of the others (symbolized by different colored boxes). These lines are then shared with the other cores, to build the full transfer matrix of this iteration step.

account, the method is still computation-intensive. On the one hand calculating current for one specific combination of discretization length δ_t and correlation time t_K still requires the summation over a large number of possible configurations of the Ising-like spins, with the different addends being built from determinants of products of matrices. On the other hand this has to be repeated several times to allow for the convergence procedure.

The ISPI code is fully parallelized allowing the calculation of $K \leq 8$ within reasonable computation time. The parallelization is implemented in such a way, that each core calculates some elements of the transfer matrix (meaning some possible configurations of the Ising-like spins) during each iteration step. The parallelization is realized using the Message Passing Interface (MPI). A sketch of the parallelization is given in Fig. 5.5. All calculations during the initialization of the iteration step are performed by all cores simultaneously. However, each core gets assigned a certain number of spin-configurations, which they calculate independently of one another to fill the transfer matrix. Each line is then multiplied with the current state vector $|\Lambda_n\rangle$, resulting into one element of state vector $|\Lambda_{n+1}\rangle$. In a final step the elements calculated from each core are shared with all the others, building the full state vector $|\Lambda_{n+1}\rangle$. This process is then repeated in the following iteration step until Eq. (5.13) is fully evaluated.

To better demonstrate the performance of the parallelization, we refer to Fig. 5.6. There, in panel (a) we demonstrate how the average calculation time per iteration step increases exponentially with increasing K . To obtain this picture, we run the ISPI code on three different machines: On S3 the code is not parallelized and runs

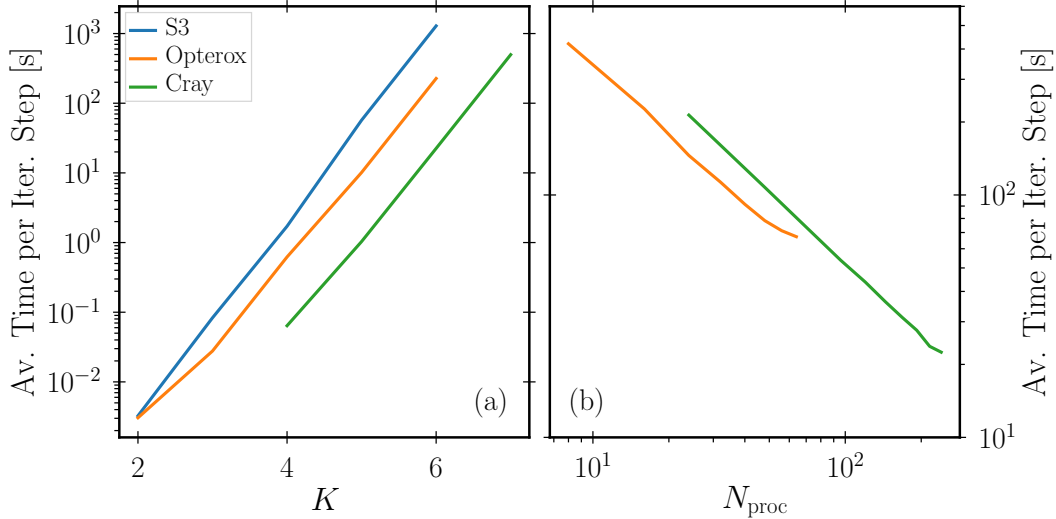


Figure 5.6: (a) Exponential increase of the average calculation time per iteration step with increasing K for different machines (see text). (b) Decrease of average calculation time per iteration step with increasing number of available processor cores for the case $K = 6$, with two different machines.

on one core of an Intel Xeon E5-2697 v2 at 2.70GHz, on the Opterox, the code runs on 16 cores of the type Intel Xeon E5-2650 at 2.00GHz, while on the Cray XT6m we used 240 cores. On these machines the current is calculated for a fixed correlation time, $\Gamma t_K = 1$ and set of parameters but with values $K = 2, \dots, 6$ for S3 and Opterox and $K = 4, \dots, 7$ for the Cray. We find a clear exponential increase in calculation time, which is attributed to the exponential increase of spin configurations with K . In panel (b) we show how calculation time per iteration step decreases when calculating the current with the same parameters and correlation time, while keeping $K = 6$ constant but varying the number of available processors. These calculations are only possible for the Opterox and Cray, since the code on the S3 runs sequential. For the Opterox we choose the number of processors as $N_{\text{proc}} = 8, \dots, 64$ in steps of 8, while on the Cray we choose $N_{\text{proc}} = 24, \dots, 240$. From Fig. 5.6 (b) it is obvious that the time necessary for one iteration step decreases such that doubling the number of processors reduces the necessary calculation time to about 50%, proving the efficiency of the parallelization procedure.

In Fig. 5.7 we compare the performance of our code for the finite-time implementation (Sec. 5.1) and for the transfer-matrix implementation (Sec. 5.2). We plot the time necessary to calculate the dot's occupation number for one specific parameter set as a function of K . Parameters are given by $k_B T = \frac{2}{11}\Gamma$, $\varepsilon_0 = 0.5\Gamma$, $U = \Gamma$, $eV = 3\Gamma$, $p = 0.5$, $\theta = \pi/2$, and measurement time $t_m \Gamma = 10$, and the memory time $t_K \Gamma = 1$. On average, we find that the transfer-matrix implementation is faster by a factor of 7. In addition, the necessary time for the finite-time implementation

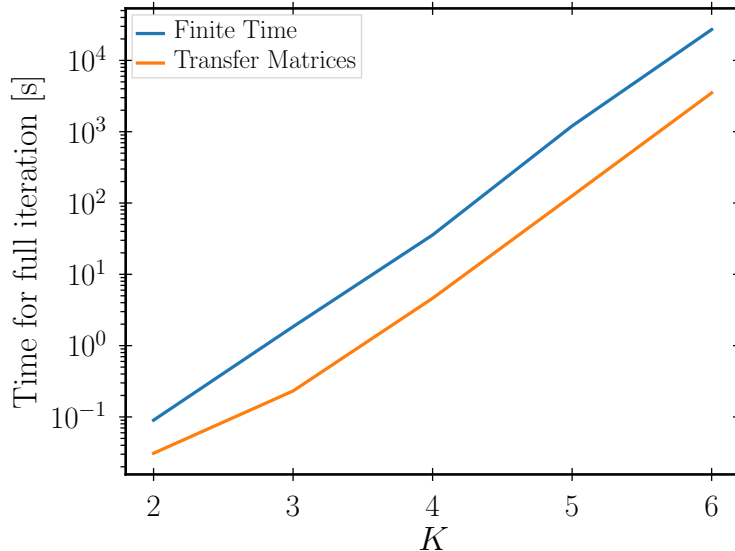


Figure 5.7: Comparison between the performance of the iterative summation scheme and the transfer-matrix approach. The time shown in this plot is the time to calculate the dot's occupation number for one specific set of parameters: $k_B T = 0.1\bar{8}\Gamma$, $\varepsilon_0 = 0.5\Gamma$, $U = \Gamma$, $eV = 3\Gamma$, $p = 0.5$, $\theta = \pi/2$. The measurement time is given by $t_m\Gamma = 10$ and the memory time $t_K\Gamma = 1$.

increases linearly with t_m/t_K , while the transfer-matrix technique is not affected by this. We also emphasize that the transfer-matrix implementation allows calculating multiple observables for the same set of parameters without having to build the transfer matrix Λ completely new. However, these faster calculation times are paid for with higher memory requirements, since it is necessary to store the complete transfer matrix. For $K = 6$ one fully occupied transfer matrix requires 256 MB of memory, $K = 7$ needs 4 GB and for $K = 8$ 64 GB of memory are necessary. This is less an issue for the finite-time implementation since there it is sufficient to work with the transfer matrix line by line.

There are other differences between the two implementations: The transfer-matrix approach works by definition in the long-term limit, while for the finite-time implementation we have to choose the measurement time large enough to reach this limit. However, the finite-time implementation allows us to study systems with e.g. a time-dependent gate or bias voltage, for which the transfer-matrix approach is not viable. Finally, calculating correlations between two points in time proves to be challenging within the finite-time implementation, but such calculations are usually possible within transfer-matrix approaches, and might be possible here, too.

5.5 Summary

In this chapter we introduced the ISPI scheme, which is used to break up the insurmountable summation over all configurations of all Hubbard-Stratonovich spins into manageable blocks of these spins. To achieve this we neglected lead-induced correlations after some memory time t_K , since they decay exponentially with time. We demonstrated how one is then able to construct an iterative scheme on the basis of continued use of Schur's formula to solve the sum over Hubbard-Stratonovich spin configurations. This resulted in the finite-time implementation of the ISPI technique. We were able to develop this method further, by introducing a mapping of the ISPI scheme to a transfer-matrix approach. This transfer-matrix implementation allows us to calculate expectation values of observables from a representation of the source term in the space of Hubbard-Stratonovich spin configurations and the largest eigenvalue and its corresponding eigenvector of the so-called transfer matrix.

In the rest of the chapter, we explained how one is able to obtain numerically exact data from the ISPI technique by making use of a convergence procedure. During this process we were able to eliminate the Trotter error, which was introduced by discretizing time, and the truncation error, caused by the truncation of the Green function, via consecutive extrapolations. The standard deviations of these extrapolations allow for an estimate of the error bars. We described how the ISPI code is parallelized, using the message passing interface (MPI) and demonstrated the scalability of this parallelization. Finally, we gave a comparison between the two implementations of the ISPI technique, presented within this chapter, which showed that they very much complement each other.

6 Results

In this chapter we present the results obtained via the two implementations of the ISPI method. The goal is to give a thorough investigation of the interacting quantum-dot spin valve. To achieve this we first demonstrate in an extensive benchmark, that our technique is valid and reproduces the results of other methods in the noninteracting limit and in the high temperature limit. Also, we show a comparison between the finite-time and the transfer-matrix implementation of the ISPI method. We then turn to the setup where the leads are magnetized collinearly ($\theta = 0$ or $\theta = \pi$). For this setup the main observable is the tunnel magnetoresistance (TMR) of the system, which is a measure for the strength of the spin-valve effect of the system. Afterwards we turn to effects that are introduced by a noncollinear setup via noncollinear magnetization directions of the leads and via an externally applied magnetic field. In this part we very much focus on the effect of resonant tunneling on the spin dynamics of the system and, thus, study the current through the system together with the dot's occupation number and spin projections.

Some results presented throughout this chapter were previously published in Refs. [119, 120]. Therefore, some parts of this chapter follow these works in an analogous manner, and other in verbatim. The same is true for some of the figures.

6.1 Benchmark

Having introduced the ISPI method, we convince ourselves of the reliability of our ISPI code. We therefore perform two benchmark tests. First, we consider a noninteracting spin valve, $U = 0$. In this case, the current as well as the occupation number and components of the spin projection of the quantum dot are calculated analytically (see Sec. 3.2). These analytic solutions are compared with ISPI data. Next, we compare the interacting ISPI data in the high-temperature regime with solutions from a first order and a first plus second order perturbation expansion in the hybridization strength Γ . A short introduction of this method is given in App. B, for a more detailed explanation we refer to Refs. [97, 121].

6.1.1 Noninteracting Limit

We have given derivations of the current as well as occupation number and spin components in Sec. 3.2 (see Eqs. (3.25) and (3.33)) for the case of a noninteracting quantum dot. For the cases $\theta = 0$ and $\theta = \pi$ without a magnetic field, we are able to simplify the noninteracting, analytical solution for the current given in Eq. (3.25).

The current formulas for parallel ($\theta = 0$) and antiparallel ($\theta = \pi$) magnetization configuration of the leads are given by

$$\begin{aligned} I_p &= \int_{-\infty}^{\infty} d\omega \frac{2\Gamma_+^2\Gamma_-^2 + (\Gamma_+^2 + \Gamma_-^2)(\omega - \varepsilon_0)^2}{[\Gamma_+^2 + (\omega - \varepsilon_0)^2][\Gamma_-^2 + (\omega - \varepsilon_0)^2]} \left[f\left(\omega - \frac{eV}{2}\right) - f\left(\omega + \frac{eV}{2}\right) \right] \\ I_{ap} &= \int_{-\infty}^{\infty} d\omega \frac{2\Gamma_+\Gamma_-}{\Gamma^2 + (\omega - \varepsilon_0)^2} \left[f\left(\omega - \frac{eV}{2}\right) - f\left(\omega + \frac{eV}{2}\right) \right]. \end{aligned} \quad (6.1)$$

These integrals are evaluated with the help of Cauchy's residual theorem. Collecting the residues at the poles of the Fermi functions, which are given by the Matsubara frequencies, and of the expression in front of the Fermi functions, we get

$$\begin{aligned} I_p &= \sum_{\tau=\pm} \sum_{\gamma,\gamma'=\pm 1} \frac{\gamma}{2} \Gamma_{\tau} \left\{ i\gamma'\Psi \left[\frac{1}{2} + \gamma' \frac{\beta\Gamma_{\tau}}{2\pi} - \frac{i\beta}{2\pi} \left(\gamma \frac{eV}{2} - \varepsilon_0 \right) \right] \right. \\ &\quad \left. - \pi f \left(\gamma \frac{eV}{2} + i\Gamma_{\tau} + \varepsilon_0 \right) \right\} \\ I_{ap} &= \sum_{\gamma,\gamma'=\pm 1} \gamma \Gamma (1 - p^2) \left\{ i\gamma'\Psi \left[\frac{1}{2} + \gamma' \frac{\beta\Gamma}{2\pi} - \frac{i\beta}{2\pi} \left(\gamma \frac{eV}{2} - \varepsilon_0 \right) \right] \right. \\ &\quad \left. - \pi f \left(\gamma \frac{eV}{2} + i\Gamma + \varepsilon_0 \right) \right\}, \end{aligned} \quad (6.2)$$

where $\Psi(x)$ denotes the digamma function [122]. For more complex setups, like noncollinear magnetizations of the leads or an additional magnetic field active on the dot, solving the energy integral is complicated and leads to lengthy expressions, that we do not write down here. Alternatively, one is able to solve the integrals numerically.

For a collinear setup, $\theta = 0, \pi$, the results can be seen in Fig. 6.1, where in panel (a) the current through the system in a parallel and antiparallel setup as a function of bias voltage V is shown. In the inset, we depict the TMR, see Eq. (1.1), resulting from this setup. In panel (b) on the other hand we show the TMR for different values of the polarization p as a function of the gate voltage ε_0 . The solid lines represent the analytical solution and the symbols ISPI data, with the errors being of the order of the symbol size. The other parameters are given in panel (a) by $k_B T = 0.2\Gamma$, $\varepsilon_0 = 0$, $p = 0.8$ and $\mathbf{B} = 0$ and for panel (b) by $k_B T = 0.2\Gamma$, $eV = 0.1\Gamma$, $\mathbf{B} = 0$. We find excellent agreement between the analytical results and ISPI for both the full $I - V$ characteristics and the TMR as a function of ε_0 . In the TMR we find a central maximum, at $eV = 0$, $\varepsilon_0 = 0$, which is well resolved in the ISPI data.

In Fig. 6.2 we turn to a noncollinear setup and include an external magnetic field in different directions. We show the linear conductance for different setups of the lead magnetizations, namely parallel ($\theta = 0$), orthogonal ($\theta = \pi/2$) and antiparallel ($\theta = \pi$) as a function of the gate voltage ε_0 . The quantum dot is subject to an external Zeeman field in x -direction of $B_x = 2\Gamma$ (panel (a)), in y -direction of $B_y = 2\Gamma$

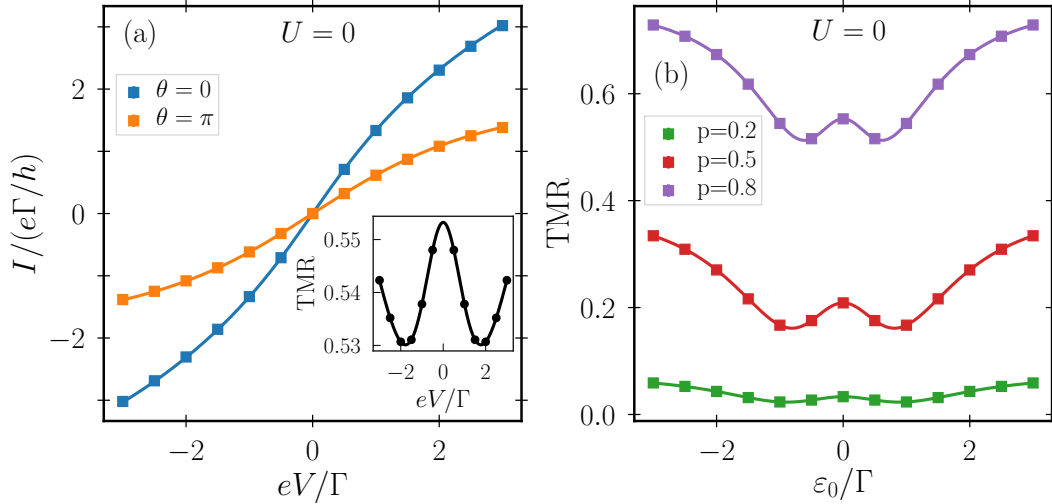


Figure 6.1: (a) $I - V$ characteristics of the noninteracting quantum-dot spin valve in collinear setup. (inset) The TMR resulting from the currents in parallel and antiparallel setup of the leads' magnetizations. Other parameters are $k_B T = 0.2\Gamma$, $\varepsilon_0 = 0$, $p = 0.8$. (b) TMR as a function of gate voltage ε_0 , in the linear response regime $eV = 0.1\Gamma$ at low temperature $k_B T = 0.2\Gamma$. Lines show the analytical results, symbols represent ISPI data. No external magnetic field has been applied for this figure. Error bars are of the order of the symbol size.

(panel (b)), in z -direction of $B_z = 2\Gamma$ (panel (c)). Other parameters are $k_B T = 0.2\Gamma$, $eV = 0.1\Gamma$, $p = 0.5$. We compare the analytic results (solid lines) with ISPI data (symbols) and note that ISPI error bars are of the order of the symbol size. For all cases ISPI data reproduces the analytical solution perfectly. Resonant transport through a noninteracting single level results in a Lorentzian conductance profile as a function of gate voltage ε_0 for $p = 0$. The maximum is centered around $\varepsilon_0 = 0$ and the width is determined by the tunnel coupling strength Γ at low temperatures $k_B T < \Gamma$. A finite magnetic field lifts the spin degeneracy and two maxima, which are split by $B_{x/y/z}$, develop as a function of ε_0 , see Fig. 6.2. Due to a low but finite temperature and the tunnel coupling Γ , the peak splitting is not fully developed, i.e. the peak-to-peak distance is somewhat smaller than $B_{x/y/z}/\Gamma = 2$ here.

The impact of the angle θ on the linear conductance varies significantly, depending on the direction of the magnetic field. In Fig. 6.2(a) we observe an asymmetry that develops as a function of the gate voltage, when the magnetic field points along the x -axis. This asymmetry does depend strongly on the angle θ as well as the degree of polarization p of the leads. For $\theta = 0$ the difference between left and right peak is largest, while it decreases for increasing angle, until we reach a fully symmetric setup at $\theta = \pi$. This asymmetry is traced back to the polarization strength of the leads, in our case $p = 0.5$, which introduces spin-dependent hybridization strengths

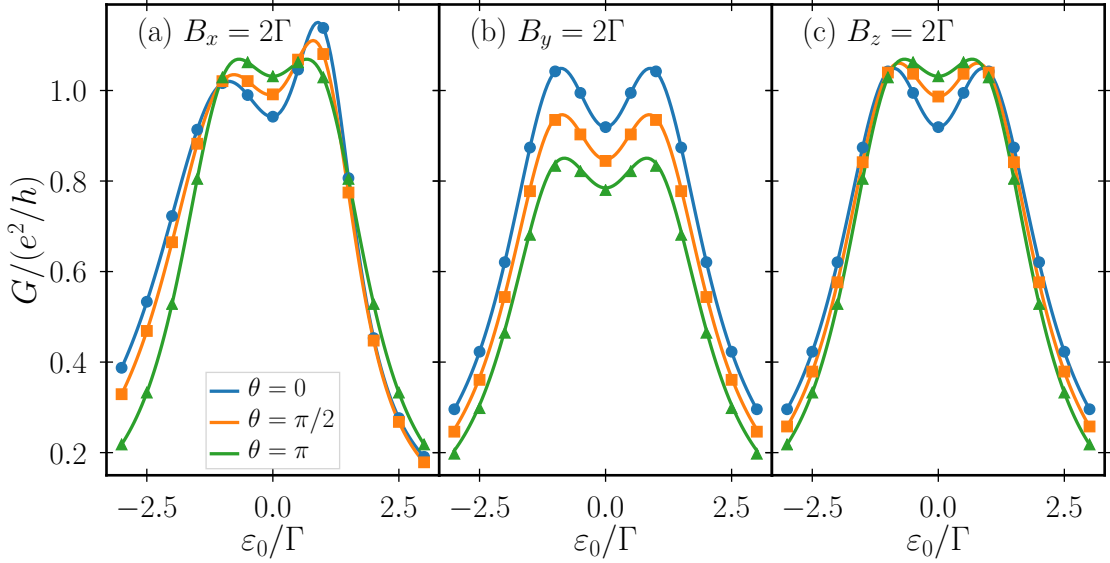


Figure 6.2: Linear conductance as a function of the gate voltage for the case of a noninteracting quantum dot and a nonzero magnetic field that points in (a) x -direction with $B_x = 2\Gamma$, (b) y -direction with $B_y = 2\Gamma$, (c) z -direction with $B_z = 2\Gamma$. Lines show the analytical results, symbols represent ISPI data. Error bars are of the order of the symbol size. Other parameters are given by $k_B T = 0.2\Gamma$, $eV = 0.1\Gamma$, $p = 0.5$.

$\Gamma_{\alpha\pm} = \Gamma_{\alpha}(1 \pm p)$. As a consequence, the coupling between dot and leads is stronger for the majority spins, resulting in a broader peak. We have convinced ourselves that this asymmetry survives even for bias voltages outside the linear response regime ($eV \geq \Gamma$).

When applying the magnetic field in y -direction (Fig. 6.2(b)), we find that the two peaks are symmetric with respect to $\varepsilon_0 = 0$, meaning that an external field in y -direction does not break the system's particle-hole symmetry for $U = 0$. The conductance is maximal for $\theta = 0$ and becomes suppressed as the angle increases, reaching its minimum in the antiparallel setup $\theta = \pi$. This can be understood via the geometry of the setup and the fact that spins precess around magnetic fields that are noncollinear to the spins magnetic moment. For the case of $\theta = 0$, the magnetic field is perpendicular to the magnetization direction of the leads, leading to precession of the spins around the y -axis. Thus, both minority and majority spins can easily move in and out of the quantum dot, whenever they are aligned properly. For the case of antiparallel magnetization, $\theta = \pi$, however, the spin's magnetic moment and the Zeeman field are aligned and no precession occurs. As a result majority spins in the left lead cannot freely pass to the right lead, since it is magnetized in the opposite direction. Consequently, the minority spins dominate transport for $\theta = \pi$, leading to the observed suppression.

In Fig. 6.2(c) we find that the width of the peaks is maximal for the antiparallel setup and minimal for the case of the magnetizations being parallel. The width

of the peaks varies with θ , where the width increases with the angle reaching its maximum at $\theta = \pi$. The height of the peaks is not affected, small variations are due to a stronger overlap of the two peaks. The two peaks are symmetric with respect to $\varepsilon_0 = 0$, since, again, an external magnetic field in z -direction keeps the system's particle-hole symmetry intact for the noninteracting case $U = 0$.

We turn to the occupation number and the components of the spin projection in the case of a quantum-dot spin valve that is noninteracting, but in presence of an external magnetic field. We focus on the cases of magnetic field in x - and z -direction. From the noninteracting, analytical solution, Eqs. (3.33), we find the following formulas for the components of spin projection, if the magnetic field points in x -direction

$$\langle \mathcal{S}_x \rangle = \int \frac{d\omega}{4\pi} \frac{2\Gamma(2B_x(\omega - \epsilon_0) + p \cos(\frac{\theta}{2})c_x^+)}{(c_x^-)^2 + 4\Gamma^2[(\omega - \epsilon_0) + pB_x \cos(\theta/2)]^2} [f_L(\omega) + f_R(\omega)] \quad (6.3)$$

$$\langle \mathcal{S}_y \rangle = - \int \frac{d\omega}{4\pi} \frac{2\Gamma p \sin(\theta/2)c_x^+}{(c_x^-)^2 + 4\Gamma^2[(\omega - \epsilon_0) + pB_x \cos(\theta/2)]^2} [f_L(\omega) - f_R(\omega)] \quad (6.4)$$

$$\langle \mathcal{S}_z \rangle = \int \frac{d\omega}{4\pi} \frac{4\Gamma^2 p \sin(\theta/2)[B_x + p(\omega - \epsilon_0) \cos(\theta/2)]}{(c_x^-)^2 + 4\Gamma^2[(\omega - \epsilon_0) + pB_x \cos(\theta/2)]^2} [f_L(\omega) - f_R(\omega)], \quad (6.5)$$

where we introduced the short hands $c_j^\pm = [(\omega - \epsilon_0)^2 \pm B_j^2 + (\Gamma^2 p^2 \cos(\theta) - \Gamma_\uparrow \Gamma_\downarrow)/2]$, with $j = x, y, z$ and $f_{L/R}(\omega) = f(\omega \mp eV/2)$. When the magnetic field points in z -direction we find

$$\langle \mathcal{S}_x \rangle = \int \frac{d\omega}{4\pi} \left[\frac{2\Gamma p \cos(\frac{\theta}{2}) ((\omega - \epsilon_0)^2 - B_z^2 + \Gamma^2 (p^2 \cos^2(\frac{\theta}{2}) - 1))}{(c_z^-)^2 + 4\Gamma^2(\omega - \epsilon_0)^2} [f_L(\omega) + f_R(\omega)] - \frac{4B_z \Gamma^2 p \sin(\frac{\theta}{2})}{(c_z^-)^2 + 4\Gamma^2(\omega - \epsilon_0)^2} [f_L(\omega) - f_R(\omega)] \right] \quad (6.6)$$

$$\langle \mathcal{S}_y \rangle = - \int \frac{d\omega}{4\pi} \frac{2\Gamma p \sin(\theta/2)c_z^+}{(c_z^-)^2 + 4\Gamma^2(\omega - \epsilon_0)^2} [f_L(\omega) - f_R(\omega)] \quad (6.7)$$

$$\langle \mathcal{S}_z \rangle = \int \frac{d\omega}{4\pi} \left[\frac{4B_z \Gamma(\omega - \epsilon_0)}{(c_z^-)^2 + 4\Gamma^2(\omega - \epsilon_0)^2} [f_L(\omega) + f_R(\omega)] + \frac{2\Gamma^2 p^2 (\omega - \epsilon_0) \sin(\theta)}{(c_z^-)^2 + 4\Gamma^2(\omega - \epsilon_0)^2} [f_L(\omega) - f_R(\omega)] \right]. \quad (6.8)$$

One is able to evaluate the integrals via residue theorem or numerically. The resulting formulas are lengthy, and we do not write them down here. These formulas are used as benchmarks for the noninteracting cases of the components of the spin projection in what follows.

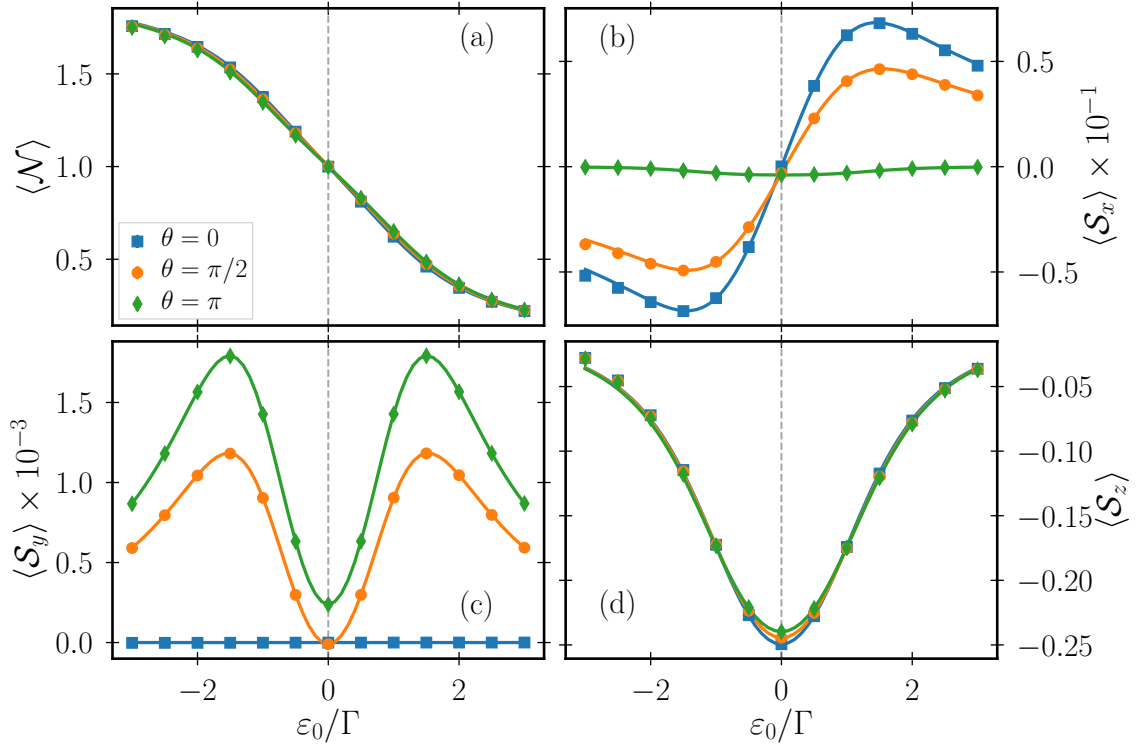


Figure 6.3: The four local observables $\langle \mathcal{N} \rangle$, $\langle \mathcal{S}_{x,y,z} \rangle$ for the noninteracting case as a function of the gate voltage ε_0 . Parameters are chosen as in Fig. 6.2 (c), where $B_z = 2\Gamma$.

In Fig. 6.3 we study the occupation number and spin-projection expectation values as a function of the gate voltage ε_0 for the same setup as in Fig. 6.2 (c), meaning the local magnetic field is given by $B_z = 2\Gamma$. Again, we find a good agreement for all four observables between the analytical solution and the data received via the ISPI scheme. We find a doubly occupied dot for large negative gate voltages $\varepsilon_0 < -2\Gamma$ and an unoccupied dot for gate voltages $\varepsilon_0 > 2\Gamma$. At the particle-hole symmetric point, $\varepsilon_0 = 0$, the dot is singly occupied. Differences for the different angles are marginal. Regarding spin expectation values, we find finite $\langle \mathcal{S}_x \rangle$, which is particularly developed for $\theta = 0$ and $\theta = \pi/2$ due to resonant tunneling effects, as opposed to lowest-order-in- Γ predictions for the quantum-dot spin valve [27]. A small but finite $\langle \mathcal{S}_x \rangle$ for $\theta = \pi$ is addressed to the external magnetic field. We observe symmetric $\langle \mathcal{S}_y \rangle$ curves with respect to $\varepsilon_0 = 0$ for $\theta = \pi$ and $\theta = \pi/2$, whereas $\langle \mathcal{S}_y \rangle = 0$ for $\theta = 0$, see Eqs. (6.6), where $\langle \mathcal{S}_y \rangle \propto \sin(\theta/2)$. The footprint of the external magnetic field applied in z -direction is reflected in $\langle \mathcal{S}_z \rangle$, where a clear minimum at $\varepsilon_0 = 0$ is visible. Also, the dependence on the enclosed angle θ is superposed by the external field and hence marginally detectable.

When applying a magnetic field in x -direction, see Fig. 6.4, left-right symmetry is broken, as was already shown for the conductance. The asymmetry in ε_0 due to the spin-dependent coupling between dot and leads is also visible in the spin

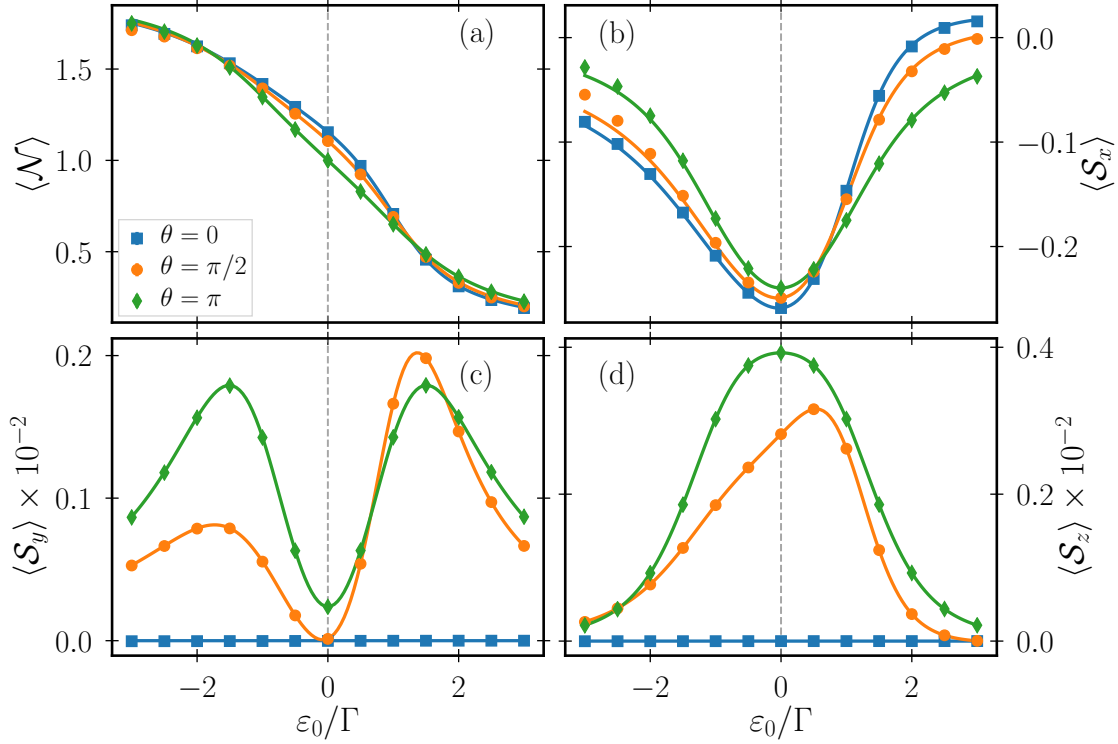


Figure 6.4: The four local observables $\langle \mathcal{N} \rangle$, $\langle \mathcal{S}_{x,y,z} \rangle$ for the noninteracting case as a function of the gate voltage ε_0 . Parameters are chosen as in Fig. 6.2 (a), where $B_x = 2\Gamma$.

projection, i.e. only the curves for $\theta = \pi$ are symmetric with respect to $\varepsilon_0 = 0$. Note that due to the absence of a spin-valve effect, for $\theta = 0$ both $\langle \mathcal{S}_y \rangle$ and $\langle \mathcal{S}_z \rangle$ are vanishing, whereas for the other angles all three components of the spin projection are finite. In fact, even though the leads are magnetized within the x - y -plane the spin projection in z -direction is nonzero. This behavior is caused by precession of the spin around the magnetic field in x -direction. The asymmetry effect cancels for a magnetic field in y - or z -direction in the absence of interactions. These particular choices of the magnetic field result in a spin precession that annihilates the effect of aforementioned spin-dependent hybridization.

To sum up our findings for the noninteracting case, we have ensured that ISPI data match perfectly with the analytic solution for all observables and all parameter choices studied in this work. It is noteworthy that even in the noninteracting case an asymmetric functional shape in the current and subsequently the occupation number and spin expectation values is observable when gate voltages are tuned.

6.1.2 High-Temperature Regime

In the presence of interactions a fully analytical solution is not available anymore. However, in the limit of high temperature, $k_B T \gg \Gamma$, the tunnel coupling can be

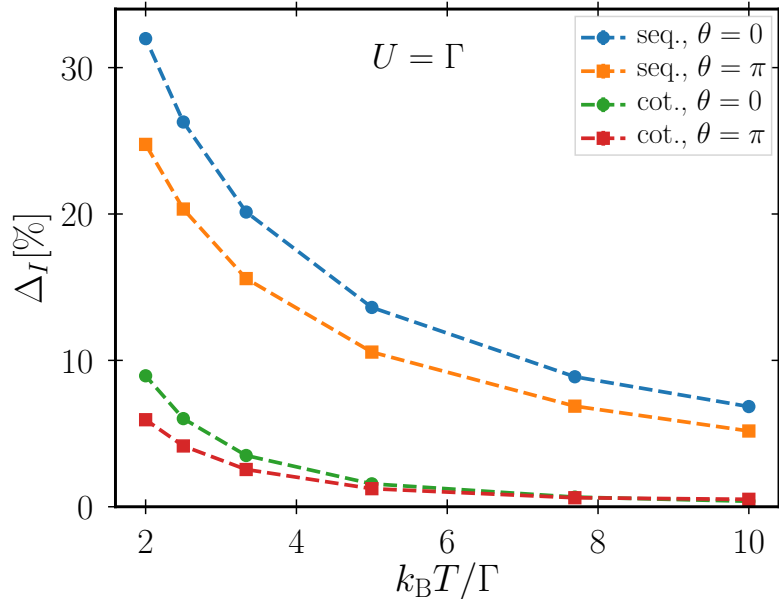


Figure 6.5: Percental difference between the current in a (anti)parallel setup obtained via ISPI and a sequential (seq.) or sequential plus cotunneling (cot.) ansatz, respectively, as a function of temperature. Lines are guide to the eye only. Other parameters are $\varepsilon_0 = 0$, $U = \Gamma$, $eV = 3\Gamma$, $\mathbf{B} = 0$, $p = 0.5$.

treated as a perturbation and the theory expanded in orders of Γ (see App. B). To lowest order, only sequential-tunneling processes contribute, while cotunneling processes are taken into account when expanding to the second order in Γ . The first order theory for the quantum-dot spin valve was formulated within a diagrammatic real-time technique [27] and was expanded upon including second order contributions [123, 124], referred to sequential plus cotunneling in this thesis.

This enables us to perform a benchmark for the interacting case. We compare the ISPI data with those obtained from sequential as well as sequential plus cotunneling calculations as a function of temperature, and check whether the ISPI data converge for high temperatures with the results from the master-equation approach. The result is shown in Fig. 6.5, where we plot the relative deviation of the sequential (seq) or sequential plus cotunneling (cot) current from the ISPI results as a function of temperature. We define

$$\Delta_I = \left| \frac{I_{\text{seq/cot}} - I_{\text{ISPI}}}{I_{\text{ISPI}}} \right|. \quad (6.9)$$

For the perturbative results we use the scheme developed in Ref. [123, 124] and we cover both the parallel ($\theta = 0$) and the antiparallel ($\theta = \pi$) configuration. Other parameters are set to $eV = 3\Gamma$, $\varepsilon_0 = 0$, $U = \Gamma$, $p = 0.5$. Lines are guides to the eye only.

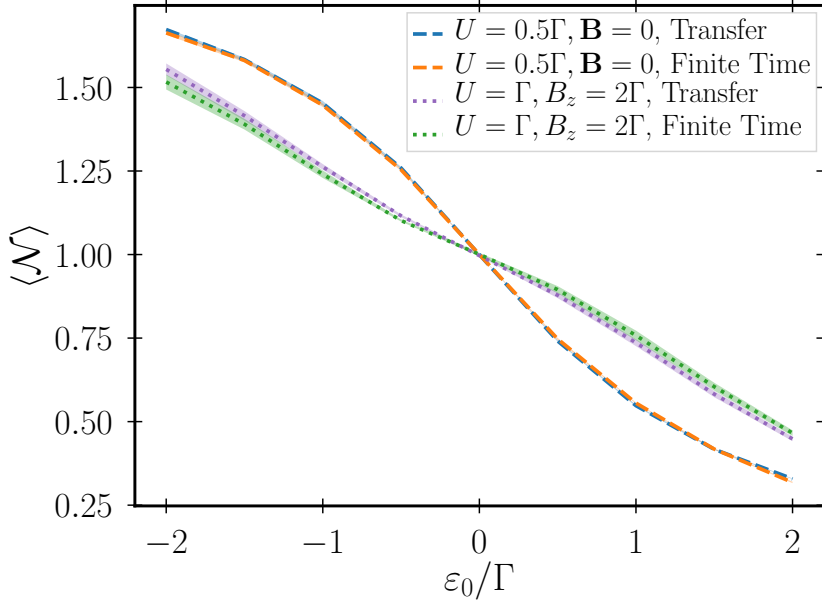


Figure 6.6: The quantum dot's occupation number as a function of the gate voltage ε_0 for the cases $U = 0.5\Gamma$, $\mathbf{B} = 0$ as well as $U = \Gamma$, $B_z = 2\Gamma$. We compare the results obtained via the finite-time implementation and via the transfer-matrix implementation. Shaded areas are error estimates. Other parameters are $k_B T = 0.2\Gamma$, $eV = 0.1\Gamma$, $p = 0.5$, $\theta = \pi/2$. The measurement time t_m is $\Gamma t_m = 20$ for the finite-time implementation.

We find a good agreement between ISPI data and the results from perturbative calculations, once $k_B T \gg \Gamma$. While sequential tunneling is only sufficient for temperatures much larger than Γ , a sequential plus cotunneling approach remains reliable for temperatures that are only somewhat larger than Γ . As soon as $k_B T \leq \Gamma$, however, perturbation theory clearly fails and cannot compete with the ISPI approach. Since tunnel processes of different orders in the tunnel coupling contribute very differently to spin accumulation and spin relaxation, we are not surprised that a perturbative calculation of the TMR breaks down already at relatively high temperatures.

6.1.3 Finite-Time and Transfer-Matrix Implementation

Having assured ourselves that the code of the finite-time implementation of the ISPI technique produces reliable results, we now compare these results with the ones obtained from the code handling the extension to the transfer-matrix implementation, Eq. (5.25). In Fig. 6.6 we show the occupation number as a function of the gate voltage ε_0 . We show two different parameter regimes: For the first we choose a rather low Coulomb interaction strength $U = 0.5\Gamma$ and do not apply an external

magnetic field, $\mathbf{B} = 0$. The second case is a more demanding regime, where we have increased the Coulomb interaction $U = \Gamma$ and added a strong Zeeman field in z -direction $B_z = 2\Gamma$. Other parameters are given by $k_B T = 0.2\Gamma$, $U = 0.5\Gamma$, $\mathbf{B} = 0$, $eV = 0.1\Gamma$, $p = 0.5$ and $\theta = \pi/2$. For the finite-time results the measurement time was chosen to be $\Gamma t_m = 20$ to reach the stationary limit. The transfer-matrix approach on the other hand operates in the stationary limit by construction.

For the first case, where $U = 0.5\Gamma$, $\mathbf{B} = 0$, we find perfect agreement between the two implementations. When Coulomb interactions are low and no external magnetic field is applied, the system reaches the stationary limit very early and thus the two implementations yield the same results. For the more sophisticated setup with higher Coulomb interactions and an additional Zeeman field, both implementations still very much agree. However, there is a slight difference between the results of the two implementations. This is due a slower convergence of the time evolution to the stationary limit. As a result, one would have to increase the measurement time in the finite-time implementation further to perfectly reproduce the results from the transfer-matrix approach. Nonetheless, this shows that the transfer-matrix implementation is a viable option to calculate the occupation number or spin projections via the ISPI technique.

6.2 Collinear Setup

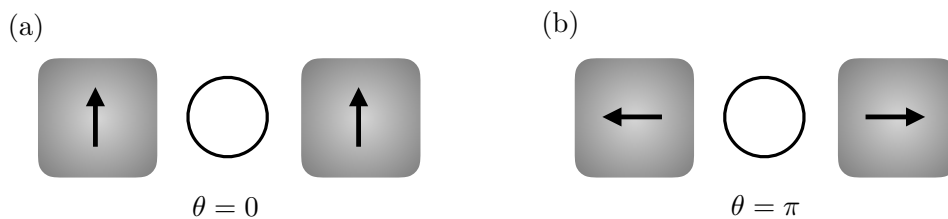


Figure 6.7: Collinear setups of the lead magnetizations in the quantum-dot spin valve used in the definition of the TMR.

We now turn to the discussion of the TMR through a quantum-dot spin valve for the experimentally relevant regime in which the energy scales for Coulomb interaction, tunnel coupling, and temperature are all of the same order of magnitude. Neither the fully analytical $U = 0$ formulas, nor a perturbative treatment of tunneling, nor any zero-temperature calculation done with other methods such as NRG is applicable. We study the system in a collinear setup, where the angle between the magnetizations of left and right lead is some multiple of π , i.e. $\theta = 0, \pi, 2\pi, \dots$. For the case of $\theta = 0$ the magnetizations are parallel and aligned in the positive x -direction (Fig. 6.7 (a)). When $\theta = \pi$ the leads are magnetized along the y -direction in an antiparallel fashion (Fig. 6.7 (b)). For $\theta = 2\pi$ the magnetizations are again parallel, but pointing in the $-x$ -direction. The TMR introduced during Sec. 1.1.2

and defined in Eq. (1.1), with $I_p \equiv I(\theta = 0)$ and $I_{ap} \equiv I(\theta = \pi)$. There we also mentioned that the TMR depends sensitively on the relative importance of different tunnel processes that contribute directly and indirectly to the current.

The fact that the nature of the dominating transport channel largely affects the TMR has been extensively discussed in the literature. Measurements of the TMR for weak tunnel coupling outside the Coulomb-blockade regime [13] could be explained within a sequential-tunneling picture. In the Coulomb-blockade regime, however, cotunneling dominates, leading to an enhancement of the TMR as compared to the sequential-tunneling result [83, 123–126]. For a qualitative explanation of the TMR measured through a quantum-dot spin valve with strong tunnel coupling, a Breit-Wigner form of the transmission has been assumed [46, 50]. While the Breit-Wigner form takes resonant-tunneling processes into account, it fails to describe correlations that, at very low temperature, give rise to the Kondo effect. The formation of Kondo correlations is accompanied by an enhancement of the transmission through the dot, which gives rise to a large, bias-voltage-dependent TMR as observed in Refs. [14, 28, 49]. Finally, we mention that also for quantum-dot spin valves in which not only the leads but also the island is ferromagnetic, an enhancement of the TMR due to cotunneling has been experimentally [127–129] and theoretically [130] found.

6.2.1 Temperature Dependence

The importance of resonant tunneling, i.e. higher-order tunneling contributions, for a proper description of transport through a quantum-dot spin valve is nicely demonstrated by the temperature dependence of the TMR. In Fig. 6.8 we demonstrate this for the regime of low and high bias voltage (panel (a) $eV = 0.1\Gamma$, panel (b) $eV = 3\Gamma$) and for a noninteracting quantum dot, $U = 0$. Shown are the analytical solution of the TMR (ANA) together with ISPI data (symbols) and the results of a perturbation theory for the TMR in Γ . We show the expansion up to order Γ , up to order Γ^2 , up to order Γ^3 and up to order Γ^4 .

We find that ISPI data perfectly reproduces the analytical solution, just as in the benchmarks in Sec. 6.1.1. In the sequential-tunneling approximation (up to order Γ), the TMR is independent of both, temperature and bias voltage, if $U = 0$ and is just given by $\text{TMR} = p^2$ [123]. Including the second or higher orders, the TMR becomes a nonmonotonic function of temperature, which converges to the sequential value for large temperatures $k_B T \gg \Gamma$. Nonphysical oscillations arise, which even extend to values of the TMR outside the interval $[0; 1]$. These oscillations are less severe once the bias voltage becomes sufficiently large, since then higher order processes are increasingly suppressed. The cotunneling approximation (up to order Γ^2) seems to give reliable results for temperatures of $k_B T \approx 10\Gamma$. Strikingly, not even a fourth order expansion is able to properly describe the correct temperature dependence of the TMR down to $k_B T \lesssim \Gamma$. We infer, that in the regime where the temperature and Γ are both of the same order of magnitude, resonant tunneling becomes overwhelmingly important and perturbation theory fails severely.

We continue by introducing Coulomb interactions on the quantum dot, and study

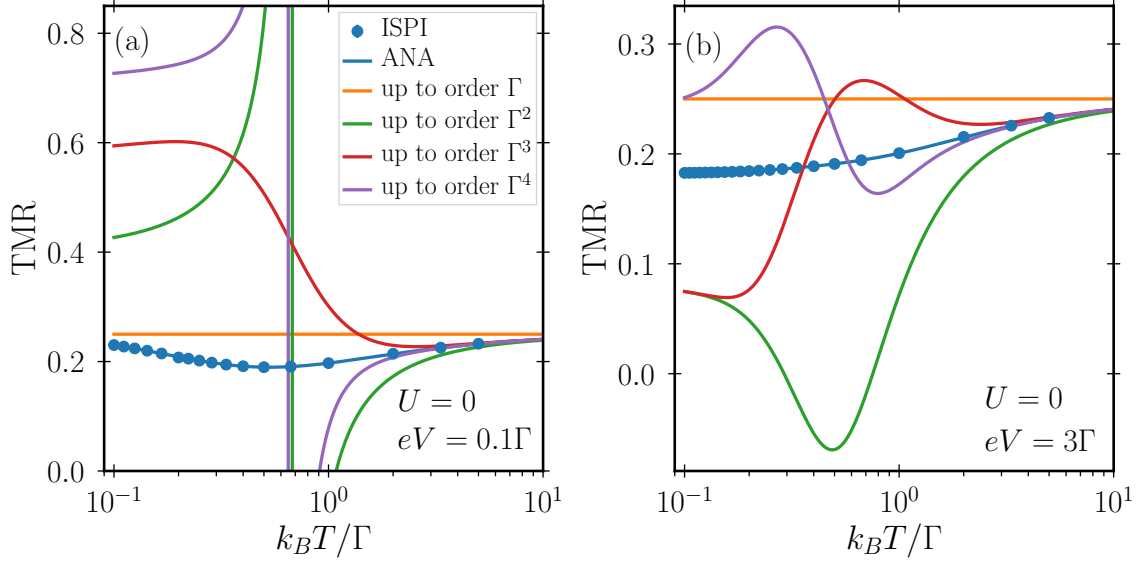


Figure 6.8: Temperature dependence of the TMR for a noninteracting setup, $U = 0$. Comparison between the analytical results, ISPI data as well as results from a perturbation expansion in Γ , with different orders taken into account for (a) the regime of low bias voltage $eV = 0.1\Gamma$ and (b) large bias voltage $eV = 3\Gamma$. Other parameters are given by $\varepsilon_0 = 0$, $p = 0.5$. Error bars of ISPI data are of the order of the symbol size.

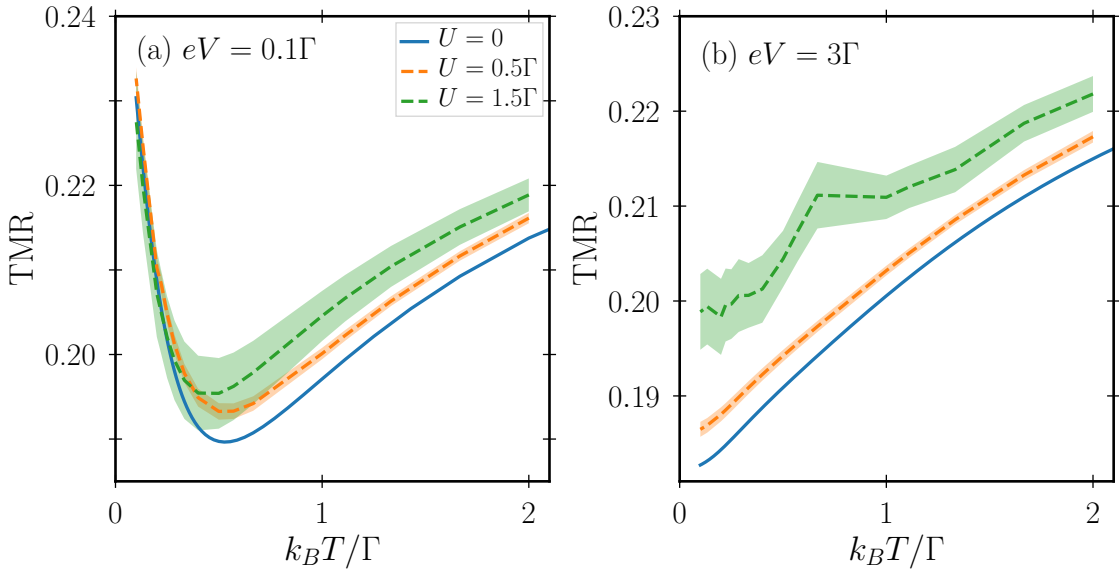


Figure 6.9: Temperature dependence of the TMR for different values of the Coulomb interaction strength, $U = 0, 0.5\Gamma, 1.5\Gamma$. (a) Regime of low bias voltage $eV = 0.1\Gamma$, and (b) regime of high bias voltage $eV = 3\Gamma$. Other parameters are chosen as in Fig. 6.8.

their impact on the temperature dependence of the TMR. In Fig. 6.9, we show the TMR as a function of the temperature for different values of the Coulomb interaction strength. Again, in panel (a) we show the low bias regime $eV = 0.1\Gamma$, while in panel (b) the regime of large bias voltage, $eV = 3\Gamma$, is shown. The other parameters are the same as for Fig. 6.8. For finite U an analytical solution is not available anymore, and we also abstain from showing results from a perturbation expansion, since its values are far off for the temperature regime under discussion. Coulomb interactions increase the TMR, but they do not change the qualitative behavior of the temperature dependence. In the regime of small bias voltage, Fig. 6.9(a), we find a nonmonotonic behavior of the TMR. For $k_B T \rightarrow \infty$ the TMR approaches the sequential-tunneling value $\text{TMR} = p^2 = 0.25$, as was already discussed for Fig. 6.8. Interestingly, for $\varepsilon_0 = 0$ and at small bias voltage, the low-temperature limit, $k_B T \rightarrow 0$, yields $\text{TMR} = p^2$, too. This can be understood directly, from the analytical formulas, Eqs. (6.1). For $k_B T \rightarrow 0$ the Fermi functions are replaced by Heaviside functions, and for $eV \rightarrow 0$ the difference between the two Heaviside functions is replaced by $\delta(0)$. With these results, and for $\varepsilon_0 = 0$, one readily finds the desired result. For intermediate temperatures, the TMR is decreased, displaying a minimum at $k_B T = 0.5\Gamma$ with $\text{TMR} \approx 0.195$.

With increasing bias voltage the value of the TMR at $k_B T \rightarrow 0$ decreases (not shown here). The nonmonotonic behavior is lost once the bias voltage becomes sufficiently large, see Fig. 6.9(b). For $eV = 3\Gamma$ the TMR increases monotonically with temperature and approaches the expected sequential tunneling value p^2 .

6.2.2 Transport Spectroscopy

We turn to the evaluation of the gate and bias voltage dependence of the TMR since both are usually tunable in experiment with high precision. Again, we start with a discussion of the noninteracting case, $U = 0$. At low temperature $k_B T = 0.1\Gamma$, the TMR shows a rather rich structure as a function of both voltages, see Fig. 6.10. In particular, there is a peak at $\varepsilon_0 = 0$, $eV = 0$. The full width at half maximum of the peak as a function of ε_0 and eV , respectively, depends on the degree of spin polarization p , see inset of Fig. 6.10. With increasing bias voltage, the local maximum of the TMR as a function of ε_0 first stays at $\varepsilon_0 = 0$ but then bifurcates into two local maxima. The position of the local maximum as a function of ε_0 is highlighted by a dashed line in Fig. 6.10. Once the level position ε_0 is tuned far away from resonance, $|\varepsilon_0| \gg \Gamma, |eV|$, the TMR approaches Julliere's value, Eq. (1.2), $\text{TMR}^{\text{Jull}} = 0.4$. This is expected, since in this regime, accumulation and relaxation of the quantum-dot spin can be neglected. The quantum dot becomes effectively invisible for transport, since cotunneling processes dominate. As a result, the quantum-dot spin valve behaves like a single tunnel junction. On the other hand, once the bias voltage is large, $|eV| \gg \Gamma, |\varepsilon_0|$, the TMR converges to the value obtained by sequential tunneling. Again, this is not a surprise since this is exactly the regime of sequential tunneling, where higher order processes are suppressed and can be neglected effectively.

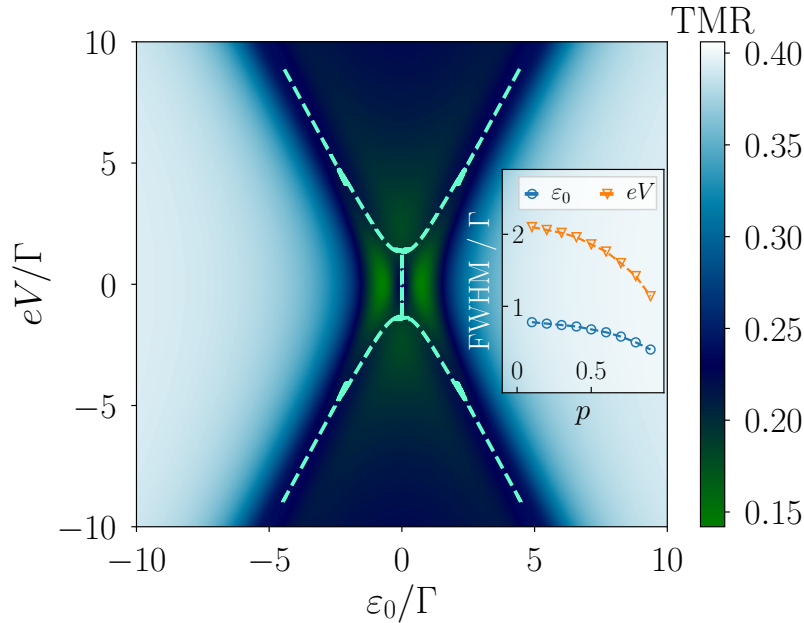


Figure 6.10: TMR for the noninteracting system as a function of gate and bias voltage. The temperature is $k_B T = 0.1\Gamma$, the leads' polarization is $p = 0.5$ and no external magnetic field is applied. The dashed line highlights the position of the local maximum of the TMR as a function of ε_0 . We find a bifurcation at finite bias voltage. (Inset) Full width half maximum of the local maximum in the center along the ε_0 and eV as a function of the polarization p .

The failure of perturbation theory is once more demonstrated impressively in Fig. 6.11. Here, we show the gate-voltage dependence of the TMR for $U = 0$ in the linear response regime, $eV = 0.1\Gamma$, and compare it to the full analytical result (ANA), obtained from Eqs. (6.1), as well as a perturbative expansion of the latter up to fourth order in Γ . The ISPI data (symbols) perfectly match the full analytical results, while finite order perturbation theory is not only quantitatively but even qualitatively wrong. Only when $|\varepsilon_0| \gg \Gamma$ become second and higher order perturbation theories reliable, predicting Julliere's value of the TMR. This, again, emphasizes the importance of resonant-tunneling effects for the TMR, especially, in a scenario where all energy scales are of the same order of magnitude.

We now include finite Coulomb interaction, $U \neq 0$. In Fig. 6.12(a) we show the gate-voltage dependence of the TMR for $U/\Gamma = 0, 1$, and 2 in the linear-response regime $eV = 0.1\Gamma$. The local maximum at resonance $\varepsilon_0 = 0$ remains clearly visible for all chosen values of U . The error bars of the ISPI data are quite moderate even for $U = 2\Gamma$. Since for large $|\varepsilon_0|$ the TMR goes up to Julliere's value, there are two minima symmetrically placed around the central maximum. With increasing U , the depth of the minima seems to shrink a bit.

In Fig. 6.12(b) we switch to the nonlinear-response regime $eV = 1.5\Gamma$. This bias

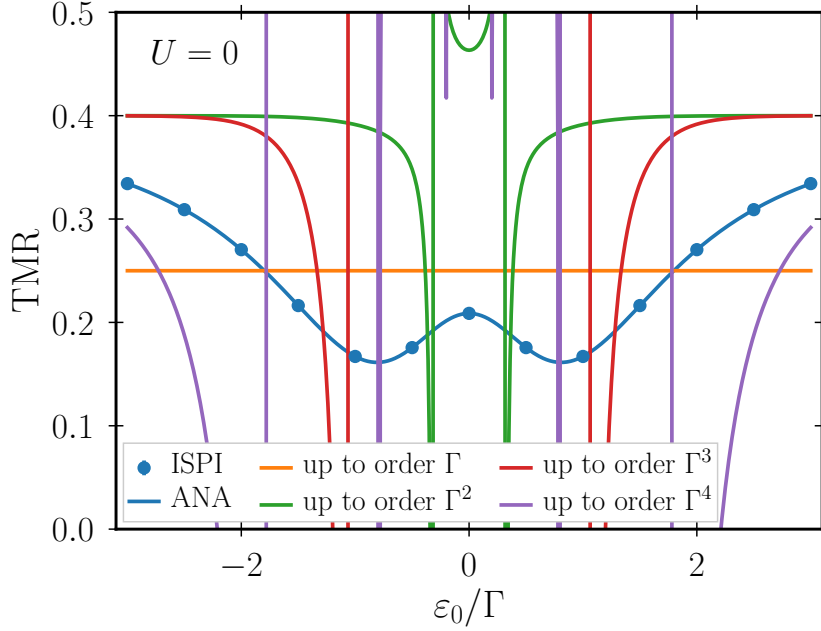


Figure 6.11: Gate voltage dependence of the TMR for the noninteracting case $U = 0$ at low temperatures $k_B T = 0.2\Gamma$ and low bias voltage $eV = 0.1\Gamma$. Comparison between the analytical results, ISPI data (symbols) and different orders of perturbation theory. The leads' polarization was set to $p = 0.5$ and no external magnetic field was applied $\mathbf{B} = 0$.

voltage is chosen close to the bifurcation point indicated in Fig. 6.10. The central maximum has just split into two local maxima, a finite Coulomb interaction U seems to wash out the fine structure visible for $U = 0$. Note that the limiting value of the TMR for $|\varepsilon_0| \gg \Gamma$ is again set by Julliere's value.

We complete the discussion of the gate-voltage dependence of the TMR with the remark that also for the case of finite U a first plus second order calculation fails completely at low temperatures. This is shown in Figs. 6.12(c) and (d), in which the same parameters as in Figs. 6.12(a) and (b) are used, respectively. Both datasets are plagued by severe and nonphysical divergences. They fail to reproduce the central maximum as well as the resulting minima. Just as before only Julliere's value is reproduced correctly at $|\varepsilon_0| \gg \Gamma$. However, perturbation theory predicts that the system reaches this value for all too small gate voltages ε_0 .

Finally, we study the bias-voltage dependence of the TMR at $\varepsilon_0 = 0$ and $k_B T = 0.2\Gamma$ for different values of the Coulomb interaction strength, see Fig. 6.13. Since the current is an antisymmetric function of the bias voltage V , the TMR is symmetric with respect to $V = 0$. For large bias voltages, the TMR approaches the value obtained for sequential tunneling, $\text{TMR} = p^2 = 0.25$ at $p = 0.5$. At $U = 0$ there is a well-pronounced local maximum in the center. Two local minima are placed symmetrically around the central peak. As U increases, the form of the TMR becomes modified. At the center (linear-response regime), the TMR first grows until

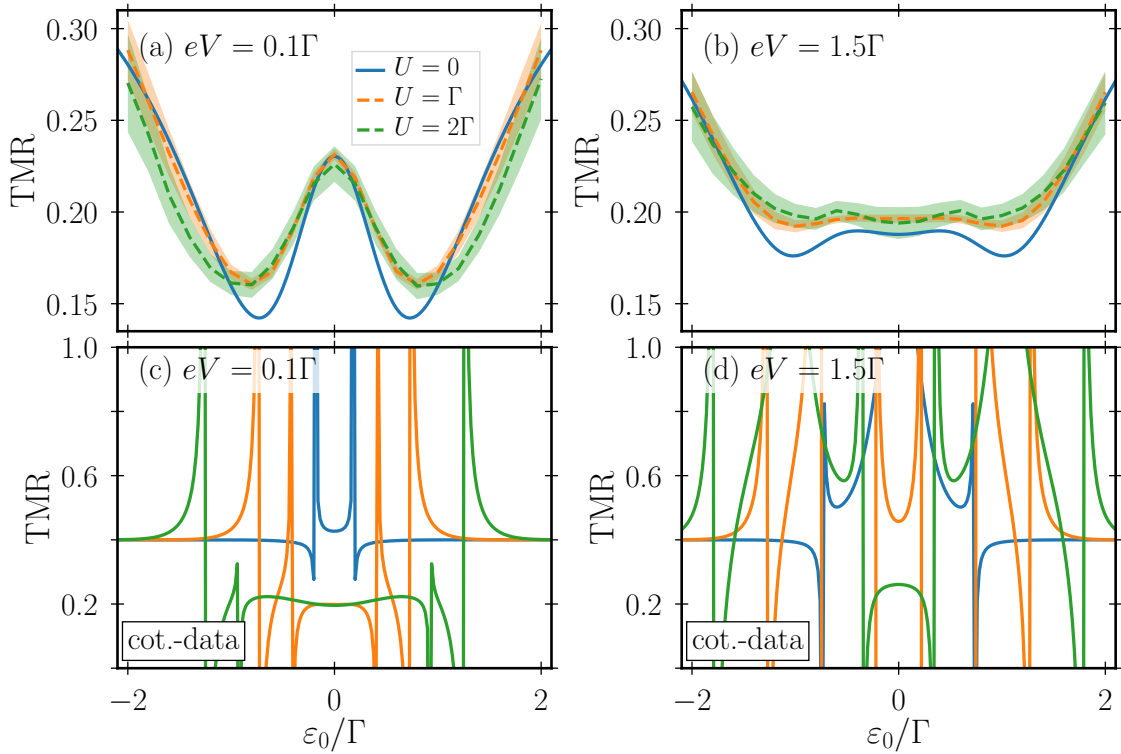


Figure 6.12: Gate-voltage dependence of the TMR for $U/\Gamma = 0, 1, 2$ and $k_B T = 0.1\Gamma$. The polarization is $p = 0.5$ and shaded areas represent error bars. The voltage is chosen to be (a), (c) in the linear-response regime $eV = 0.1\Gamma$, and (b), (d) slightly beyond the bifurcation point $eV = 1.5\Gamma$. In (c) and (d) we depict the results of a first plus second order calculation for the parameters of (a) and (b), respectively.

$U \approx \Gamma$ and then drops again. In the non-linear regime, $|eV| < \Gamma$, the interaction always increases the TMR. As a consequence the minima are getting washed out for $U > \Gamma$. The error bars indicate the increasing numerical challenge for increasing U , especially in the linear-response regime.

6.2.3 Summary

The TMR through a quantum-dot spin valve is a highly nontrivial function of temperature as well as gate and bias voltage. For negligible Coulomb interaction one is able to calculate the TMR analytically. In the limit of weak tunnel coupling, a perturbative treatment of tunneling including sequential or sequential plus cotunneling is possible. In a generic experimental scenario, however, the energy scales for charging energy, tunneling strength, and temperature are all of the same order of magnitude. As a result, neither neglecting interactions nor a perturbative treatment of tunneling is justified. In contrast, resonant-tunneling effects in the presence of finite Coulomb interactions are important for a proper, physical description of the

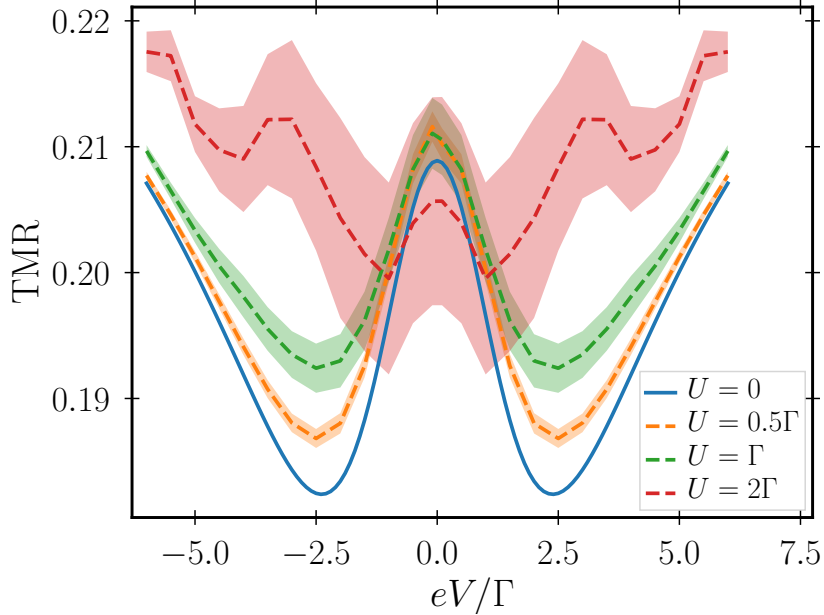


Figure 6.13: Bias-voltage dependence of the Tmr for $U/\Gamma = 0, 0.5, 1, 2$. The other parameters are $\varepsilon_0 = 0$, $k_B T = 0.2\Gamma$, and $p = 0.5$. Shaded areas represent depict error bars.

TMR. The ISPI technique provides reliable, numerically exact data that naturally includes tunneling contributions from all orders in the tunnel-coupling strength, which seems to be extremely important. For intermediate values of the charging energy, up to the same order of magnitude as the tunnel coupling strength, numerical convergence is achieved.

We have analyzed the temperature as well as the gate- and bias-voltage dependence of the TMR. We find that for $k_B T \lesssim \Gamma$ perturbation theory severely fails since resonant tunneling becomes important. The TMR displays a well-pronounced peak at $\varepsilon_0 = 0$ and $eV = 0$. We are able to clearly resolve this peak within our ISPI scheme and study the influence of a finite Coulomb interaction.

6.3 Noncollinearity and Zeeman field

We continue the discussion with the system being in an arbitrary, in general non-collinear setup and include a local Zeeman term on the quantum dot. A sketch of the setup is given in Fig. 6.14. We, again, choose the symmetric case, meaning that the lead polarizations are chosen such that $p_L = p_R = p$, whereas hybridization strengths are $\Gamma_L = \Gamma_R = \Gamma$ and the bias voltage is defined by $\mu_L = -\mu_R = eV/2$. The angle between the leads' magnetizations is $\theta_L = -\theta_R = \theta/2$, c.f. Eq. (3.10). As we are especially interested in resonant transport and spin effects, we choose $k_B T \ll \Gamma$ in the following. We have shown in the previous sections that a weak-

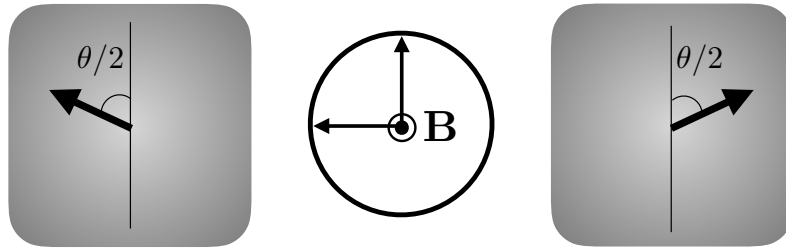


Figure 6.14: Noncollinear setup of the quantum-dot spin valve. The angle θ can be chosen arbitrary, the Zeeman field \mathbf{B} has arbitrary direction and strength.

coupling theory does not apply in this regime, while the ISPI method is able to give reliable predictions, once convergence is reached.

Once the temperature is lower than the system's Kondo temperature T_K , the quantum-dot spin valve shows a clear Kondo peak in the conductance at zero bias [131]. It was predicted that for the quantum-dot spin valve the Kondo peak is split even without an external magnetic field applied, which is caused by the exchange field emerging due to the spin-polarized leads [132, 133], which was verified experimentally [14, 28]. The magnitude and sign of this spin splitting can even be controlled via the gate voltage [134]. Throughout this work we study the quantum-dot spin valve in the mixed valence regime, where Kondo correlations should be present but not universal. As a consequence, we do not observe a Kondo peak within our data.

6.3.1 Interaction-Induced Current Asymmetry

For a start, we return to the parameters settings from Fig. 6.2(c), i.e. $k_B T = 0.2\Gamma$, $eV = 0.1\Gamma$ and $p = 0.5$, with the magnetization chosen noncollinearly, $\theta = \pi/2$. However, we now include ISPI calculations for Coulomb interaction strengths $0 \leq U \leq 2\Gamma$. For small bias voltages, i.e. the linear conductance regime, we find the results shown in Fig. 6.15(a). Spin degeneracy is lifted by the Zeeman field in z -direction, and in the absence of interactions $U = 0$, see blue solid line, we observe peaks at $\varepsilon_0 \approx \pm B_z/2$, as was discussed before already. Finite Coulomb interaction $U \neq 0$ renormalizes the peak positions, which are then located at $\varepsilon_0 \approx \pm(B_z + U)/2$. Additionally, the Coulomb interaction breaks the spin (particle-hole) symmetry, leading to an asymmetry in the gate voltage dependence of the conductance with respect to $\varepsilon_0 = 0$, i.e. $G(\varepsilon_0) \neq G(-\varepsilon_0)$. Strikingly, this asymmetry is modified with the Coulomb interaction strength and becomes more pronounced for increasing U . Especially, the heights of the peaks are affected: The conductance peak for $\varepsilon_0 > 0$, attributed to the spin $\sigma = \uparrow$ -channel is higher whereas its counterpart $\varepsilon_0 < 0$ for $\sigma = \downarrow$

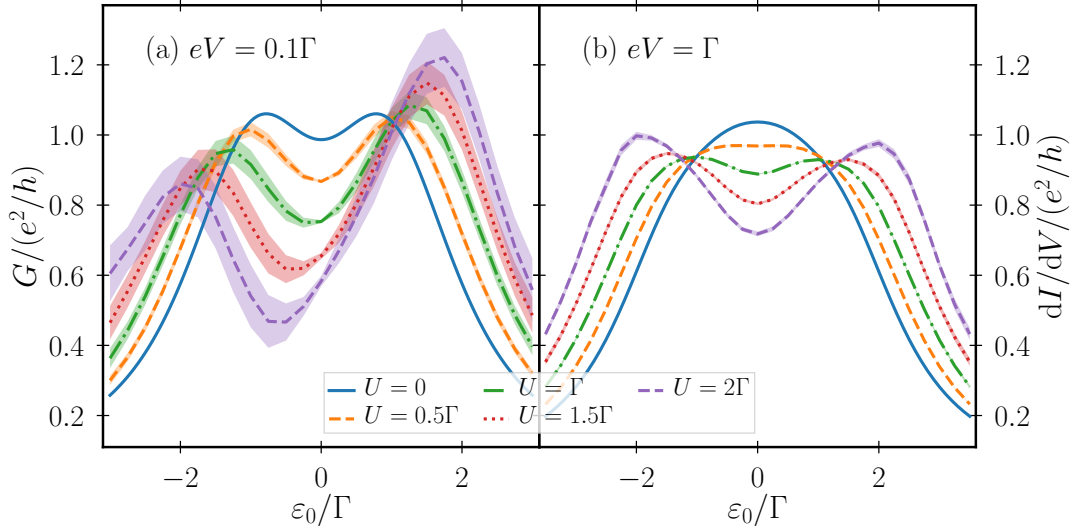


Figure 6.15: (a) Linear and (b) nonlinear differential conductance of the *interacting* spin valve as a function of gate voltage ε_0 for noncollinear lead magnetizations. An external Zeeman field of strength $B_z = 2\Gamma$ is applied in z -direction. Other parameters are $k_B T = 0.2\Gamma$, $\theta = \pi/2$, $p = 0.5$, and $eV = 0.1\Gamma$ in (a) and $eV = \Gamma$ in (b). Shaded areas are error estimates.

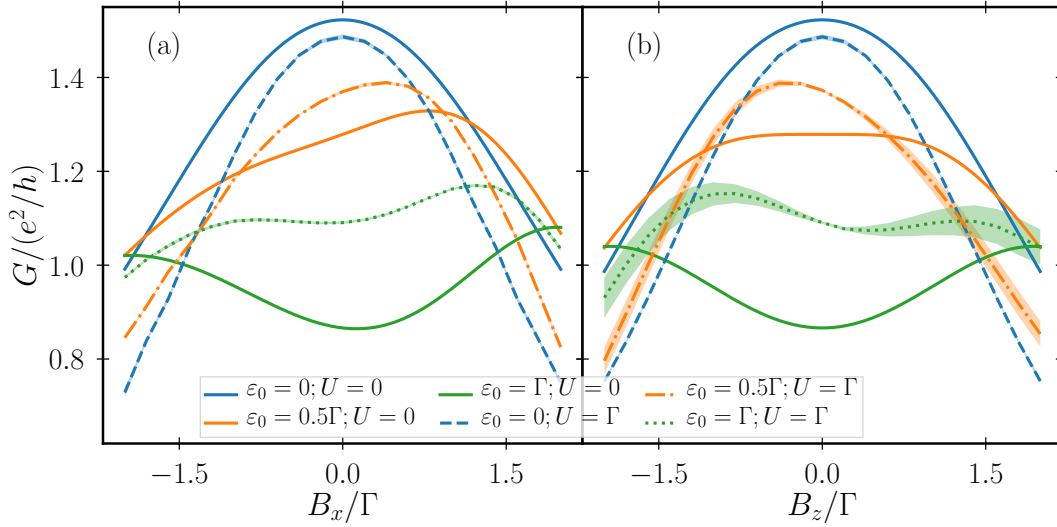


Figure 6.16: Linear conductance through the quantum-dot spin valve as a function of the magnetic field. The local magnetic field points in (a) x -direction and (b) z -direction. The noninteracting case and the interacting case, $U = \Gamma$ are compared for different gate voltages ε_0 . Other parameters are $k_B T = 0.2\Gamma$, $\theta = \pi/2$, $p = 0.5$, and $eV = 0.1\Gamma$. Shaded areas are error estimates.

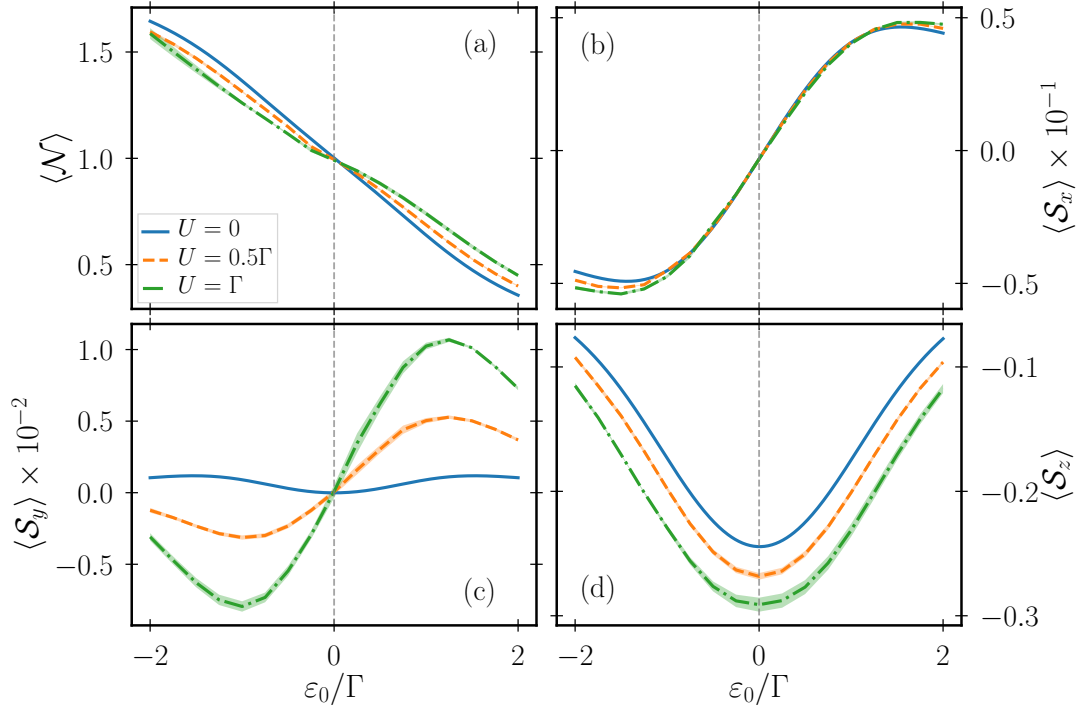


Figure 6.17: Occupation number and spin projections as a function of gate voltage ε_0 at different interaction strengths U in the linear response regime $eV = 0.1\Gamma$. Parameters are as in Fig. 6.15. Shaded areas are error estimates.

is suppressed. Since this effect vanishes for collinear lead magnetizations $\theta = (0, \pi)$ and for $U = 0$, we conclude it to be a spin-dependent, *interaction-induced* current asymmetry.

Turning to the nonequilibrium setup, i.e. $eV = \Gamma$, see Fig. 6.15(b) we note that the Zeeman splitting is smeared out by the finite bias voltage of comparable order as the Zeeman field, e.g. the blue solid curve for $U = 0$. Nevertheless, finite $U > 0$ lifts the spin degeneracy of the energy level and a splitting evolves for interaction strengths $U \geq \Gamma$. Again, with increasing Coulomb interaction strength, the asymmetry of the peak splitting increases. In comparison to the linear-response regime, the asymmetry-effect is less pronounced, probably due to the washing out of quantum effects at large bias voltages. However, in this generic regime where all energy scales are of the same order of magnitude, nonequilibrium and interaction effects should be treated on equal footing, as is possible with the ISPI method, in order to obtain a complete physical picture.

To further illustrate the appearance of the interaction-induced asymmetry, we show in Fig. 6.16 the linear conductance $G(B_x)$ in panel (a) and $G(B_z)$ in panel (b) for different gate voltages ε_0 and Coulomb interactions $U = 0$ and $U = \Gamma$. For $U = 0$ we reproduce the asymmetry properties, known from Fig. 6.2(a) and (c). In that case, when tuning B_z all curves are symmetric, i.e. left-right symmetry is intact,

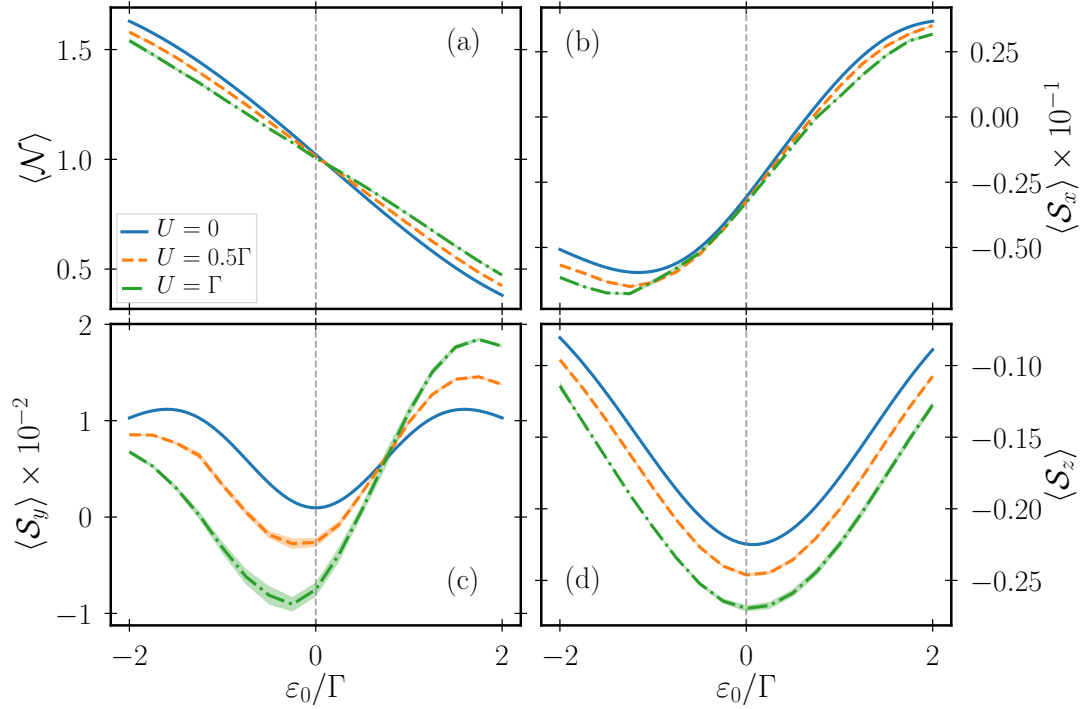


Figure 6.18: Same as Fig. 6.17 but in the nonequilibrium regime, $eV = \Gamma$.

while when tuning B_x we find asymmetric curves even for the noninteracting case, while the gate voltage is nonzero. The left-right symmetry is broken in this case by the different hybridization strengths for the two spin channels.

Finite Coulomb interaction strength U affects both cases. For one the conductance is suppressed, which is due to Coulomb blockade. Secondly, in both cases increasing the Coulomb interaction decreases the width of the curves and moves peaks closer together (in the case of $\varepsilon_0 = \Gamma$). This makes sense, since Coulomb interaction pushes the quantum dot's energy levels further apart, additionally to the magnetic field. As a result lower magnetic fields are necessary for a similar effect in the conductance. However, when tuning B_x , the Coulomb interaction does not significantly impact the asymmetry of the curve. When tuning B_z , on the other hand, Coulomb interaction serves to break left-right symmetry, and the conductance is sensitive to the sign of the magnetic field, resulting in asymmetric line shapes in the figure. Note that for $\varepsilon_0 = 0$ the particle-hole symmetric point is under investigation and as a result this case remains symmetric. Only when $\varepsilon_0 \neq 0$ we find that the particle-hole symmetry is broken and with it $G(B_z) \neq G(-B_z)$. The asymmetry in the two cases develops very differently. When tuning B_x we find a global maximum at $B_x/\Gamma \approx 1.3$, for $\varepsilon_0 = \Gamma$, while when tuning B_z the same case shows a global maximum at $B_z/\Gamma \approx -0.9$. This means while the general lineshapes seem similar, apart from a minus sign, there are significant quantitative differences.

In order to complete the picture, we discuss the spin projections and occupation number for the same cases as shown in Fig. 6.15. All four observables are shown

in Fig. 6.17(a)-(d) for the linear response regime $eV = 0.1\Gamma$ and in Fig. 6.18(a)-(d) for finite bias voltage $eV = \Gamma$. We find that $\langle \mathcal{S}_x \rangle$ and $\langle \mathcal{S}_z \rangle$ display a certain asymmetry, even in the noninteracting case, which is absent in the linear-response regime. Having a finite Coulomb interaction, the exchange field plays a role as well, i.e. an interaction-induced magnetic field which stems from inherent coherences of the system (cf. Sec. 1.1.2). The exchange field is generated by the Coulomb interaction and its orientation is determined by the direction of the leads' magnetizations. Of course its particular form and strength depend strongly on all other system parameters. Its impact on $\langle \mathcal{S}_{x,y,z} \rangle$ is visible when increasing the Coulomb interaction strength. The x - and z -components are barely affected qualitatively by the increasing Coulomb interaction, yet they are shifted towards more negative values in the respective expectation value, see panels (b) and (d) in Figs. 6.17 and 6.18. For the y -component, however, $U \neq 0$ changes the line shape significantly. While for the noninteracting case the y -component is suppressed at low bias voltages, Coulomb interactions introduce an additional, asymmetric contribution to the y -component (see Fig. 6.17(c)). With increasing eV the y -component is not suppressed anymore, see Fig. 6.18(c), and the effect of the asymmetric contribution becomes less relevant as a result.

6.3.2 Angular Dependence

Before, we only discussed three different angles between the leads' magnetizations, $\theta = 0, \pi/2, \pi$. Now we focus on the angular dependence of the different observables. Fig. 6.19 shows the linear conductance $G(\theta)/G(\theta = 0)$ for different values of the gate voltage ε_0 . We choose $U = 2\Gamma$, no external magnetic field is applied to the dot, and the other parameters are given by $k_B T = 0.2\Gamma$, $eV = 0.1\Gamma$. We compare data from a perturbative calculation performed in Ref. [27] with ISPI data. Note that the quantity $G(\theta)/G(0)$ is closely related to the TMR, in fact $\text{TMR} = 1 - G(\pi)/G(0)$. Of course, one could just as well define an angle-dependent TMR, $\text{TMR}(\theta) = 1 - G(\theta)/G(0)$. Due to the finite polarization p , all datasets have a pronounced minimum at $\theta = \pi$. Taking into account resonant tunneling effects, we observe that the minimal value varies strongly for different gate voltages ε_0 , such that $G(\theta)/G(0)|_{\varepsilon_0=\Gamma} < G(\theta)/G(0)|_{\varepsilon_0=0} < G(\theta)/G(0)|_{\varepsilon_0=3\Gamma}$. This behavior is consistent with our findings from Sec. 6.2.2. The results obtained via perturbation theory does not account this. However, in this data the impact of the exchange field is visible very clearly. While for $\varepsilon_0 = 0$ and $\varepsilon_0 = 3\Gamma$ the linear conductance shows a cosine-like behavior, the case $\varepsilon_0 = \Gamma$ deviates and the width is smaller. This effect is attributed to the exchange field. The cosine-like behavior is only reproduced for resonant tunneling when the gate voltage $\varepsilon_0 \gg \Gamma$. However, for small gate voltages, especially in the case of $\varepsilon_0 = 0$, resonant-tunneling results deviate significantly.

In Fig. 6.20 we present the effect that an external magnetic field has on the angular dependence of the linear conductance through the quantum-dot spin valve. In panel (a) we apply a local Zeeman field in x -direction and in panel (b) we apply it in z -direction. We compare different strengths of the magnetic field and different gate

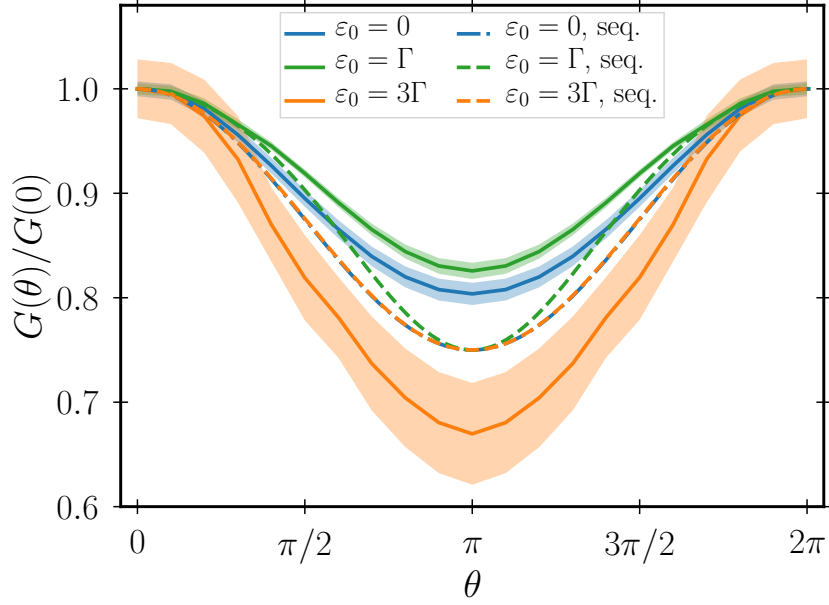


Figure 6.19: Linear conductance as a function the angle θ enclosed by the leads' magnetizations. We show ISPI data for different gate voltages ε_0 (shaded areas are error estimates) and compare it to results from sequential tunneling (denoted by the shorthand seq.). Parameters are $k_B T = 0.2\Gamma$, $eV = 0.1\Gamma$, $U = 2\Gamma$, $p = 0.5$ and $\mathbf{B} = 0$.

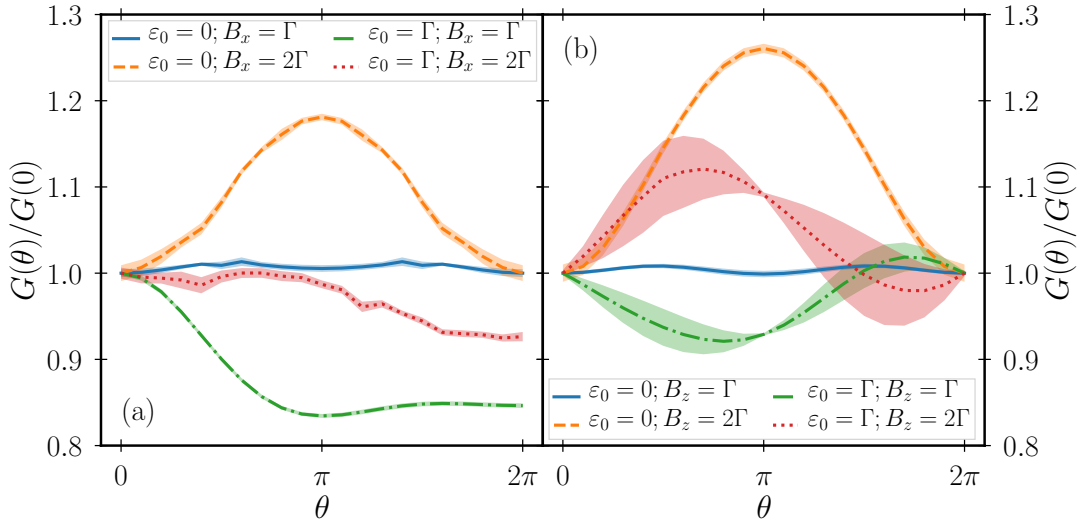


Figure 6.20: Impact of an external magnetic field on the angular dependence of the linear conductance through the quantum-dot spin valve. In panel (a) the external magnetic field points in x -direction, while in (b) it points in z -direction. Parameters are $k_B T = 0.2\Gamma$, $eV = 0.1\Gamma$, $U = \Gamma$, $p = 0.5$.

voltages. The other parameters are given by $k_B T = 0.2\Gamma$, $eV = 0.1\Gamma$, $U = \Gamma$ and $p = 0.5$. Comparing both panels with Fig. 6.19 it is obvious that due to the magnetic field the angular dependence of the linear conductance is changed drastically: The central minimum at $\theta = \pi$ is lost and replaced by a behavior that heavily depends on the strength and orientation of the magnetic field as well as the gate voltage. The case $\varepsilon_0 = 0$ is symmetric with respect to $\theta = \pi$ and there are only minor differences between the magnetic field pointing in x - or z -direction. At $B_{x/z} = \Gamma$ and $\varepsilon_0 = 0$ the linear conductance is almost constant, only small oscillations are visible. When increasing the magnetic field further to $B_{x/z} = 2\Gamma$ a maximum at $\theta = \pi$ develops, which is slightly higher when the magnetic field points in z -directions. Once $\varepsilon_0 \neq 0$, however, the direction of the magnetic field has a strong impact. When the magnetic field points in z -direction we find that the linear conductance oscillates and the symmetry with respect to $\theta = \pi$ is lost, which is only the case for $U \neq 0$. This effect is of course closely related to the asymmetry discussed in Fig. 6.15. If the magnetic field points in x -direction on the other hand (panel (b)), we find a very different picture. A striking new feature is that $G(0) \neq G(2\pi)$, which at first glance seems unintuitive. However, based on our choice of coordinate system (see Sec. 3.1), $\theta = 0$ means that the leads' magnetizations are aligned in $+x$ direction, while for $\theta = 2\pi$ they point in $-x$ direction. Since the magnetic field points along the x -axis it is very plausible that we find different values for the linear conductance. For $\theta = 4\pi$ the system then returns into the same state as for $\theta = 0$.

6.3.3 Summary

When studying a quantum-dot spin valve with noncollinear magnetized leads and subjecting the quantum dot to a local Zeeman field, we find an interaction-induced asymmetry in the current profile, when changing the gate voltage. The Zeeman field together with a small to intermediate Coulomb interaction produces asymmetric current line shapes, as the spin-symmetry together with left/right-symmetry is broken. We were able to trace back this asymmetry in the linear and differential conductance to the y -component of the spin projection, which is also strongly influenced by Coulomb interactions. As a result, we argue that the interaction-induced exchange field depends highly on resonant tunneling effects, leading to this strong asymmetry effect, that affects both the conductance and the spin projections of the quantum dot. This effect is most pronounced at small bias voltages, but does also survive a finite bias voltage that drives the system out of equilibrium, as long as resonant tunneling effects have an impact on the underlying physics.

We also discussed the conductance as a function of the angle between the leads' magnetizations and found significant differences between resonant and sequential tunneling, which are consistent with our earlier predictions of the TMR. When activating an external magnetic field, the angular dependence of the linear conductance becomes rather complicated and heavily depends on the strength of the magnetic field, its direction and the gate voltage.

7 Conclusions

The goal of this work has been to study spin-dependent, resonant transport through an interacting quantum-dot spin valve in the generic regime where all energy scales are of the same order of magnitude. For this we expanded the technique of iterative summations of path integrals in three ways: We implemented spin-dependent processes within the technique, we showed that it is possible to calculate the quantum dot's occupation number and spin projection in addition to the current as observable using the ISPI technique, and we proposed a mapping of the ISPI technique itself to a transfer matrix approach.

In Chapter 3 we introduced the Hamiltonian of the quantum-dot spin valve and described it in detail. The system is comprised from a central, single-level quantum dot, that is tunnel-coupled to two Stoner ferromagnets and contacted capacitively by a gate electrode. For the quantum-dot we employed the Anderson impurity model. We demonstrated how spin-dependent tunneling is established and controlled via the magnetization directions of the leads and their respective polarization strength. Using a nonequilibrium Green functions approach, we derived an analogue to the Meir-Wingreen formula for the noninteracting quantum-dot spin valve. In addition, we derived analytic solutions for the quantum dot's occupation number and spin projection, again, for the noninteracting setup. Due to the smallness of the central quantum dot, a noninteracting solution is not sufficient to describe the transport properties of the setup in a quantitative or qualitative manner. A number of different approaches have been employed to tackle this problem, one of them being the ISPI technique. To allow a classification of this method, we compared it at the end of the chapter with perturbative approaches in the Coulomb interaction U and in the hybridization strength Γ , as well as with numerically exact methods, namely quantum Monte Carlo simulations and renormalization group approaches. We argued that the ISPI technique is a unique approach that excels in the generic parameter regime where all energy scales are of the same order of magnitude. As a result, the ISPI technique can act as a bridge, connecting the regimes of applicability of the other methods.

In Chapter 4 we demonstrated how one is able to calculate the system's partition function using a path-integral ansatz. To allow a treatment of the Hamiltonian's quartic interaction term within this approach, we decoupled this term using a Hubbard-Stratonovich transformation, which introduces one Ising-like Hubbard-Stratonovich spin per time step. The result is a formula for the partition function, where it is necessary to sum over all configurations of the Hubbard-Stratonovich spins. This is an impossible task, and the point where the ISPI method is applied. Finally, we showed how one is able to purposefully break time-translation invari-

ance by including a source term within the partition function, transforming it into a generating functional. The logarithmic derivative of this generating functional enabled us to calculate the expectation values of the current, occupation number and components of the spin projection via a fitting source term.

We introduced the ISPI technique in Chap. 5. Since lead-induced correlations decay exponentially with time, we were motivated to truncate these correlations after some memory time, which is the main approximation of the ISPI method. One then is able to construct an iteration scheme, where the number of Hubbard-Stratonovich spins over which one has to sum per iteration step is reduced significantly. Via a convergence procedure we were able to reach numerically exact data for the current as well as the occupation number and spin projection. We also proposed a direct mapping of the ISPI technique to a transfer-matrix approach, leading to the transfer-matrix implementation of the ISPI technique. This implementation and the standard finite-time implementation complement one another. To calculate the stationary limit of observables, the transfer-matrix implementation reduces calculation times, as we have shown when testing the performance of the two implementations. In addition, the transfer-matrix formulation may be suited to allow calculation of non-time-local observables within the ISPI technique.

In Chap. 6 we presented our results for the resonant transport through quantum-dot spin valves. We started with an extensive benchmark of the ISPI technique, comparing its results with those of the noninteracting solution derived before, as well as to results from a sequential and a sequential plus cotunneling approach. We found perfect agreement between ISPI and the noninteracting solution, and showed that for large temperatures ISPI reproduces the results from the perturbative method. Also, we compared results from the finite-time implementation with those from the transfer-matrix implementation and, again, found a perfect agreement between the two.

In a next step we studied the TMR for the interacting quantum-dot spin valve and found that it shows a highly nontrivial behavior as a function of the temperature as well as the gate and bias voltage. We also were able to demonstrate that to describe low-temperature features of the TMR a perturbation theory in the hybridization Γ severely fails, while ISPI produces reliable data.

Finally, we discussed the effects of noncollinear leads combined with a local magnetic field acting on the dot. We found that magnetic fields may introduce asymmetry in the current as a function of gate voltage. Such an asymmetry is already visible for the noninteracting setup, when the magnetic field points in x -direction. However, this effect can be understood in a rather straightforward manner by spin-dependent couplings. The interplay between Coulomb interaction, noncollinear leads and a magnetic field creates an additional asymmetry effect, whose origin is much less obvious. We were able to track it down to the fact that the interplay between these three constituents, has a significant effect on the y -component of the spin projection, which causes the effect in the current.

A Infinite Order Expansion

The formalism of nonequilibrium Green functions introduced in Sec. 2.2 proves particularly useful for perturbative approaches. Via an expansion in the tunneling Hamiltonian up to infinite order it is possible to give a formula for the *dressed Green function* $\mathbf{G}_{\sigma\sigma'}$, called the Dyson equation. In addition, we derive a formula, again via infinite order expansion, for the *mixed Green function* $\mathbf{G}_{\sigma,\alpha\mathbf{k}\tau}$, which is necessary in Sec. 3.2 where we derived the current through the noninteracting quantum-dot spin valve. We can think of these Green functions as being built from simple parts, namely the Green function of the free quantum dot $\mathbf{G}_{0,\sigma\sigma'}$, the Green function of lead α , $\mathbf{g}_{\alpha\mathbf{k},\tau\tau'}$, and the tunneling vertices $Y_{\alpha,\tau\sigma}$, $Y_{\alpha,\sigma\tau}^*$. The free Green functions denote propagation of the system in time, while the tunneling vertices present tunneling between dot and leads.

For an easy notation of the expansion a diagrammatic representation has proven very useful and is widely used in literature [33, 68, 135]. To use it, we introduce the diagrammatic representations of the different building blocks in energy space

$$\mathbf{G}_{\sigma\sigma'}(\omega) = \begin{array}{c} \sigma \\ \bullet \rightleftarrows \bullet \\ \sigma' \end{array}, \quad \mathbf{G}_{\sigma\sigma'}^0(\omega) = \begin{array}{c} \sigma \\ \bullet \leftarrow \bullet \\ \sigma' \end{array}, \quad \mathbf{g}_{\alpha\mathbf{k},\tau\tau'}(\omega) = \begin{array}{c} \alpha\mathbf{k}\tau \\ \bullet \text{---}\leftarrow\text{---}\bullet \\ \alpha\mathbf{k}\tau' \end{array} \quad (\text{A.1})$$

$$Y_{\alpha,\tau\sigma} = \begin{array}{c} \times \\ \alpha\mathbf{k}\tau \quad \sigma \end{array}, \quad Y_{\alpha,\sigma\tau}^* = \begin{array}{c} \times \\ \sigma \quad \alpha\mathbf{k}\tau \end{array}$$

In addition it is very useful to define the irreducible self energy in the diagrammatic representation. Translating Eq. (3.31) into diagrams leads to

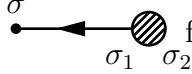
$$\Sigma_{\sigma\sigma'}(\omega) \equiv \begin{array}{c} \textcircled{\times} \\ \sigma \quad \sigma' \end{array} = \begin{array}{c} \times \text{---}\leftarrow\text{---}\times \\ \sigma \quad \alpha\mathbf{k}\tau \quad \alpha\mathbf{k}\tau' \quad \sigma' \end{array} \quad (\text{A.2})$$

We note that when connecting different diagrams, it is understood that all intermediate degrees of freedom are summed.

Dressed Green function Having defined all necessary basic building blocks, we are able to build a perturbation expansion of the dressed Green function by adding up all possible diagrams. The result takes the following form

$$\begin{array}{c} \sigma \\ \bullet \rightleftarrows \bullet \\ \sigma' \end{array} = \begin{array}{c} \sigma \\ \bullet \leftarrow \bullet \\ \sigma' \end{array} + \begin{array}{c} \sigma \\ \bullet \leftarrow \textcircled{\times} \leftarrow \bullet \\ \sigma_1 \quad \sigma_2 \end{array} + \begin{array}{c} \sigma \\ \bullet \leftarrow \textcircled{\times} \leftarrow \textcircled{\times} \leftarrow \bullet \\ \sigma_1 \quad \sigma_2 \quad \sigma_3 \quad \sigma_4 \end{array} + \dots \quad (\text{A.3})$$

It is important to note that we already employed the linked cluster theorem, which states that non-connected diagrams cancel exactly, leaving only above connected

diagrams [33]. The factor $\frac{1}{n!}$, which one would expect from a Taylor series is compensated by permutations of the intermediate states. On the right hand side we are able to bracket  from the second term onwards, leading to the following expression

$$\begin{aligned}
 \text{diagram} &= \text{diagram} + \text{diagram} \times \left(\text{diagram} + \text{diagram} + \dots \right) \\
 &= \text{diagram} + \text{diagram},
 \end{aligned} \tag{A.4}$$

where in the last step we made use of the fact that this expansion is indeed infinite. The last line is then the famous Dyson equation in its diagrammatic formulation. If we translate it back, replacing the diagrams with their respective formulas, we find

$$\mathbf{G}_{\sigma\sigma'}(\omega) = \mathbf{G}_{\sigma\sigma'}^0(\omega) + \sum_{\sigma_1, \sigma_2} \mathbf{G}_{\sigma\sigma_1}^0(\omega) \mathbf{\Sigma}_{\sigma_1\sigma_2}(\omega) \mathbf{G}_{\sigma_2\sigma'}(\omega). \tag{A.5}$$

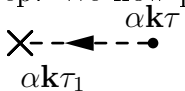
This equation may be solved easily, obtaining the following result for the dressed Green function in matrix notation

$$\hat{\mathbf{G}}(\omega) = \left[\left(\hat{\mathbf{G}}_0(\omega) \right)^{-1} - \hat{\mathbf{\Sigma}}(\omega) \right]^{-1}. \tag{A.6}$$

Mixed Green Function The mixed Green function $\mathbf{G}_{\sigma, \alpha\mathbf{k}\tau}$, introduced during the derivation of the noninteracting current, see Eq. (3.16), can be derived in a similar fashion. Since the creation and annihilation operators for this mixed Green function are from both the quantum dot and the leads, the propagator has to start in lead α and end on the quantum dot. As a result tunnel vertices are necessary explicitly for the expansion

$$\mathbf{G}_{\sigma, \alpha\mathbf{k}\tau} = \text{diagram} + \text{diagram} + \dots \tag{A.7}$$

$$= \text{diagram} + \text{diagram} + \dots, \tag{A.8}$$

where we reintroduced the self energy in the second step. We now proceed similar to the derivation of the Dyson equation by bracketing  from all terms, leading to

$$\begin{aligned}
 \mathbf{G}_{\sigma, \alpha\mathbf{k}\tau} &= \left(\text{diagram} + \text{diagram} + \dots \right) \times \text{diagram} \\
 &= \text{diagram}
 \end{aligned} \tag{A.9}$$

The last line is then our final result, which we can again translate back, leading to the exact formula used during Sec. 3.2

$$\mathbf{G}_{\sigma, \alpha k \tau} = \sum_{\sigma_1, \tau_1} \mathbf{G}_{\sigma \sigma_1}(\omega) Y_{\alpha, \sigma_1 \tau_1}^* \mathbf{g}_{\alpha k, \tau_1 \tau}(\omega). \quad (\text{A.10})$$

B Master Equation Approach

Assuming that the quantum dot is only weakly coupled to the leads, one is able to understand the tunneling as a perturbation and expand in orders of the tunneling Hamiltonian. We used results from this approach throughout Secs. 6.1 and 6.2 to compare our ISPI data with them. Here, we demonstrate how observables are calculated using a first-order expansion with respect to the tunneling Hamiltonian. For this *sequential tunneling* approximation, it is assumed that the coupling to the leads is weak enough such that the time between tunneling events is the largest time scale in our system. This method has proven very popular and is used successfully for many different problems, e.g. [33, 97, 121, 136].

We start by discussing the results obtained when only incoherent processes contribute to the tunneling. The quantum dot is in one of the following states $|0\rangle$, $|\uparrow\rangle$, $|\downarrow\rangle$, $|d\rangle$, which denote the unoccupied state, a state where it is occupied by a particle with spin up or down or doubly occupied, respectively. Employing Fermi's golden rule, transitions between these states due to tunneling through the left (L) or right (R) junction are governed by the matrix elements [33]

$$\Omega_{\alpha\beta}^{\text{L/R}} = 2\pi \sum_{f_\beta, i_\alpha} |\langle f_\beta | \mathcal{H}_{\text{T,L/R}} | i_\alpha \rangle|^2 W_{i_\alpha} \delta(E_{f_\beta} - E_{i_\alpha}), \quad (\text{B.1})$$

where i_α denotes the initial configuration of the internal degrees of freedom of state α , and f_β is the final configuration of the degrees of freedom of state β . We sum over all of these degrees of freedom, and weigh them by a thermal distribution function W_{i_α} , which is in our case the Fermi function $f(E_{i_\alpha})$. Since we used a symmetric setup throughout this thesis, the transition rates for the left and right junction are also chosen equal $\Omega_{\alpha\beta}^{\text{L}} = \Omega_{\alpha\beta}^{\text{R}} = \Omega_{\alpha\beta}$. With the transition rates being known, we are able to write down the master equations. These are kinetic equations that describe the dynamical behavior of the distribution function P_α .

$$\frac{d}{dt} P_\alpha = - \sum_{\beta} \Omega_{\beta\alpha} P_\alpha + \sum_{\beta} \Omega_{\alpha\beta} P_\beta. \quad (\text{B.2})$$

This equation allows a direct interpretation: The first term represents the rate of decay of state α , via processes that start in state α and end in any other state β . The second term is then the rate of opposite processes, which start in an arbitrary state of the system and end in the state α . In this work we only discussed the steady

state, where $\frac{d}{dt}P_\alpha = 0$, which means

$$0 = \begin{pmatrix} -(\Omega_{\uparrow 0} + \Omega_{\downarrow 0}) & \Omega_{0\uparrow} & \Omega_{0\downarrow} & 0 \\ \Omega_{\uparrow 0} & -(\Omega_{0\uparrow} + \Omega_{d\uparrow}) & 0 & \Omega_{\uparrow d} \\ \Omega_{\downarrow 0} & 0 & -(\Omega_{0\downarrow} + \Omega_{d\downarrow}) & \Omega_{\downarrow d} \\ 0 & \Omega_{d\uparrow} & \Omega_{d\downarrow} & -(\Omega_{\uparrow d} + \Omega_{\downarrow d}) \end{pmatrix} \begin{pmatrix} P_0 \\ P_\uparrow \\ P_\downarrow \\ P_d \end{pmatrix}, \quad (\text{B.3})$$

where it is understood that $\sum_\alpha P_\alpha = 1$. Once the different P_α are calculated using the equation above, the current can be obtained from the expression [33, 137]

$$I = -e \sum_N (\Omega_{N+1N} - \Omega_{N-1N}) P(N). \quad (\text{B.4})$$

Eq. (B.3) treats tunneling in and out of the dot incoherently. However, for the quantum-dot spin valve coherences are crucial even in a sequential approximation. This is already visible from the reduced density matrix, which for the quantum-dot spin valve takes the following form [27]

$$\rho_{\text{dot}} = \begin{pmatrix} P_0 & 0 & 0 & 0 \\ 0 & P_\uparrow & P_\uparrow^\downarrow & 0 \\ 0 & P_\downarrow^\uparrow & P_\downarrow & 0 \\ 0 & 0 & 0 & P_d \end{pmatrix}. \quad (\text{B.5})$$

The off-diagonal elements immediately prove that coherences are taken into account. It proves very much useful to define the components of the vector of average spin \mathbf{S} via

$$S_x = \frac{P_\uparrow^\downarrow + P_\downarrow^\uparrow}{2}; \quad S_y = \frac{P_\uparrow^\downarrow - P_\downarrow^\uparrow}{2}; \quad S_z = \frac{P_\uparrow - P_\downarrow}{2}. \quad (\text{B.6})$$

as well as $P_1 = P_\uparrow + P_\downarrow$. This way the dot state is characterized by the set of parameters $(P_0, P_1, P_2, S_x, S_y, S_z)$. As a consequence we require six first order master equations, where the first three are given by [27]

$$\begin{aligned} \frac{d}{dt} \begin{pmatrix} P_0 \\ P_1 \\ P_2 \end{pmatrix} &= \sum_{\alpha=L,R} \Gamma \begin{pmatrix} -2f_\alpha^+(E_0) & f_\alpha^-(E_0) & 0 \\ 2f_\alpha^+(E_0) & -f_\alpha^-(E_0 + U) & 2f_\alpha^-(E_0 + U) \\ 0 & f_\alpha^+(E_0 + U) & -2f_\alpha^-(E_0 + U) \end{pmatrix} \begin{pmatrix} P_0 \\ P_1 \\ P_2 \end{pmatrix} \\ &+ \sum_{\alpha=L,R} 2p\Gamma \begin{pmatrix} f_\alpha^-(E_0) \\ -f_\alpha^-(E_0) + f_\alpha^+(E_0 + U) \\ -f_\alpha^+(E_0 + U) \end{pmatrix} \mathbf{S} \cdot \hat{\mathbf{n}}_\alpha, \end{aligned} \quad (\text{B.7})$$

where $f_\alpha^+(\omega)$ is the Fermi function and $f_\alpha^-(\omega) = 1 - f_\alpha^+(\omega)$. The energy E_0 was introduced in Sec. 3.1 and is defined as $E_0 = \varepsilon_0 - U/2$. The second three master equations are concerned with the evolution of the spin, and are given by

$$\frac{d\mathbf{S}}{dt} = \left(\frac{d\mathbf{S}}{dt} \right)_{\text{acc}} + \left(\frac{d\mathbf{S}}{dt} \right)_{\text{rel}} + \left(\frac{d\mathbf{S}}{dt} \right)_{\text{rot}} \quad (\text{B.8})$$

with

$$\left(\frac{d\mathbf{S}}{dt}\right)_{\text{acc}} = \sum_{\alpha=L,R} p\Gamma \left[f_{\alpha}^{+}(E_0)P_0 + \frac{-f_{\alpha}^{-}(E_0) + f_{\alpha}^{+}(E_0 + U)}{2}P_1 - f_{\alpha}^{-}(E_0 + U)P_d \right] \hat{\mathbf{n}}_{\alpha} \quad (\text{B.9})$$

$$\left(\frac{d\mathbf{S}}{dt}\right)_{\text{rel}} = \sum_{\alpha=L,R} \Gamma [f_{\alpha}^{-}(E_0) + f_{\alpha}^{+}(E_0 + U)] \mathbf{S} \quad (\text{B.10})$$

$$\left(\frac{d\mathbf{S}}{dt}\right)_{\text{rot}} = \mathbf{S} \times \sum_{\alpha=L,R} \mathbf{B}_{\alpha}, \quad (\text{B.11})$$

where \mathbf{B}_{α} is the exchange field from lead α . From this we see that the three parts that affect the change of the quantum dot's average spin are accumulation processes, which depends on the occupation probabilities, relaxation processes, which account for the decay of the dot spin, and rotation processes, caused by the exchange field, which causes precession of the spin. For a detailed discussion of the derivation of these formulas and their results, we refer to Ref. [27].

C Inverse Keldysh Rotation

We derive Eq. (4.30), starting with the Green function in the rotated basis from Eq. (2.18). To reach this basis we made use of the involutory transformation matrix

$$\mathbf{U} = \frac{1}{\sqrt{2}} \begin{pmatrix} 1 & 1 \\ 1 & -1 \end{pmatrix} \quad (\text{C.1})$$

and followed the convention from Larkin and Ovchinnikov [60]

$$\begin{pmatrix} g_{\alpha\mathbf{k}}^R & g_{\alpha\mathbf{k}}^K \\ 0 & g_{\alpha\mathbf{k}}^A \end{pmatrix} = \mathbf{U} \begin{pmatrix} g_{\alpha\mathbf{k}}^T & g_{\alpha\mathbf{k}}^< \\ g_{\alpha\mathbf{k}}^> & g_{\alpha\mathbf{k}}^T \end{pmatrix} \kappa_z \mathbf{U}. \quad (\text{C.2})$$

To return to the initial basis we revert the rotation. For this we make use of the fact that \mathbf{U} is involutory, $\mathbf{U} = \mathbf{U}^{-1}$. As a result, we find the following expression for the reverse Keldysh rotation

$$\mathbf{U} \begin{pmatrix} g_{\alpha\mathbf{k}}^R & g_{\alpha\mathbf{k}}^K \\ 0 & g_{\alpha\mathbf{k}}^A \end{pmatrix} \mathbf{U} \kappa_z = \frac{1}{2} \begin{pmatrix} g_{\alpha\mathbf{k}}^A + g_{\alpha\mathbf{k}}^R + g_{\alpha\mathbf{k}}^K & g_{\alpha\mathbf{k}}^A - g_{\alpha\mathbf{k}}^R + g_{\alpha\mathbf{k}}^K \\ -g_{\alpha\mathbf{k}}^A + g_{\alpha\mathbf{k}}^R + g_{\alpha\mathbf{k}}^K & -g_{\alpha\mathbf{k}}^A - g_{\alpha\mathbf{k}}^R + g_{\alpha\mathbf{k}}^K \end{pmatrix}. \quad (\text{C.3})$$

The advanced and retarded Green functions of the free lead are well known, see Eq. (3.20). We therefore are left with finding a formula to describe the Keldysh Green function $g_{\alpha\mathbf{k}}^K$ in terms of $g_{\alpha\mathbf{k}}^R$ and $g_{\alpha\mathbf{k}}^A$. For this we start with the definition of $g_{\alpha\mathbf{k}}^K$

$$g_{\alpha\mathbf{k}}^K = -i \langle [\mathcal{C}_{\alpha\mathbf{k}}, \mathcal{C}_{\alpha\mathbf{k}}^\dagger] \rangle = g_{\alpha\mathbf{k}}^> + g_{\alpha\mathbf{k}}^< = -2\pi i (1 - 2f_\alpha(\omega)) \delta(\omega\sigma_0 - \mathcal{E}_{\alpha\mathbf{k}}). \quad (\text{C.4})$$

Since $g_{\alpha\mathbf{k}}^R - g_{\alpha\mathbf{k}}^A = -2\pi i \delta(\omega\sigma_0 - \mathcal{E}_{\alpha\mathbf{k}})$, we are able to plug this into the equation above, finding

$$g_{\alpha\mathbf{k}}^K = (1 - 2f_\alpha(\omega))(g_{\alpha\mathbf{k}}^R - g_{\alpha\mathbf{k}}^A), \quad (\text{C.5})$$

which is the desired result. Plugging this back into Eq. (C.3), we find the expression

$$g_{\alpha\mathbf{k}} = \begin{pmatrix} g_{\alpha\mathbf{k}}^R & 0 \\ 0 & -g_{\alpha\mathbf{k}}^A \end{pmatrix} + (g_{\alpha\mathbf{k}}^A - g_{\alpha\mathbf{k}}^R) \begin{pmatrix} f_\alpha(\omega) & f_\alpha(\omega) \\ f_\alpha(\omega) - 1 & f_\alpha(\omega) \end{pmatrix}. \quad (\text{C.6})$$

We stop short to note that Eq. (C.5) can be rewritten, using the identity $f(x) = \frac{1}{2} - \frac{1}{2} \tanh \frac{\beta x}{2}$ leading to the fluctuation-dissipation theorem for fermions

$$g_{\alpha\mathbf{k}}^K = \tanh \frac{\beta(\omega - \mu_\alpha)}{2} (g_{\alpha\mathbf{k}}^R - g_{\alpha\mathbf{k}}^A), \quad (\text{C.7})$$

which is a generic relation for systems in equilibrium.

D Fourier Transformation of the Tunneling Self-Energies

With Eq. (4.44) we derived a formula for the generating functional, that is based on the sum of determinants of the dressed Green function Δ plus the source self energy $\eta\Sigma_S$ and the charging self energy Σ_C over all configurations of the Hubbard-Stratonovich spins. Since the theory is formulated time-discretely, they all are matrices in time. For Σ_C we derived its time representation in Eq. (4.38), the same is true for $\eta\Sigma_S$ for occupation number and spin components (see Eq. (4.55)). However, for the dressed Green function, we only derived a formula in energy space and found that it is defined in accordance to the Dyson equation (Eqs. (4.34)). For the source self energy of the current we found that it is given by the difference of parts of the tunneling self energy, for which we only have a formula in energy space, too (Eqs. (4.48) and (A.6)). Consequently, it is necessary to Fourier transform these two building blocks, which can be either done via a discrete Fourier transformation or analytically using residue theorem. The latter is what we want to show here.

Current Source Self Energy We start our discussion with the Fourier transformation of the current's source self energy. We start with the tunneling self energy Eq. (4.32) which we Fourier transform to build the source self energy for the current. First we make use of the identity for the Fermi function $f_\alpha(\omega) \equiv f(\omega - \mu_\alpha) = 1 - f(-\omega + \mu_\alpha)$. Applying this to Eq. (4.32) we get

$$\Sigma_{T,\alpha}(\omega) = \frac{i}{2} \begin{pmatrix} f(\omega - \mu_\alpha) - f(-\omega + \mu_\alpha) & -2f(\omega - \mu_\alpha) \\ 2f(-\omega + \mu_\alpha) & f(\omega - \mu_\alpha) - f(-\omega + \mu_\alpha) \end{pmatrix} \otimes \hat{\Gamma}_\alpha, \quad (\text{D.1})$$

with $\hat{\Gamma}_\alpha$ being defined as in Eq. (3.24). As a result, we are left with Fourier transforming $f(\omega - \mu_\alpha)$ and $f(-\omega + \mu_\alpha)$. We present the calculation in detail here

$$\int_{-\infty}^{\infty} d\omega e^{-i\omega t} f(\omega - \mu_\alpha) = \int_{-\infty}^{\infty} d\omega \frac{e^{-i\omega t}}{1 + e^{\beta(\omega - \mu_\alpha)}} = \lim_{\eta \rightarrow 0} \int_{-\infty}^{\infty} d\omega \frac{e^{-i\omega t} e^{\eta\omega}}{1 + e^{\beta(\omega - \mu_\alpha)}}, \quad (\text{D.2})$$

where we introduced an exponential cut-off with the small parameter $\eta > 0$. This is necessary to ensure that the integral remains finite. Next we employ the substitution $x = \omega - \mu_\alpha$ leading to

$$\begin{aligned} \int_{-\infty}^{\infty} d\omega e^{-i\omega t} f(\omega - \mu_\alpha) &= \lim_{\eta \rightarrow 0} \int_{-\infty}^{\infty} dx \frac{e^{-i(x+\mu_\alpha)t} e^{\eta(x+\mu_\alpha)}}{1 + e^{\beta x}} \\ &= \lim_{\eta \rightarrow 0} e^{-i\mu_\alpha(t+i\eta)} \int_{-\infty}^{\infty} dx \frac{e^{-ix(t+i\eta)}}{1 + e^{\beta x}}. \end{aligned} \quad (\text{D.3})$$

This integral is solveable analytically leading to the final result of the Fourier transformation of $f(\omega - \mu_\alpha)$

$$\begin{aligned} \int_{-\infty}^{\infty} d\omega e^{-i\omega t} f(\omega - \mu_\alpha) &= \lim_{\eta \rightarrow 0} e^{-i\mu_\alpha(t+i\eta)} \frac{i\pi}{\beta \sinh\left(\frac{\pi}{\beta}(t+i\eta)\right)} \\ &= \begin{cases} \frac{\pi}{\delta_t} + \mu_\alpha & \text{if } t = 0 \\ e^{-i\mu_\alpha t} \frac{i\pi}{\beta \sinh\left(\frac{\pi}{\beta}t\right)} & \text{otherwise,} \end{cases} \end{aligned} \quad (\text{D.4})$$

where δ_t is the stepsize of the time-discretization, which appears due to $\delta(t - t') = \frac{\delta_{tt'}}{\delta_t}$. The Fourier transformation of $f(-\omega + \mu_\alpha)$ is performed accordingly, the only difference is that the cut-off parameter has to be chosen such that $\eta < 0$, leading to

$$\int_{-\infty}^{\infty} d\omega e^{-i\omega t} f(-\omega + \mu_\alpha) = \begin{cases} \frac{\pi}{\delta_t} - \mu_\alpha & \text{if } t = 0 \\ -e^{-i\mu_\alpha t} \frac{i\pi}{\beta \sinh\left(\frac{\pi}{\beta}t\right)} & \text{otherwise.} \end{cases} \quad (\text{D.5})$$

One now only has to plug this back into Eq. (D.1) and has found an expression for the tunneling self-energy in time space, with which one is able to calculate the current's source self energy, via Eq. (4.52).

Dressed Green function We now turn to the Fourier transformation of the dressed Green function $\Delta(\omega) = (G_0^{-1}(\omega) - \sum_\alpha \Sigma_{T,\alpha}(\omega))^{-1}$. Since the elements of $\Delta(\omega)$ are rather lengthy, due to the inversion, we only describe the procedure in general, which can then be applied to each of the elements. We first note that all elements have the following structure

$$\Delta_{\sigma\sigma'}^{\nu\nu'}(\omega) = A(\omega) + B(\omega)f_L(\omega) + C(\omega)f_R(\omega), \quad (\text{D.6})$$

where the coefficients $A(\omega)$, $B(\omega)$ and $C(\omega)$ are prefactors that can depend on the different system parameters. These parts are Fourier transformed separately, using Residue theorem. For this one determines the roots of the coefficients' denominators and sorts them by the sign of their imaginary part. According to Ref. [138], one is then able to calculate the Fourier transform by adding the integral over two closed contours, one involving the upper half of the complex plane, the other involving the lower half, cf. Fig. D.1. For the first part in Eq. (D.6) the poles of the Fermi function do not appear, and one finds the following expression

$$\int_{-\infty}^{\infty} d\omega e^{-i\omega t} A(\omega) = 2\pi i \left(\Theta(-t) \sum_{\{a_\uparrow^0\}} \text{Res}_{a_\uparrow^0} A(\omega) - \Theta(t) \sum_{\{a_\downarrow^0\}} \text{Res}_{a_\downarrow^0} A(\omega) \right), \quad (\text{D.7})$$

where $\{a_\uparrow^0\}$ which includes the roots of the denominator of $a(\omega)$ with positive imaginary part and $\{a_\downarrow^0\}$ which includes the roots with negative imaginary part. The

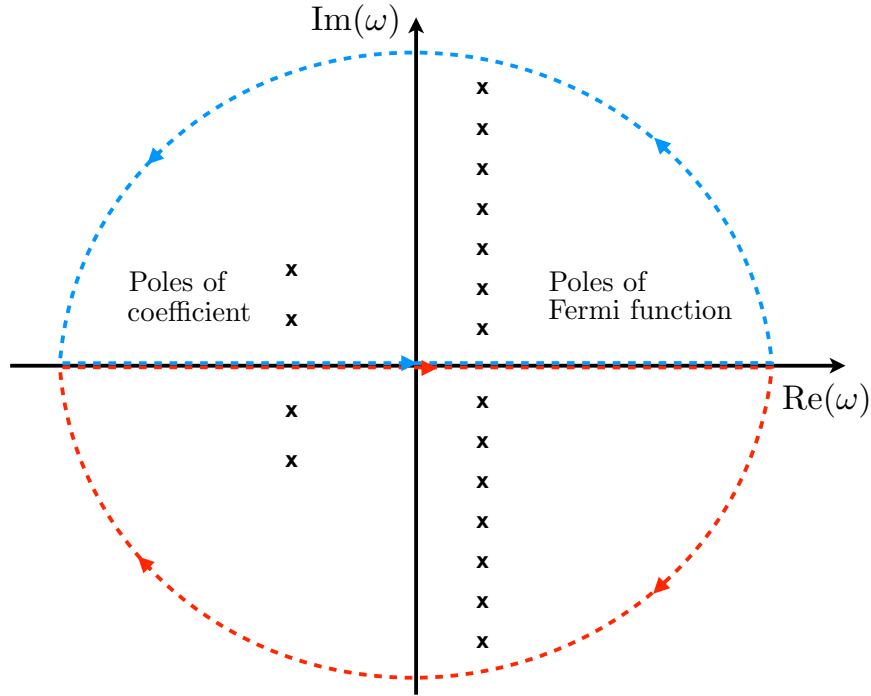


Figure D.1: The upper (blue) and lower (red) contours of the complex integration to Fourier transform the elements of the dressed Green function. Crosses denote poles, with the poles of the Fermi function (right hand side, due to finite bias voltage) being infinitely many. Since the arcs are pushed to infinity, they do not have a contribution to the integral.

negative sign between the two parts is attributed to the fact that the contour involving the lower half of the complex plane runs counter-clockwise, which introduces this additional minus sign.

For the second and third addend one has to take into account not only the poles of the coefficient, but the poles of the Fermi function, too. The Fermi function $f(x) = (1 + e^{\beta x})^{-1}$ has an infinite number of poles given by $\{f^0\} = \{x | \exists n \in \mathbb{Z} : x = (2n+1)\frac{i\pi}{\beta}\}$. One finds that the residue is for all of them given by $\text{Res}_{f^0} f(\omega) = \frac{1}{\beta}$. With this, one is then able to transform these addends as

$$\int_{-\infty}^{\infty} d\omega e^{-i\omega t} B(\omega) f_L(\omega) = 2\pi i \left(\Theta(-t) \left[\sum_{\{b_{\uparrow}^0\}} \text{Res}_{b_{\uparrow}^0} B(\omega) f_L(\omega) + \sum_{\{f_{\uparrow}^0\}} \text{Res}_{f_{\uparrow}^0} B(\omega) f_L(\omega) \right] - \Theta(t) \left[\sum_{\{b_{\downarrow}^0\}} \text{Res}_{b_{\downarrow}^0} B(\omega) f_L(\omega) + \sum_{\{f_{\downarrow}^0\}} \text{Res}_{f_{\downarrow}^0} B(\omega) f_L(\omega) \right] \right) \quad (\text{D.8})$$

$$\begin{aligned}
\int_{-\infty}^{\infty} d\omega e^{-i\omega t} C(\omega) f_R(\omega) = 2\pi i \left(\Theta(-t) \left[\sum_{\{c_{\uparrow}^0\}} \text{Res}_{c_{\uparrow}^0} C(\omega) f_R(\omega) + \sum_{\{f_{\uparrow}^0\}} \text{Res}_{f_{\uparrow}^0} C(\omega) f_R(\omega) \right] \right. \\
\left. - \Theta(t) \left[\sum_{\{c_{\downarrow}^0\}} \text{Res}_{c_{\downarrow}^0} C(\omega) f_R(\omega) + \sum_{\{f_{\downarrow}^0\}} \text{Res}_{f_{\downarrow}^0} C(\omega) f_R(\omega) \right] \right), \tag{D.9}
\end{aligned}$$

where $\{b_{\uparrow/\downarrow}^0\}$ and $\{c_{\uparrow/\downarrow}^0\}$ are defined in accordance with $\{a_{\uparrow/\downarrow}^0\}$. With this, one element of the dressed Green function is Fourier transformed. The other elements are transformed accordingly.

As a result, the time representations of all elements in Eq. (4.44) are known analytically, and with it one is then able to apply the ISPI scheme to calculate the generating functional.

Bibliography

- [1] B. J. van Wees, H. van Houten, C. W. J. Beenakker, J. G. Williamson, L. Kouwenhoven, D. van der Marel, and C. T. Foxon, *Quantized Conductance of Point Contacts in a Two-Dimensional Electron Gas*, *Phys. Rev. Lett.* **60**, 848 (1988).
- [2] D. Berman, N. B. Zhitenev, R. C. Ashoori, H. I. Smith, and M. R. Melloch, *Single-electron transistor as a charge sensor for semiconductor applications*, *J. Vac. Sci. Technol. B* **15**, 2844 (1997).
- [3] T. A. Fulton and G. J. Dolan, *Observation of Single-Electron Charging Effects in Small Tunnel Junctions*, *Phys. Rev. Lett.* **59**, 109 (1987).
- [4] M. H. Devoret and R. J. Schoelkopf, *Amplifying quantum signals with the single-electron transistor*, *Nature* **406**, 1039 (2000).
- [5] Z. Chowdhury, J. D. Harms, S. K. Khatamifard, M. Zabihi, Y. Lv, A. P. Lyle, S. S. Sapatnekar, U. R. Karpuzcu, and J.-P. Wang, *Efficient In-Memory processing Using Spintronics*, *IEEE Comp. Arch. Lett.* **17**, 42 (2018).
- [6] A. I. Ekimov and A. A. Onushchenko, *Quantum size effect in three-dimensional microscopic semiconductor crystals*, *Pis'ma Zh. Eksp. Teor Fiz.* **34**, 363 (1981); *Sov.-JETP Lett.* **34**, 345 (1981).
- [7] A. I. Ekimov, A. L. Efros, and A. A. Onushchenko, *Quantum size effect in semiconductor microcrystals*, *Solid State Commun.* **56**, 921 (1985).
- [8] L. E. Brus, *Electron-electron and electron-hole interactions in small semiconductor crystallites: The size dependence of the lowest excited electronic state*, *J. Chem. Phys.* **80**, 4403 (1984).
- [9] *Nanocrystals in their prime*, *Nature Nanotech* **9**, 325 (2014).
- [10] L. P. Kouwenhoven, D. G. Austing, and S. Tarucha, *Few-electron quantum dots*, *Rep. Prog. Phys.* **64**, 701 (2001).
- [11] G. J. Podd, S. J. Angus, D. A. Williams, and A. J. Ferguson, *Charge sensing in intrinsic silicon quantum dots*, *Appl. Phys. Lett.* **96**, 082104 (2010).
- [12] G. J. Iafrate, K. Hess, J. B. Krieger, and M. Macucci, *Capacitive nature of atomic-sized structures*, *Phys. Rev. B* **52**, 10737 (1995).
- [13] A. D. Crisan, S. Datta, J. J. Viennot, M. R. Delbecq, A. Cottet, and T. Kontos, *Harnessing spin precession with dissipation*, *Nat. Commun.* **7**, 10451 (2016).

- [14] J. R. Hauptmann, J. Paaske, and P. E. Lindelof, *Electric-field-controlled spin reversal in a quantum dot with ferromagnetic contacts*, **Nat. Phys.** **4**, 373 (2008).
- [15] S. M. Cronenwett, T. H. Oosterkamp, and L. P. Kouwenhoven, *A Tunable Kondo Effect in Quantum Dots*, **Science** **281**, 5376 (1998).
- [16] W. J. D. Haas, J. D. Boer, and G. J. V. D. Berg, *The Electrical Resistance of Gold, Copper and Lead at Low Temperatures*, **Physica** **1**, 1115 (1934).
- [17] J. Kondo, *Resistance Minimum in Dilute Magnetic Alloys*, **Progress of Theoretical Physics** **32**, 37 (1964).
- [18] D. Goldhaber-Gordon, H. Shtrikman, D. Mahalu, D. Abusch-Magder, U. Meirav, and M. A. Kastner, *Kondo effect in a single-electron transistor*, **Nature** **391**, 156 (1998).
- [19] M. Julliere, *Tunneling between ferromagnetic films*, **Phys. Lett. A** **54**, 225 (1975).
- [20] S. S. P. Parkin, C. Kaiser, A. Panchula, P. M. Rise, B. Hughes, M. Samant, and S.-H. Yang, *Giant tunnelling magnetoresistance at room temperature with MgO (100) tunnel barriers*, **Nat. Mater.** **3**, 862 (2004).
- [21] Y. M. Lee, J. Hayakawa, S. Ikeda, F. Matsukura, and H. Ohno, *Effect of electrode composition on the tunnel magnetoresistance of pseudo-spin-valve magnetic tunnel junction with a MgO tunnel barrier*, **Appl. Phys. Lett.** **90**, 212507 (2007).
- [22] S. Ikeda, J. Hayakawa, Y. Ashizawa, Y. M. Lee, K. Miura, H. Hasegawa, M. Tsunoda, F. Matsukura, and H. Ohno, *Tunnel magnetoresistance of 604% at 300 K by suppression of Ta diffusion in CoFeB/MgO/CoFeB pseudo-spin-valves annealed at high temperature*, **Appl. Phys. Lett.** **93**, 082508 (2008).
- [23] Z. Wang, I. Gutiérrez-Lezama, N. Ubrig, M. Kroner, M. Gibertini, T. Taniguchi, K. Watanabe, A. Imamoğlu, E. Giannini, and A. F. Morpurgo, *Very large tunneling magnetoresistance in layered magnetic semiconductor CrI₃*, **Nat. Commun.** **9**, 2516 (2018).
- [24] T. Song, X. Cai, M. W.-Y. Tu, X. Zhang, B. Huang, N. P. Wilson, K. L. Seyler, L. Zhu, T. Taniguchi, K. Watanabe, and et al., *Giant tunneling magnetoresistance in spin-filter van der Waals heterostructures*, **Science** **360**, 1214 (2018).
- [25] S. A. Wolf, J. Lu, M. R. Stan, E. Chen, and D. M. Treger, *The Promise of Nanomagnetism and Spintronics for Future Logic and Universal Memory*, **Proc. IEEE** **98**, 2155 (2010).
- [26] J. König and J. Martinek, *Interaction-Driven Spin Precession in Quantum-Dot Spin Valves*, **Phys. Rev. Lett.** **90**, 166602 (2003).
- [27] M. Braun, J. König, and J. Martinek, *Theory of transport through quantum-dot spin valves in the weak-coupling regime*, **Phys. Rev. B** **70**, 195345 (2004).

- [28] A. N. Pasupathy, R. C. Bialczak, J. Martinek, J. E. Grose, L. A. K. Donev, P. L. McEuen, and D. C. Ralph, *The Kondo Effect in the Presence of Ferromagnetism*, *Science* **306**, 86 (2004).
- [29] Y. Utsumi, J. Martinek, G. Schön, H. Imamura, and S. Maekawa, *Nonequilibrium Kondo effect in a quantum dot coupled to ferromagnetic leads*, *Phys. Rev. B* **71**, 245116 (2005).
- [30] B. Sothmann, D. Fütterer, M. Governale, and J. König, *Probing the exchange field of a quantum-dot spin valve by a superconducting lead*, *Phys. Rev. B* **82**, 094514 (2010).
- [31] L. Dell'Anna, A. Zazunov, and R. Egger, *Superconducting nonequilibrium transport through a weakly interacting quantum dot*, *Phys. Rev. B* **77**, 104525 (2008).
- [32] B. M. Andersen, K. Flensberg, V. Koerting, and J. Paaske, *Nonequilibrium Transport through a Spinful Quantum Dot with Superconducting Leads*, *Phys. Rev. Lett.* **107**, 256802 (2011).
- [33] H. Bruus and K. Flensberg, *Many-Body Quantum Theory in Condensed Matter Physics* (Oxford University Press, Oxford, 2004).
- [34] J.-D. Pillet, C. H. L. Quay, P. Morfin, C. Bena, A. L. Yeyati, and P. Joyez, *Andreev bound states in supercurrent-carrying carbon nanotubes revealed*, *Nat. Phys.* **6**, 965 (2010).
- [35] M. R. Buitelaar, W. Belzig, T. Nussbaumer, B. Babić, C. Bruder, and C. Schönenberger, *Multiple Andreev Reflections in a Carbon Nanotube Quantum Dot*, *Phys. Rev. Lett.* **91**, 057005 (2003).
- [36] S. D. Franceschi, L. Kouwenhoven, C. Schönenberger, and W. Wernsdorfer, *Hybrid superconductor–quantum dot devices*, *Nat. Nanotech.* **5**, 703 (2010).
- [37] T. Meng, S. Florens, and P. Simon, *Self-consistent description of Andreev bound states in Josephson quantum dot devices*, *Phys. Rev. B* **79**, 224521 (2009).
- [38] C. Buizert, A. Oiwa, K. Shibata, K. Hirakawa, and S. Tarucha, *Kondo Universal Scaling for a Quantum Dot Coupled to Superconducting Leads*, *Phys. Rev. Lett.* **99**, 136806 (2007).
- [39] S. Droste, J. Splettstoesser, and M. Governale, *Finite-frequency noise in a quantum dot with normal and superconducting leads*, *Phys. Rev. B* **91**, 125401 (2015).
- [40] S. Weiss and J. König, *Odd-triplet superconductivity in single-level quantum dots*, *Phys. Rev. B* **96**, 064529 (2017).
- [41] R. López, R. Aguado, and G. Platero, *Shot noise in strongly correlated double quantum dots*, *Phys. Rev. B* **69**, 235305 (2004).
- [42] D. Kotekar-Patil, A. Corna, R. Maurand, A. Crippa, A. Orlov, S. Barraud, L. Hutin, M. Vinet, X. Jehl, S. D. Franceschi, and M. Sanquer, *Pauli spin blockade in CMOS double quantum dot devices*, *Phys. Stat. Sol. B* **254**, 1600581 (2017).

- [43] V. Kashcheyevs, A. Schiller, A. Aharony, and O. Entin-Wohlman, *Unified description of phase lapses, population inversion, and correlation-induced resonances in double quantum dots*, *Phys. Rev. B* **75**, 115313 (2007).
- [44] S. Wenderoth, J. Bätge, and R. Härtle, *Sharp peaks in the conductance of a double quantum dot and a quantum-dot spin valve at high temperatures: A hierarchical quantum master equation approach*, *Phys. Rev. B* **94**, 121303(R) (2016).
- [45] M. Ciorga, A. S. Sachrajda, P. Hawrylak, C. Gould, P. Zawadzki, S. Jullian, Y. Feng, and Z. Wasilewski, *Addition spectrum of a lateral dot from Coulomb and spin-blockade spectroscopy*, *Rhys. Rev. B* **61**, R16315 (2000).
- [46] S. Sahoo, T. Kontos, J. Furer, C. Hoffmann, M. Gräber, A. Cottet, and C. Schönenberger, *Electric field control of spin transport*, *Nat. Phys.* **1**, 99 (2005).
- [47] A. Cottet, T. Kontos, S. Sahoo, H. T. Man, M.-S. Choi, W. Belzig, C. Bruder, A. F. Morpurgo, and C. Schönenberger, *Nanospintronics with carbon nanotubes*, *Semicond. Sci. Technol.* **21**, S78 (2006).
- [48] R. Hanson, L. P. Kouwenhoven, J. R. Petta, S. Tarucha, and L. M. K. Vandersypen, *Spins in few-electron quantum dots*, *Rev. Mod. Phys.* **79**, 1217 (2007).
- [49] K. Hamaya, M. Kitabatake, K. Shibata, M. Jung, M. Kawamura, K. Hirakawa, T. Machida, T. Taniyama, S. Ishida, and Y. Arakawa, *Electric-field control of tunneling magnetoresistance effect in a Ni / InAs / Ni quantum-dot spin valve*, *Appl. Phys. Lett.* **91**, 022107 (2007).
- [50] K. Hamaya, M. Kitabatake, K. Shibata, M. Jung, M. Kawamura, K. Hirakawa, T. Machida, T. Taniyama, S. Ishida, and Y. Arakawa, *Kondo effect in a semiconductor quantum dot coupled to ferromagnetic electrodes*, *Appl. Phys. Lett.* **91**, 232105 (2007).
- [51] E. A. Laird, F. Kuemmeth, G. A. Steele, K. Grove-Rasmussen, J. Nygård, K. Flensberg, and L. P. Kouwenhoven, *Quantum transport in carbon nanotubes*, *Rev. Mod. Phys.* **87**, 703 (2015).
- [52] M. Zaffalon and B. J. van Wees, *Zero-Dimensional Spin Accumulation and Spin Dynamics in a Mesoscopic Metal Island*, *Phys. Rev. Lett* **91**, 186601 (2003).
- [53] L. V. Keldysh, *Diagram Technique for nonequilibrium processes*, *Zh. Eksp. Teor. Fiz.* **47**, 1515 (1964); *Sov. Phys.-JETP* **20**, 1018 (1965).
- [54] A. Kamenev, *Field Theory of Non-Equilibrium Systems* (Cambridge University Press, Cambridge, 2011).
- [55] H. F. Trotter, *On the product of semi-groups of operators*, *Proc. Amer. Math. Soc.* **10**, 545 (1959).
- [56] M. Suzuki, *Generalized Trotter's formula and systematic approximants of exponential operators and inner derivations with applications to many-body problems*, *Commun. Math. Phys.* **51**, 183 (1976).

- [57] A.-P. Jauho, N. S. Wingreen, and Y. Meir, *Time-dependent transport in interacting and noninteracting resonant-tunneling systems*, *Phys. Rev. B* **50**, 5528 (1994).
- [58] C. Caroli, R. Combescot, P. Nozieres, and D. Saint-James, *Direct calculation of the tunneling current*, *J. Phys. C: Solid State Phys.* **4**, 916 (1971).
- [59] A. A. Abrikosov, L. P. Gorkov, and I. E. Dzyaloshinski, *Methods of quantum field theory in statistical physics* (Dover Publications, Inc., New York, 1963).
- [60] A. I. Larkin and Y. N. Ovchinnikov, *Nonlinear conductivity of superconductors in the mixed state*, *Zh. Eksp. Teor. Fiz.* **68**, 1915 (1975); *Sov. Phys.-JETP* **41**, 960 (1975).
- [61] Y. Meir and N. S. Wingreen, *Landauer formula for the current through an interacting electron region*, *Phys. Rev. Lett.* **68**, 2512 (1992).
- [62] D. C. Langreth, in *Linear and Nonlinear Electron Transport in Solids*, edited by J. T. Devreese and V. E. van Doren (Plenum Press, New York, 1976).
- [63] D. C. Langreth and P. Nordlander, *Derivation of a master equation for charge-transfer processes in atom-surface collisions*, *Phys. Rev. B* **43**, 2541 (1991).
- [64] A. Karabegov, Y. Neretin, and T. Voronov, *Felix Alexandrovich Berezin and His Work*, in *Geometric Methods in Physics. Trends in Mathematics*, edited by P. Kielanowski, S. Ali, A. Odziejewicz, M. Schlichenmaier, and T. Voronov (Birkhäuser, Basel, 2013).
- [65] A. Altland and B. Simons, *Condensed Matter Field Theory*, 2nd ed. (Cambridge University Press, Cambridge, 2010).
- [66] M. Combescure and D. Robert, *Fermionic coherent states*, *J. Phys. A: Math. Theor.* **45**, 244005 (2012).
- [67] F. A. Berezin, *The Method of Second Quantization* (Academic Press, New York, 1966).
- [68] J. W. Negele and H. Orland, *Quantum Many-Particle Systems* (Perseus Books Group, New York, 1998).
- [69] W.-M. Zhang, D. H. Feng, and R. Gilmore, *Coherent states: Theory and some applications*, *Rev. Mod. Phys.* **62**, 867 (1990).
- [70] A. Jensen, J. R. Hauptmann, J. Nygård, and P. E. Lindelof, *Magnetoresistance in ferromagnetically contacted single-wall carbon nanotubes*, *Phys. Rev. B* **72**, 035419 (2005).
- [71] W. Rudziński, J. Barnaś, R. Świrkowicz, and M. Wilczyński, *Spin effects in electron tunneling through a quantum dot coupled to noncollinearly polarized ferromagnetic leads*, *Phys. Rev. B* **71**, 205307 (2005).
- [72] S. Lindebaum and J. König, *Theory of transport through noncollinear single-electron spin-valve transistors*, *Phys. Rev. B* **84**, 235409 (2011).

- [73] S. Lindebaum and J. König, *Current fluctuations in noncollinear single-electron spin-valve transistors*, *Phys. Rev. B* **86**, 125306 (2012).
- [74] B. Sothmann, D. Futterer, M. Governale, and J. König, *Probing the exchange field of a quantum-dot spin valve by a superconducting lead*, *Phys. Rev. B* **82**, 094514 (2010).
- [75] M. Hell, B. Sothmann, M. Leijnse, M. R. Wegewijs, and J. König, *Spin resonance without spin splitting*, *Phys. Rev. B* **91**, 195404 (2015).
- [76] P. Stegmann, J. König, and S. Weiss, *Coherent dynamics in stochastic systems revealed by full counting statistics*, *Phys. Rev. B* **98**, 035409 (2018).
- [77] N. M. Gergs, S. A. Bender, R. A. Duine, and D. Schuricht, *Spin Switching via Quantum Dot Spin Valves*, *Phys. Rev. Lett.* **120**, 017701 (2018).
- [78] I. Weymann, *Finite-temperature spintronic transport through Kondo quantum dots: Numerical renormalization group study*, *Phys. Rev. B* **83**, 113306 (2011).
- [79] P. Simon, P. S. Cornaglia, D. Feinberg, and C. A. Balseiro, *Kondo effect with noncollinear polarized leads: A numerical renormalization group analysis*, *Phys. Rev. B* **75**, 045310 (2007).
- [80] M. Sindel, L. Borda, J. Martinek, R. Bulla, J. König, G. Schön, S. Maekawa, and J. von Delft, *Kondo quantum dot coupled to ferromagnetic leads: Numerical renormalization group study*, *Phys. Rev. B* **76**, 045321 (2007).
- [81] R. Świrkowicz, M. Wilczyński, and J. Barnaś, *The Kondo effect in quantum dots coupled to ferromagnetic leads with noncollinear magnetizations: effects due to electron-phonon coupling*, *J. Phys. Condens. Matter* **20**, 255219 (2008).
- [82] D. Matsubayashi and M. Eto, *Spin splitting and Kondo effect in quantum dots coupled to noncollinear ferromagnetic leads*, *Phys. Rev. B* **75**, 165319 (2007).
- [83] C. J. Gazza, M. E. Torio, and J. A. Riera, *Quantum dot with ferromagnetic leads: A density-matrix renormalization group study*, *Phys. Rev. B* **73**, 193108 (2006).
- [84] P. Kubiczek, A. N. Rubtsov, and A. I. Lichtenstein, *Exact real-time dynamics of single-impurity Anderson model from a single-spin hybridization-expansion*, *SciPost Phys.* **7**, 016 (2019).
- [85] A. E. Antipov, Q. Dong, J. Kleinhenz, G. Cohen, and E. Gull, *Currents and Green's functions of impurities out of equilibrium: Results from inchworm quantum Monte Carlo*, *Phys. Rev. B* **95**, 085144 (2017).
- [86] L. Simine and D. Segal, *Path-integral simulations with fermionic and bosonic reservoirs: Transport and dissipation in molecular electronic junctions*, *J. Chem. Phys.* **138**, 214111 (2013).
- [87] S. Weiss, J. Eckel, M. Thorwart, and R. Egger, *Iterative real-time path integral approach to nonequilibrium quantum transport*, *Phys. Rev. B* **77**, 195316 (2008); E: *Phys. Rev. B* **79**, 249901 (2009).

- [88] S. Weiß, *Nonequilibrium quantum transport and confinement effects in interacting nanoscale conductors* (Shaker Verlag, Aachen, 2008).
- [89] R. Hützen, S. Weiss, M. Thorwart, and R. Egger, *Iterative summation of path integrals for nonequilibrium molecular quantum transport*, *Phys. Rev. B* **85**, 121408 (2012).
- [90] D. Becker, S. Weiss, M. Thorwart, and D. Pfannkuche, *Non-equilibrium quantum dynamics of the magnetic Anderson model*, *New J. Phys.* **14**, 073049 (2012).
- [91] P. W. Anderson, *Localized Magnetic States in Metals*, *Phys. Rev.* **124**, 41 (1961).
- [92] F. Covito, F. G. Eich, R. Tuovinen, M. A. Sentef, and A. Rubio, *Transient Charge and Energy Flow in the Wide-Band Limit*, *J. Chem. Theory Comput.* **14**, 2495 (2018).
- [93] S. Weiss, R. Hützen, D. Becker, J. Eckel, R. Egger, and M. Thorwart, *Iterative path integral summation for nonequilibrium quantum transport: Iterative summation of path integrals*, *Phys. Stat. Sol. B* **250**, 2298 (2013).
- [94] D. Segal, A. J. Millis, and D. R. Reichman, *Numerically exact path-integral simulation of nonequilibrium quantum transport and dissipation*, *Phys. Rev. B* **82**, 205323 (2010).
- [95] T. L. Schmidt, P. Werner, L. Mühlbacher, and A. Komnik, *Transient dynamics of the Anderson impurity model out of equilibrium*, *Phys. Rev. B* **78**, 235110 (2008).
- [96] H. Wang and M. Thoss, *A multilayer multiconfiguration time-dependent Hartree study of the nonequilibrium Anderson impurity model at zero temperature*, *Chem. Phys.* **509**, 13 (2018).
- [97] J. König, *Quantum Fluctuations in the Single-Electron Transistor* (Shaker Verlag, Aachen, 1999).
- [98] E. Gull, A. J. Millis, A. I. Lichtenstein, A. N. Rubtsov, M. Troyer, and P. Werner, *Continuous-time Monte Carlo methods for quantum impurity models*, *Rev. Mod. Phys.* **83**, 349 (2011).
- [99] N. V. Prokof'ev and B. V. Svistunov, *Polaron Problem by Diagrammatic Quantum Monte Carlo*, *Phys. Rev. Lett.* **81**, 2514 (1998).
- [100] S. M. A. Rombouts, K. Heyde, and N. Jachowicz, *Quantum Monte Carlo Method for Fermions, Free of Discretization Errors*, *Phys. Rev. Lett.* **82**, 4155 (1999).
- [101] P. Werner, A. Comanac, L. de'Medici, M. Troyer, and A. J. Millis, *Continuous-Time Solver for Quantum Impurity Models*, *Phys. Rev. Lett.* **97**, 076405 (2006).
- [102] G. Cohen, E. Gull, D. R. Reichman, and A. J. Millis, *Taming the Dynamical Sign Problem in Real-Time Evolution of Quantum Many-Body Problems*, *Phys. Rev. Lett.* **115**, 266802 (2015).

- [103] K. G. Wilson, *The renormalization group: Critical phenomena and the Kondo problem*, *Rev. Mod. Phys.* **47**, 773 (1975).
- [104] S. R. White, *Density matrix formulation for quantum renormalization groups*, *Phys. Rev. Lett.* **69**, 2863 (1992).
- [105] R. Bulla, T. A. Costi, and T. Pruschke, *Numerical renormalization group method for quantum impurity systems*, *Rev. Mod. Phys.* **80**, 395 (2008).
- [106] U. Schollwöck, *The density-matrix renormalization group*, *Rev. Mod. Phys.* **77**, 259 (2005).
- [107] E. Boulat, H. Saleur, and P. Schmitteckert, *Twofold Advance in the Theoretical Understanding of Far-From-Equilibrium Properties of Interacting Nanostructures*, *Phys. Rev. Lett.* **101**, 140601 (2008).
- [108] R. P. Feynman, *Space-Time Approach to Non-Relativistic Quantum Mechanics*, *Rev. Mod. Phys.* **20**, 367 (1948).
- [109] A. Kamenev, *Many-body theory of non-equilibrium systems*, in *Nanophysics: Coherence and Transport*, edited by H. Bouchiat, Y. Gefen, S. Guéron, G. Montambaux, and J. Dalibard (Elsevier, New York, 2005).
- [110] J. Hubbard, *Calculation of Partition Functions*, *Phys. Rev. Lett.* **3**, 77 (1959).
- [111] J. E. Hirsch, *Discrete Hubbard-Stratonovich transformation for fermion lattice models*, *Phys. Rev. B* **28**, 4059 (1983).
- [112] D. K. Salkuyeh, *Comments on “A note on a three-term recurrence for a tridiagonal matrix”*, *Appl. Math. Comp.* **176**, 442 (2006).
- [113] H. A. Kramers and G. H. Wannier, *Statistics of the Two-Dimensional Ferromagnet. Part I*, *Phys. Rev.* **60**, 252 (1941).
- [114] H. A. Kramers and G. H. Wannier, *Statistics of the Two-Dimensional Ferromagnet. Part II*, *Phys. Rev.* **60**, 263 (1941).
- [115] L. Onsager, *Crystal Statistics. I. A Two-Dimensional Model with an Order-Disorder Transition*, *Phys. Rev.* **65**, 117 (1944).
- [116] K. B. Petersen and M. S. Pedersen, *The Matrix Cookbook*, Version 20121115 (Technical University of Denmark, Copenhagen, 2012).
- [117] S. Weiss and R. Egger, *Path-integral Monte Carlo simulations for interacting few-electron quantum dots with spin-orbit coupling*, *Phys. Rev. B* **72**, 245301 (2005).
- [118] R. M. Fye, *New results on Trotter-like approxiations*, *Phys. Rev. B* **33**, 6271 (1986).
- [119] S. Mundinar, P. Stegmann, J. König, and S. Weiss, *Iterative path-integral summations for the tunneling magnetoresistance in interacting quantum-dot spin valves*, *Phys. Rev. B* **99**, 195457 (2019).

- [120] S. Mundinar, A. Hucht, J. König, and S. Weiss, *Interaction-induced current asymmetries in resonant transport through interacting quantum-dot spin valves revealed by iterative summation of path integrals*, *Phys. Rev. B* **102**, 045404 (2020).
- [121] B. Sothmann, *Influence of spin excitations on transport through a quantum-dot spin valve* (Universität Duisburg-Essen, 2011).
- [122] M. Abramowitz and I. A. Stegun, eds., *Handbook of Mathematical Functions* (Dover Publications, Inc., New York, 1972).
- [123] I. Weymann, J. König, J. Martinek, J. Barna, and G. Schön, *Tunnel magnetoresistance of quantum dots coupled to ferromagnetic leads in the sequential and cotunneling regimes*, *Phys. Rev. B* **72**, 115334 (2005).
- [124] I. Weymann, J. Barnaś, J. König, J. Martinek, and G. Schön, *Zero-bias anomaly in cotunneling transport through quantum-dot spin valves*, *Phys. Rev. B* **72**, 113301 (2005).
- [125] I. Weymann and J. Barnaś, *Shot noise and tunnel magnetoresistance in multilevel quantum dots: Effects of cotunneling*, *Phys. Rev. B* **77**, 075305 (2008).
- [126] J. Martinek, J. Barnaś, S. Maekawa, H. Schoeller, and G. Schön, *Spin accumulation in ferromagnetic single-electron transistors in the cotunneling regime*, *Phys. Rev. B* **66**, 014402 (2002).
- [127] K. Ono, H. Shimada, and Y. Ootuka, *Enhanced Magnetic Valve Effect and Magneto-Coulomb Oscillations in Ferromagnetic Single Electron Transistor*, *J. Phys. Soc. Jpn.* **66**, 1261 (1997).
- [128] L. F. Schelp, A. Fert, F. Fettar, P. Holody, S. F. Lee, J. L. Maurice, F. Petroff, and A. Vaurés, *Spin-dependent tunneling with Coulomb blockade*, *Phys. Rev. B* **56**, R5747(R) (1997).
- [129] K. Yakushiji, S. Mitani, K. Takanashi, S. Takahashi, S. Maekawa, H. Imamura, and H. Fujimori, *Enhanced tunnel magnetoresistance in granular nanobridges*, *Appl. Phys. Lett.* **78**, 515 (2001).
- [130] S. Takahashi and S. Maekawa, *Effect of Coulomb Blockade on Magnetoresistance in Ferromagnetic Tunnel Junctions*, *Phys. Rev. Lett.* **80**, 1758 (1998).
- [131] A. Rosch, J. Paaske, J. Kroha, and P. Wölfle, *Nonequilibrium Transport through a Kondo Dot in a Magnetic Field: Perturbation Theory and Poor Man's Scaling*, *Phys. Rev. Lett.* **90**, 076804 (2003).
- [132] J. Martinek, Y. Utsumi, H. Imamura, J. Barnaś, S. Maekawa, J. König, and G. Schön, *Kondo Effect in Quantum Dots Coupled to Ferromagnetic Leads*, *Phys. Rev. Lett.* **91**, 107203 (2003).
- [133] J. Martinek, M. Sindel, L. Borda, J. Barnaś, J. König, G. Schön, and J. von Delft, *Kondo Effect in the Presence of Itinerant-Electron Ferromagnetism Studied with the Numerical Renormalization Group Method*, *Phys. Rev. Lett.* **91**, 247202 (2003).

-
- [134] J. Martinek, M. Sindel, L. Borda, J. Barnaś, R. Bulla, J. König, G. Schön, S. Maekawa, and J. von Delft, *Gate-controlled spin splitting in quantum dots with ferromagnetic leads in the Kondo regime*, *Phys. Rev. B* **72**, 121302 (2005).
- [135] R. D. Mattuck, *A Guide to Feynman Diagrams in the Many-Body Problem* (Dover Publications Inc., New York, 1992).
- [136] E. Kleinherbers, P. Stegmann, and J. König, *Revealing attractive electron–electron interaction in a quantum dot by full counting statistics*, *New J. Phys.* **20**, 073023 (2018).
- [137] C. W. J. Beenakker, *Theory of Coulomb-blockade oscillations in the conductance of a quantum dot*, *Phys. Rev. B* **44**, 1646 (1991).
- [138] A. O. Gogolin, *Lectures on Complex Integration*, edited by E. G. Tsitsishvili and A. Komnik (Springer, Berlin, 2014).
- [139] A. I. Ekimov and A. A. Onushchenko, *Sov.-JETP Lett.* **34**, 345 (1981).
- [140] L. V. Keldysh, *Sov. Phys.-JETP* **20**, 1018 (1965).
- [141] A. I. Larkin and Y. N. Ovchinnikov, *Sov. Phys.-JETP* **41**, 960 (1975).
- [142] S. Weiss, J. Eckel, M. Thorwart, and R. Egger, *Phys. Rev. B* **79**, 249901 (2009).

Danksagung

An dieser Stelle möchte ich all denen danken, die diese Arbeit ermöglicht haben und mich unterstützt haben. Ganz besonderer Dank gilt Prof. Dr. Jürgen König, dass er es mir ermöglicht hat auf diesem spannenden Gebiet zu forschen und dass ich bei ihm promovieren durfte. Während dieser Zeit hat er mich stets motiviert, mich mit ehrlicher und konstruktiver Kritik vorangebracht und hatte stets Rat, wenn er denn nötig war. Nicht weniger dankbar bin ich Dr. Stephan Weiß, dass er mich mit der ISPI Methode bekannt gemacht hat und dass ich immer zu ihm kommen konnte, wenn ich Diskussionsbedarf hatte oder auch einfach nur reden wollte.

Priv.-Doz. Dr. Alfred Hucht, Dr. Philipp Stegmann und Eric Kleinherbers möchte ich nicht nur für viele gute Gespräche danken, sondern auch für viele physikalische Diskussionen, die oftmals weit weg von meinem eigentlichen Themengebiet lagen und mein physikalisches Wissen äußerst erweitert haben. Besonders möchte ich Fred dafür danken, dass er mir den Transfer-Matrix Formalismus beigebracht hat, Philipp und Eric möchte ich besonders dafür danken, dass ich stets zu ihnen kommen konnte, wenn ein störungstheoretischer Blick auf meine Probleme hilfreich war.

Für die tolle und angenehme Arbeitsatmosphäre möchte ich allen Mitgliedern der AG König und AG Sothmann danken. Insbesondere gilt mein Dank Sabina Grubba für die endlose Geduld bei organisatorischen Problemen, sowie meinen Bürokolleginnen Marianne und Anna für die immer angenehme und diskussionsfreudige Atmosphäre.

Darüber hinaus will ich meinen Freunden danken, für die vielen schönen, gemeinsamen Erfahrungen. Namentlich möchte ich an dieser Stelle nennen: Natalie, Michael, Tobias, Sarah, Fabian, Isabell, Julius, Claudi, Nicoletta, Bernd, Flo und Johann. Danke, dass es euch gibt.

Zum Schluss will ich mich noch bei Saphira bedanken, die mich während dieser Zeit ausgehalten hat und mich immer wieder zum Lachen gebracht hat, sowie bei meiner Familie für ihre endlose Unterstützung. Ganz besonders bei meiner Mutter und meiner Schwester, dass sie stets für mich da waren und mir immer zugehört haben, selbst wenn ich mal quengelig war, sowie bei meinem Vater für sein großes Interesse an meiner Arbeit. Danke euch allen!

Erklärung

Die hier vorgelegte Dissertation habe ich selbstständig verfasst und zur Erlangung des Grades „Doktor der Naturwissenschaften“ eingereicht. Ich habe nur die angegebenen Hilfsmittel benutzt und alle von anderen Werken wörtlich oder inhaltlich übernommenen Stellen – einschließlich der Abbildungen – als solche gekennzeichnet. Die Dissertation wurde in der vorgelegten oder in ähnlicher Form noch bei keiner anderen Institution eingereicht. Ich habe bisher keine erfolglosen Promotionsversuche unternommen.

Duisburg, den 16. Juli 2020

Simon Mundinar